MULTISCALE MODELING OF NEUROBIOLOGICAL SYSTEMS

by

Cihan Kaya

BS, Bogazici University, 2010

MS, Bogazici University, 2013

Submitted to the Graduate Faculty of

the School of Medicine in partial fulfillment

of the requirements for the degree of

Doctor of Philosophy

University of Pittsburgh

2018

UNIVERSITY OF PITTSBURGH

SCHOOL OF MEDICINE

This dissertation was presented

by

Cihan Kaya

It was defended on

July 27, 2018

and approved by

Andreas Pfenning, PhD, Assistant Professor, Computational Biology

Terrence J. Sejnowski, PhD, Professor, Computational Neurobiology

Alexander Sorkin, PhD, Professor, Cell Biology

Dissertation Co-Director: James R. Faeder, PhD, Associate Professor, Computational and Systems Biology

Dissertation Co-Director: Ivet Bahar, PhD, Professor, Computational and Systems Biology

MULTISCALE MODELING OF NEUROBIOLOGICAL SYSTEMS

Cihan Kaya, PhD

University of Pittsburgh, 2018

The central nervous system (CNS) is one of the most complicated living structures in the universe. A single gene expression, the expression level of a single protein or the concentration of a neurotransmitter could regulate the entire functionality of the CNS. The CNS needs to be investigated as a multiscale system with connections among different levels. The existing technology significantly limits experimental studies, and computational modeling is a useful tool for understanding how parts are connected, regulated, and function together. Ideally, the goal is to develop unified computational methodologies for exploring biological systems at multiple scales ranging from molecular to cellular to tissue level. While rigorous models have been developed at the molecular scale, higher level approaches usually suffer from lack of physical realism and lack of knowledge on model parameters. Molecular level studies can help to define reaction schemes and parameters which could be used in cellular microphysiology models, and image data provide a structural basis for reconstructing the surroundings of the cellular system of interest.

This dissertation develops and tests a new multiscale model of dopaminergic signaling and a detailed model of the activation-triggered subunit exchange mechanism of calcium/calmodulin-dependent kinase type II (CaMKII). The goal is to develop and use computational models to understand the molecular mechanisms of neurotransmission, and how disruptions may cause complex disorders and conditions such as drug abuse. The simulations of the dopamine (DA) signaling model show that the addition of the geometry of the environment and localization of

individual molecules significantly affect the DA reuptake. Consequently, the formation of DAT clusters reduces the DA clearance rate and increases DA receptor activity. In addition, the effects of the psychostimulants such as cocaine and amphetamine are also investigated. Constructed model and method can potentially serve as an *in silico* microscope to understand the molecular basis of signaling and regulation events in the CNS. Calibration of CaMKII model shows the limitations of the current parameter estimation methods for large biological models with long simulation times such as hours. The high dimensional parameter space and the limited and noisy data makes the parameter estimation task a challenge.

TABLE OF CONTENTS

1.0 INTRODUCTION 1

1.1 THE PROBLEM 5

1.2 THE APPROACH 7

1.3 HYPOTHESES AND MAJOR FINDINGS 10

1.4 SIGNIFICANCE 11

1.5 OVERVIEW 13

2.0 HETEROGENEITIES IN AXONAL STRUCTURE AND TRANSPORTER DISTRIBUTION LOWER DOPAMINE REUPTAKE EFFICIENCY 15

2.1 BACKGROUND 15

2.2 METHODS 18

2.2.1 Confocal imaging of immunolabeled DATs in transgenic mouse brains . 18

2.2.2 *In silico* reconstruction of DA axonal terminals in the striatum 19

2.2.3 Distribution of DATs on the axonal surfaces 23

2.2.4 MCell simulations of DA release and reuptake events in DA neurons 26

2.2.5 Conformational dynamics of DAT 30

2.3 RESULTS 35

2.3.1 *In silico* turnover and $[DA]_{EC}$ at half-maximal-rate conform to experimental data 35

2.3.2 DAT conformers reach a dynamic equilibrium within hundreds of milliseconds. 37

2.3.3 DA levels exhibit large fluctuations depending on AZ structure and DAT surface distribution 39

2.3.4 Cellular structural complexity modulates the fractional occupancy of high-affinity DA receptors 43

2.3.5 Phasic firing favors high transient levels in [DA] while retaining the average $[DA]_{EC}$ 46

2.3.6 Non-uniform surface distribution of DATs is a major modulator of the strength and intensity of DA signaling 53

2.4 DISCUSSION 57

2.4.1 Overview 57

2.4.2 DA reuptake simulations require spatially extended models 58

2.4.3 Spatial irregularities and hindrance in the interstitial region between neurons limits DA receptor activation 59

2.4.4 Heterogeneous surface distribution of DAT reduces the effectiveness of DA clearance 59

2.4.5 Firing patterns determine the relative levels of inhibitory vs. excitatory responses 61

2.4.6 The modeling framework is extensible to analyzing the effect of psychostimulants on DA reuptake dynamics 63

3.0 EFFECT OF PSYCHOSTIMULANTS ON DOPAMINERGIC SIGNALING ... 65

3.1 BACKGROUND 65

3.2 METHOD 67

3.2.1 Spatially realistic model of DA release and reuptake in the presence of psychostimulant cocaine 67

3.2.2 Network model of intracellular dopamine dynamics 69

3.3 RESULTS 72

3.3.1 Cocaine competitively inhibits DAT and exponentially increases DA receptor activity 72

3.3.2 Hybrid spatial-network model of AMPH-induced DA efflux 74

3.3.3 DAT distribution affects the activation of DA efflux from DAT 79

3.4 DISCUSSION 81

3.4.1 Overview 81

3.4.2 Cocaine inhibits DA reuptake at sufficient concentrations 82

3.4.3 AMPH uptake is the main regulator of DA efflux at low AMPH concentrations 83

3.4.4 Addition of key modulators to simulation environment make simulations more realistic 85

4.0 MODELING AND ANALYSIS OF THE SUBUNIT EXCHANGE MECHANISM IN CAMKII SIGNALING 86

4.1 BACKGROUND 86

4.2 METHODS 91

4.2.1 Model construction 91

4.2.2 Experimental data 96

4.2.3 Network-Free simulations 101

4.2.4 Genetic algorithms with online model checking 102

4.3 RESULTS AND DISCUSSION 104

4.3.1 Subunit exchange can take place in timescales from minutes to hours .. 104

4.3.2 GA implementation with NFsim fails due to the size of the model 106

4.3.3 GA with Online Model Checking 108

4.4 CONCLUSION 114

5.0 CONCLUSION 116

5.1 LIMITATIONS 117

5.2 FUTURE WORK 119

5.2.1 Parkinson's disease condition implementation 119

5.2.2 Improvement of vesicular DA release mechanism 119

5.2.3 A more realistic placement of DA receptors 120

5.2.4 The effect of the DA auto-receptor activation on the DA release and reuptake process 121

5.2.5 Signaling molecules can change the outcome of the AMPH-induced DA efflux model 122

5.2.6 Proper implementation of hybrid genetic algorithm/online model checking with NFsim 122

5.2.7 Spatial modeling of CaMKII dynamics 123

APPENDIX A CELL SIMULATIONS 124

A.1 ANATOMY OF AN MCELL MODEL 124

A.1.1 Simulation specifications and main file 124

A.1.2 Simulation environment and geometry 127

A.1.3 Parameters 128

A.1.4 Molecules **128**

A.1.5 Reactions **129**

A.1.6 Surface classes **130**

A.1.7 Surface modifications **130**

A.1.8 Release patterns **131**

A.1.9 Model outputs **132**

APPENDIX B BIONETGEN MODEL OF ACTIVATION-TRIGGERED SUBUNIT EXCHANGE OF CAMKII **134**

B.1 PARAMETERS **134**

B.2 MOLECULE TYPES **135**

B.3 INITIALIZATION **136**

B.4 OBSERVABLES **138**

B.5 FUNCTIONS **139**

B.6 REACTION RULES **140**

B.7 MODEL EXECUTION **141**

BIBLIOGRAPHY **143**

LIST OF TABLES

Table 1. Geometric characteristics of axon terminals reconstructed for simulations. 22

Table 2. Parameters and properties used in MCell simulations 25

Table 3. Structural properties near *AZ*s 42

Table 4. $[DA]_{EC}$ values (mean ± standard error of the mean) under different conditions 49

Table 5. Percentage of high- and low-affinity DA receptors that DAs can potentially bind 52

Table 6. Kinetic parameters of the CaMKII model adopted from (Michalski & Loew, 2012) 95

Table 7. Parameters for TLBR model 110

LIST OF FIGURES

Figure 1. Reconstruction of the morphology of DA neuronal axons 21

Figure 2. Four space-dependent models of different plasma distributions of DATs 24

Figure 3. Schematic representation of the sequence of events occurring during the transport cycle 31

Figure 4. Results from global sensitivity analysis performed for kinetic parameters representing DAT conformational dynamics 34

Figure 5. Time evolution of DA concentration and DAT conformational states averaged over 140 independent MCell runs 36

Figure 6. Snapshots from MCell simulations of DA release and reuptake by DATs on DA terminals. 38

Figure 7. Time evolution of DA levels in the EC region after a single release event in different *AZ*s. 40

Figure 8. Expected fractional occupancy (or percentage saturation) of DA high-affinity receptors in response to successive releases. 45

Figure 9. Comparative analysis of global EC DA levels under different firing patterns and the effect of the complexity of cell geometry and the heterogeneity of DAT surface density 47

Figure 10. Time evolution of DA level in the synapse after a release event 50

Figure 11. Distribution of peak heights and widths for EC DA levels 54

Figure 12. Probability distributions of $[DA]_{EC}$ level under lateral DAT diffusion and Probability distributions of DAT distances to closest *AZ*. 56

Figure 13. Kinetic scheme of cocaine and DA binding to DAT 69

Figure 14. A detailed description of the AMPH-induced intracellular signaling model 71

Figure 15. Comparative analysis of EC DA concentration under different cocaine concentrations 73

Figure 16. Correlation between intracellular AMPH concentration, DAT phosphorylation rate, and DAT endocytosis 76

Figure 17. Intracellular AMPH dynamics in the intracellular network model 78

Figure 18. Spatial model AMPH-induced DA efflux 78

Figure 19. Comparative analysis of EC DA concentration under different AMPH concentrations 80

Figure 20. CaMKII model..... 93

Figure 21. Frequency-dependent CaMKII activation data 98

Figure 22. Activation triggered subunit exchange data 100

Figure 23. Schematic description GA implementation with model checking 103

Figure 24. Parameter scan results for varying dissociation constant. 105

Figure 25. Best calculated objective functions for different generations 108

Figure 26. The data generated for parameter estimation from TLBR model. 111

Figure 27. Performance of the hybrid GA/OMC method 113

LIST OF EQUATIONS

Equation 1 27

Equation 2 27

Equation 3 28

Equation 4 28

Equation 5 28

Equation 6 75

Equation 7 77

Equation 8 107

LIST OF ABBREVIATIONS

aMD	Accelerated molecular dynamics
AP	Action potential
AZ	Active zone
ABF	Adaptive biasing force
AMPA	α-amino-3-hydroxy-5-methyl-4-isoxazolepropionic acid
AMPH	Amphetamine
ACSF	Artificial cerebrospinal fluid
ADHD	Attention deficit and hyperactivity disorder
BNGL	BioNetGen language
Ca^{++}	Calcium ion
CaV	Voltage gated calcium channels
CaMKII	Calcium/calmodulin dependent kinase type II
CaM	Calmodulin
CNS	Central nervous system
cMD	Conventional molecular dynamics
CA	Cornu Ammonis
DA	Dopamine
DAT	Dopamine Transporter
Str	Dorsal striatum
dDAT	*Drosophila* dopamine transporter
EM	Electron microscopy

ER	Endoplasmic reticulum
EC	Extracellular
FEP	Free energy perturbation
GA	Genetic algorithm
GTP	Guanosine triphosphate
IC	Intracellular
IC50	Half inhibition concentration
HA	Hemagglutinin-A
hDAT	Human dopamine transporter
IP_3R	Inositol 1,4,5-triphosphate receptor
IF	Inward-facing
LTD	Long-term depression
LTP	Long-term potentiation
MDL	Model description language
NMDA	N-methyl-D-aspartate
NAc	*Nucleus accumbens*
OMC	Online model checking
OF	Outward-facing
PLC	Phospholipase C
PEG	Polyethylene glycol
PKA	Protein kinase A
PP1	Protein phosphatase
PP2A	Protein phosphatase 2

Na^+	Sodium ion
SSA	Stochastic simulation algorithm
SNc	*Substantia nigra*
TIRF	Total internal reflection fluorescence
TAAR	Trace amine associated receptor
TLBR	Trivalent ligand bivalent receptor
VMAT	Vesicular monoamine transporter
VT	Volume transmission

ACKNOWLEDGMENTS

This dissertation is dedicated to my partner Gizem, for all the support and unconditional love she has for me. I owe special gratitude to my parents Huseyin and Gonul, and my sister Nagehan. This thesis would not be possible without their unlimited love and encouragement.

Special recognition to my advisors Dr. Ivet Bahar and Dr. James Faeder, I cannot express how grateful I am for your mentorship. I learned a lot from you and your support and encouragement help me to grow and be a better scientist and a better person.

I would like to thank Dr. Andreas Pfenning, Dr. Alexander Sorkin, and Dr. Terry Sejnowski for serving as my committee members. Your scientific and academic advice made my work more meaningful and successful.

I would specifically like to thank Dr. Mary Cheng and Dr. Bing Liu for their collaboration and scientific advice. They taught me a lot about structural biology and systems biology.

I would like to thank several past and present members of the Bahar and Faeder Lab, in particular, Dr. James Krieger, She Zhang, Dr. Mert Gur and Sanjana Gupta for joyous scientific discussions and advice.

Finally, I would like to express my gratitude to Ms. Kelly Gentille and Ms. Nancy Linderman for their support and advice. I cannot imagine graduate school without their help navigating the program requirements and bureaucracy.

I would like to thank all the members of the Molecular Pathology lab at UPMC. A special thanks to Dr. Marina Nikiforova and Dr. Yuri Nikiforov for giving me such a fantastic opportunity

to work in a great lab. I thank the members of the MGP-bioinformatics team, Dr. Lucas Santana dos Santos and Mr. Liang Chen. It has been a great joy and pleasure in working with you. I want to express my gratitude to Dr. Abigail Wald for her understanding and support on all issues.

Finally, I want to thank all my family and friends. They have been a source of love and support for me regardless of the situation.

1.0 INTRODUCTION

The human brain is one of the most complex living structures in the universe. The human brain can store more information than any supercomputer, and the connections in the brain being more extensive than any social network that a human can imagine. The advances in technology provide us with much useful information about the way brain works, and there are many unresolved questions such as how it controls all the other organs and how it processes memories and emotions. The brain plays a central role in many behavioral conditions, and defects/disruptions in the brain can cause over 1,000 disorders. Brain disorders affect approximately one-sixth of the population and cost billions of dollars to the economy.

As in the case of any complex systems, the brain has a lot of heterogeneous and moving parts. It has various cell types, and each cell functions in different ways (Churchland & Sejnowski, 2016). As an example, hippocampal neurons have a length of the order of micrometers μm's, and they make many connections with other neurons, whereas sciatic neuron can go up to a meter long and the total number of connections may not be as large as a hippocampal neuron (Nolte, 2002). The functional differences are not only caused by the length of scale or the number of connections but also can be identified with low-level components such as the neurotransmitter type, its location in the brain, or the primary type of neurotransmitter transporter that the neuron expresses.

In the central nervous system (CNS) neurons are connected through synapses, and signaling at synaptic connections is one of the primary processes that mediate brain function (Shepherd, 2003). Due to the importance of synapses in the CNS function, a significant portion of neurodegenerative disorders such as Parkinson's disease or drug abuse can be caused by defects in this signaling process (Dagher & Robbins, 2009). The disruption of synapses between neurons can lead to imbalances between excitation and inhibition in neural circuits, which can give rise to abnormal cognitive processing (Franken, Stam, Hendriks, & van den Brink, 2003). Therefore, it is necessary to understand how conventional circuits maintain balance to resolve issues caused by disturbances in synapses. Different synapse types use different sets of neurotransmitters, receptors, and transporter molecules. These differences lead to different functions, and the defects lead to different diseases (Lovinger, 2010). One of the most widely studied and important synapse types is the dopaminergic synapse due to its role in reward prediction/valuation (Wise & Rompre, 1989).

Dopamine (DA) is in various regions of the brain. Dopamine transporters (DAT) are membrane proteins that transport DA across the cell membrane. DAT-mediated DA reuptake is the primary mechanism for removal of extracellular (EC) DA from synaptic and extra-synaptic space (Torres, Gainetdinov, & Caron, 2003). The regulation of DA reuptake depends on the localization and expression level of DATs on the membrane (Volz, Hanson, & Fleckenstein, 2007), as well as the intramolecular and intermolecular interaction mechanisms that enable effective transport, signaling, regulation, and recycling. The mechanisms that control the distribution and trafficking of DAT are still ambiguous. It is essential to understand how various factors regulate DA reuptake mechanism.

Lack of DA clearance in certain regions of the brain increases DA levels in the extra-synaptic regions, and the activity of the DA receptors is upregulated accordingly. Downstream

signaling from DA receptors activates the reward and satisfaction pathways (Wise & Rompre, 1989). Therefore, DA neurotransmission is one of the focal points of the drug abuse research (Di Chiara & Imperato, 1988). More specifically, the effect of psychostimulants such as cocaine and amphetamine (AMPH) on DA neurotransmission has been a topic of study for more than two decades. Many of these studies are experimental, and a group of properties such as surface density of distribution of DAT has not been extensively studied due to limitations in technology.

The conformational dynamics of DAT is one of the primary determinants of DA transport efficiency (Vaughan & Foster, 2013). Advances in structural characterization of membrane proteins have opened the way to the resolution of the crystal structure of DAT (Penmatsa, Wang, & Gouaux, 2013; Wang, Penmatsa, & Gouaux, 2015), and molecular simulations of these structures identified various states and dynamics of their transitions (Mary Hongying Cheng & Bahar, 2015; Mary Hongying Cheng et al., 2015; Mary Hongying Cheng, Garcia-Olivares, Wasserman, DiPietro, & Bahar, 2017; Khelashvili et al., 2015; Ma et al., 2017; Razavi, Khelashvili, & Weinstein, 2017). Individual states of the DAT have multiple interactions with downstream signaling molecules and extracellular DA, and these interactions lead DAT to a central role in DA signaling. The resolution of DAT structures enables us to simulate transporters with different drugs or neurotransmitters and estimate the rates of structural transitions at long time scales such as milliseconds, that molecular simulations are not able to reach.

On the cellular level, previous efforts are generally revolved around how DA concentration mediated at the specific regions of the brain, specifically in the striatum and nucleus accumbens (Garris, Ciolkowski, Pastore, & Wightman, 1994). More recent efforts include how the spatial complexity of the system regulates the EC DA, yet no detailed description of the cell morphology and individual transporter/receptor localization has been included in modeling efforts (Block et

al., 2015). However, the complexity of the cell surface and the EC space in the brain is considerably more tortuous compared to a regular cell such as blood cell, and the models that do not include spatial complexity may not be able to provide a proper description of the microphysiology of the DA neurons and EC space.

DAT is the primary target for psychostimulants such as cocaine and amphetamine. The mechanism of action of cocaine is known as competitive inhibition (Beuming et al., 2008). Cocaine binding to DAT blocks the DA translocation pathway. Continued exposure to cocaine leads to an increase in EC DA concentration above the metabolic level, which in turn increases the activity level of DA receptors that trigger reward pathways. AMPH has more complicated interaction with DAT than cocaine. AMPH is transported by DAT into the cell and interacts with various downstream signaling pathways such as Ca^{++} signaling, Rho signaling, and G-protein signaling pathways (Saunders et al., 2000). The activated intracellular signaling pathways regulate the state of DAT and activate DA efflux to the cell exterior which, in turn, affect DA receptor activation. Intracellular signaling is significantly more complicated than extracellular signaling since the number of signaling molecules is considerably more abundant in the cell, and the number of interactions grows exponentially.

Memory and learning are two of the most commonly studied areas in brain research. A mechanism proposed to explain memory and learning is the synaptic plasticity. Synaptic plasticity can be defined as the strengthening or weakening of the interactions depending on the activity patterns of the neuron itself and its neighbors. High input frequencies result in long-term potentiation (LTP) which strengthen the synaptic connectivity, whereas low input frequency causes long-term depression (LTD) which shrink the size of the spine. One of the key molecules in LTP is the calcium/calmodulin-dependent kinase type II (CaMKII). CaMKII is a central piece

of Ca^{++} signaling pathways. It has many connections between several signaling molecules. More interestingly, CaMKII is a large complex, usually assembled as a dodecamer, and its rapid dissociation/association and intramolecular activation properties make it challenging to gain a quantitative understanding of the molecular basis of CAMKII signaling events.

1.1 THE PROBLEM

Modeling DA reuptake and DA neurotransmission are one of the most popular questions, and a significant effort has been made to build a comprehensive model at both cellular and molecular levels (Mortensen & Amara, 2003). In the 1990s, a well-mixed model of extracellular region in the dorsal striatum to predict the time trajectory of DA concentration had been introduced (Garris, 1994). The first DA concentration model with a spatial component is defined as 'volume transmission' (VT) models (Cragg, Nicholson, Kume-Kick, Tao, & Rice, 2001; Cragg & Rice, 2004; Rice & Cragg, 2008; Rice, Patel, & Cragg, 2011; Sulzer, Cragg, & Rice, 2016). VT models assume spatial/volume exclusion/transmission properties as individual parameters. The central message from these models is that the consideration of realistic diffusion and reactions in EC microenvironment significantly affects the model predictions for DA dynamics. However, a detailed model that considers both spatial complexity and localization of DAT has not been developed.

Another determinant of DA dynamic is the spectrum of transitions that take place on a molecular level. The recent resolution of Drosophila DAT enables structure-based simulation studies (Penmatsa, Wang, & Gouaux, 2015). Such simulations provide significant information about the discrete states of DAT and the transitions among these states. The trajectories from the

simulations are not adequate in making predictions on the events on a timescale longer than microseconds, yet they can provide valuable information on the kinetics of conformational transitions.

The advances in imaging technologies and modeling methods in both molecular and cellular level improved the accuracy and specificity of computational models. To have a better understanding of DA neurotransmission, the connection between these two scales using a multiscale modeling strategy is required. The timescale of molecular simulations is generally in the order of nanoseconds to microseconds, which is too short compared to cellular events that happen at much longer timescales such as microseconds to seconds. Also, the length scale of the diffusion of individual neurotransmitters is considerably more significant than the simulation environment that is used in molecular level simulations. Such diffusion events are generally ignored in molecular simulations, and molecular simulations usually place neurotransmitters in the close vicinity of transporter/receptor molecules. A more realistic understanding of such complicated systems is required to identify the defects and develop therapies for various conditions originating from deficiencies in DA signaling.

DAT is the primary target of psychostimulants that are widely studied in the context of drug abuse (Di Chiara & Imperato, 1988). A major inhibitor of DAT is cocaine. Cocaine competitively inhibits DAT function to transport DA. Since cocaine is a potent inhibitor of DAT function, it is generally assumed that cocaine stays on DAT for hours. The effect of DAT recycling on the membrane and the effect of spatial complexity on the cocaine inhibition has not been examined. Another drug that disturbs DA signaling is AMPH. The mechanism of action for AMPH is more complicated than cocaine. AMPH regulates several intracellular down-stream signaling pathways. These complex pathways are generally studied without spatial properties due to the

large copy number of individual molecules. A complete picture of DA dynamics in the presence of psychostimulants is necessary to provide insights to design therapeutics against drug abuse.

CaMKII has a long-lasting activity after initial stimulation by calmodulin and calcium. A mechanism called ‘Calmodulin Trapping’ explains the activity. Quantitative models have been using this mechanism to explain the high activity levels of CaMKII observed even after the completion of stimulation. However, calmodulin trapping blocks the phosphorylation of CaMKII on a secondary threonine site and activation-triggered subunit exchange. A recent experimental study shows that CaMKII can be phosphorylated at two threonine sites and as a result, an activation-triggered subunit exchange on the holoenzymes is observed. A detailed model of CaMKII dynamics in the presence of subunit exchange can show how the activity spreads across CaMKII molecules with the help of activation-triggered subunit exchange mechanism.

1.2 THE APPROACH

This dissertation addresses four main problems: (1) the absence of the binding and transition rates of DAT, (2) the lack of the inclusion of the effect of DA neuronal spatial complexity and heterogeneities in computational modeling of the DA transmission, (3) the lack of complete spatially realistic models for DA signaling under psychostimulants and lastly, (4), the lack of detailed quantitative model of CaMKII interactions to explain activation-triggered subunit exchange.

The first problem has been recently addressed using two rigorous methods (M. H. Cheng, Kaya, & Bahar, 2018): (I) alchemical free energy calculations with free energy perturbation and (II), the potential of the mean force calculations using adaptive biasing force methods to calculate

binding free energies of DA-binding and -unbinding to/from DAT. As an input to these methods, our coworker Dr. Mary Cheng from Bahar lab used a variety of molecular level simulations and generated a total of more than two microseconds long trajectories. As a result, we were able to estimate the energy landscape of DAT and construct a model for the conformational dynamics of DAT.

The second problem has been addressed in three steps. The first step was the reconstruction of the 3D geometry of DA synaptic environment from electron microscopy and fluorescence microscopy images obtained by Dr. Alexander Sorkin and coworkers (Block et al., 2015). I determined the geometry of DAT expressing cells and other neurons by using semi-automated 3D reconstruction algorithm which uses integer programming (Turetken et al., 2016). In addition to geometry, the location of DAT clusters and DA active zones have been identified. The second step was the implementation of the DAT transition kinetics into a spatially realistic model of DA reuptake from DAT and determination of stochastic DA release times using different action potential firing frequencies and patterns. All simulations were performed in MCell, a software developed for spatiotemporally realistic simulations of micro physiological events near CNS synapses. MCell outputs the location of the individual molecules and the number of molecules in specified compartments. Using molecule counts, I estimated the concentration and activation levels of DA receptors. In addition to activation levels, I evaluated the local and global concentration of DA in the EC space. In the third step, I carried out MCell simulations under diverse conditions such as the various distribution of DAT under different DA release patterns. Since MCell is a spatial stochastic simulation tool, it is required to simulate the models for a significantly large number of times to have a proper statistical estimate. Therefore, I repeated the third step for more than 100 times for individual settings. MCell simulations show that the DAT

distribution on the cell membrane and the complexity of the cellular morphology are significant factors for DA reuptake efficiency.

I addressed the third problem by extending the model developed for the second problem with the addition of psychostimulants. First, I studied the effect of cocaine. The mechanism of action of the cocaine only involves the extracellular region. Therefore, I added cocaine molecules with known concentrations to the system and generated trajectories. For AMPH, it is impossible to use a similar strategy since AMPH enters the DAT-expressing cell through DATs and disrupts the intracellular signaling networks. The intracellular signaling networks have many molecules which makes it infeasible to use in spatial stochastic simulation tools such as MCell. To this end, in collaboration with Dr. Bing Liu in the Bahar Lab, I build a multiscale model of AMPH-induced DA efflux model. The effect of localization of the DAT and concentration of AMPH with varying action potential firing patterns are studied. MCell simulations show that spatial complexity does not have a significant effect on the DA reuptake efficiency in the presence of low cocaine concentrations. The effect of AMPH on EC DA concentration is significantly small if the DATs are nonuniformly distributed due to reduced AMPH uptake rate from DAT. On the other hand, the EC DA concentration considerably increased under a uniform distribution of DAT since the AMPH uptake is more efficient and many DAT are phosphorylated and efflux DA.

I approached the last problem by creating a model of CaMKII intra- and inter-subunit dynamics to reproduce the experimental data available at both short-time scales (seconds) and long-time scales (minutes). Since the CaMKII is structurally a dodecamer, there is a need to simulate the system using network-free methods instead of conventional network-based methods. The model calibration was performed using genetic algorithms. The CaMKII is one of the central molecules, and I would like to learn about the activation dynamics. However, I discovered a bottle-

neck in the parameter calibration step. Since the model simulations were not efficient, and the objective function was hard to optimize, I introduced a hybrid model checking/genetic algorithm strategy to overcome the computational problems. Due to technical difficulties in network-free simulations, the suggested hybrid model checking/genetic algorithm strategy did not converge. However, the application of the method on simple models show promising results and about the increase in efficiency with the addition of model checking.

Multiscale models allow us to understand how the components interact with each other and function together, how the functionality is altered when a drug is present, and if a protein is in a dysfunctional state. The molecular modeling part provides a foundation of the dynamics of essential molecules. Cellular simulations integrate data from various sources such as molecular simulations, microscopy studies, and physiological experiments to bridge different scales. The hybrid multiscale models can explain various events that can describe physiology in different length and time scales. Multiscale models enable the adoption of parameters estimated from molecular simulations in higher scale simulations to examine regulatory mechanisms that can affect the cellular system behavior at significantly long-time scales.

1.3 HYPOTHESES AND MAJOR FINDINGS

The main aspects of this dissertation are the introduction of a relationship between events at the molecular and cellular levels for DA neurotransmission, the development of a detailed spatially realistic reaction-diffusion model of DAT release and reuptake, and the construction of a quantitative and detailed model of activation triggered subunit exchange. Using literature data,

answers to the following hypotheses were investigated, and the following significant conclusions were reached:

Claim 1. Spatial complexity of the EC region and the localization of DAT molecules are the two main contributors to DA release and reuptake dynamics under various neuron firing frequencies. The spatially realistic model and MCell simulations provide realistic and time-dependent information on the concentration levels and distribution of DA molecules in the synapses.

Claim 2. The local and global effects of the presence and the dose of the psychostimulants can be identified using spatial stochastic models in connection with large-scale interaction networks generally identified as non-spatial models. MCell simulations provided new insights on the inhibitory effect of cocaine on DA transmission and the complex effects of AMPH on dopaminergic signaling.

Claim 3. The subunit exchange mechanism can explain how low levels of Ca^{++} can activate CaMKII for an extended period of times such as hours. Constructing and calibrating a detailed quantitative model of subunit exchange needs smart parameter estimation methods and network free simulation tools. The intrasubunit interactions and the rates of phosphorylation events should be recalibrated to provide a realistic description of the role of subunit exchange mechanism on CaMKII activation.

1.4 SIGNIFICANCE

DA modulates motor control, cognition, and drug addiction. Understanding the mechanism of dopamine transmission is essential to designing therapies for neurological disorders. I developed

a multi-scale model using advances in imaging and high-performance-computing technologies, which permitted us to perform spatially realistic simulations of DA reuptake. Simulations show large temporal and spatial variations in the local density of DA depending on the morphology of the synaptic/extra-synaptic regions near the DA release site, and on the firing pattern. DA clearance is less efficient under the heterogeneous distribution of DAT compared to the uniform DAT distribution with the same average surface density. DAT membrane distribution, accessibility of DAT dopamine re-uptake transporters outward-facing conformation, and large fluctuations in DA levels emerge as crucial features that modulate dopaminergic transmission. Psychostimulants significantly disrupt the EC DA concentration and DA receptor activity. Cocaine competitively binds to DATs and blocks the DA clearance whereas AMPH disrupts the intracellular signaling pathways and induces DA efflux from DATs. The DAT localization does not have a significant effect on the way cocaine disrupts DA signaling. Instead, the primary modulator is the concentration of the cocaine in the system. A The effect of DAT localization is more significant for the effect of AMPH due to limited uptake of AMPH under nonuniform DAT distribution.

CaMKII is one of the critical nodes in the signaling network which can affect important processes such as neurotransmitter degradation and transcription factor regulation. Structurally, CaMKII is a dodecamer, and each subunit has many functional sites, e.g., calmodulin binding site and phosphorylation regions. The subunit exchange mechanism of CaMKII can explain how the activity of CaMKII lasts for an hour in the absence of stimulation in addition to ‘Calmodulin Trapping’ mechanism. The subunit exchange mechanism is observed significantly later than the CaMKII activation meaning that subunit exchange takes place after CaM is released from the trapped state.

1.5 OVERVIEW

This dissertation is organized as follows:

Chapter 2 provides detailed information on the construction of spatiotemporally realistic model starting from both molecular simulation data and microscopy data. I determined how the variations in the spatial complexity and structural heterogeneity affect the DA reuptake and the EC DA concentration at both local and global levels under various DA neuron firing patterns.

Chapter 3 presents the alterations in the spatiotemporally realistic DA release and reuptake in the presence of psychostimulants such as cocaine and AMPH. The implementation of the model on different scales and the effect of spatial complexity are investigated. The effect of cocaine on the DA signaling depends on the concentration more than the localization of the DAT. Contrary, the primary triggering factor for AMPH induced DA efflux is the process of AMPH uptake. Since the nonuniform distribution of DAT has a low AMPH uptake rate, the effect is minimal under nonuniform DAT distribution. However, there are significant differences in the extents of DA clearance and DA efflux with different DAT distributions. In the end, the two alterations neutralize the total effect.

Chapter 4 presents a detailed quantitative model of activation-triggered subunit exchange for CaMKII. I created the model and performed a parameter scan to check the validity of the model on the experimental data. The initial model does not capture the activation-triggered subunit exchange. Hence we calibrated the model parameters using genetic algorithms. Due to the complex nature of the optimization problem, a scalable heuristic optimization technique with genetic algorithms is used. The genetic algorithms have a significant overhead due to the entire trajectory generation at each step. To increase the efficiency and the accuracy of genetic algorithms, a hybrid

online model checking/genetic algorithm is implemented. The method showed promising results on simple models, but technical issues with the simulation engine prevented application to the CaMKII model.

2.0 HETEROGENEITIES IN AXONAL STRUCTURE AND TRANSPORTER DISTRIBUTION LOWER DOPAMINE REUPTAKE EFFICIENCY

2.1 BACKGROUND

Midbrain dopaminergic neurons have a strong influence on striatum functions such as motor or action planning, cognitive functions, and motivation (Roeper, 2013). Dysregulation of dopaminergic transmission leads to impairment of these activities, resulting in disorders such as Parkinson's disease (PD) (Hoang, 2014), attention-deficit/hyperactivity disorder (ADHD) (Wu, Bellve, Fogarty, & Melikian, 2015), and drug addiction (Nutt, Lingford-Hughes, Erritzoe, & Stokes, 2015). A mechanistic understanding of dopamine (DA) transmission events is essential to developing therapeutic strategies because many behavioral states strongly correlate with DA release and reuptake (Sulzer et al., 2016; Tsai et al., 2009).

DA release to the synapse is activated by excitatory stimulation and exhibits patterns like neuronal firings. DA excitatory signaling proceeds by activation of DA receptors upon binding DA molecules. DA rapidly diffuses from the active zone (*AZ*), or release site, to extra-synaptic regions in the extracellular (EC) medium. DA transporters (DATs) membrane proteins usually located on the surface of presynaptic axon terminals, regulate DA signaling by removing excess DA from extra-synaptic regions (Torres et al., 2003; Vaughan & Foster, 2013). DATs are targets for addictive substances, which inhibit their function (Amara & Sonders, 1998), thus resulting in

excess (neurotoxic) DA levels in the EC region (Di Chiara & Imperato, 1988), whereas low levels of DA cause motor impairments associated with PD (Lotharius & Brundin, 2002). Also, reuptake by DATs, the rate of DA diffusion from the *AZ* to the extra-synaptic region (Taylor, Ilitchev, & Michael, 2013), and the frequency and patterns of action potentials (APs) (Tsai et al., 2009), are known to modulate the efficiency of DA signaling.

The dynamics of DA reuptake by DATs has been a focal topic in modeling efforts, both at the cellular and molecular levels (Mortensen & Amara, 2003). Early efforts at the cellular level adopted a well-mixed model focusing on predicting the DA concentration in some areas of the brain, such as the nucleus accumbens or dorsal striatum (Garris et al., 1994). The effect of EC DA concentration on the activation of DA receptors (Viggiano, Vallone, & Sadile, 2004), as well as spatial/volume exclusion/transmission properties affecting EC DA levels, have been included in later, volume transmission (VT) models (Cragg et al., 2001; Cragg & Rice, 2004; Dreyer, Herrik, Berg, & Hounsgaard, 2010; Dreyer & Hounsgaard, 2013; Rice & Cragg, 2008; Sulzer et al., 2016). These studies highlighted a need for considering the distinctive diffusion and uptake characteristics of the EC microenvironment. No quantitative models/simulations have been developed/performed to date that would permit us to assess how the complex geometry of DA terminals, and the spatial distribution and conformational dynamics of DATs alter dopaminergic signaling. The advances in imaging DA neurons and visualizing individual DATs (Block et al., 2015) now enable us to reconstruct *in silico* the detailed morphology near *AZ*s, and examine the time evolution of DA release and reuptake with the help of MCell, a software initially developed (Czech, Dittrich, & Stiles, 2009; Kerr et al., 2008; Stiles, Van Helden, Bartol, Salpeter, & Salpeter, 1996) for spatiotemporally realistic simulations of synaptic signaling events.

In addition to cellular structure and heterogeneities, the conformational dynamics of DATs is a determinant of DA transport efficiency. Recent crystal structures of *Drosophila* DAT (dDAT) (Penmatsa et al., 2013; Penmatsa et al., 2015; Wang et al., 2015), have opened the way to structure-based studies of DAT dynamics. Simulations based on these structures helped elucidate the sequence of molecular events that take place during the transport cycle of the human orthologue, hDAT (Mary Hongying Cheng & Bahar, 2015; Mary Hongying Cheng, Torres-Salazar, Gonzalez-Suarez, Amara, & Bahar, 2017; Huang & Zhan, 2007; Khelashvili et al., 2015; Razavi et al., 2017). We are now able to make reasonable approximations for the kinetic scheme and parameters associated with the DAT transport cycle based on statistical analyses of the full-atomic trajectories and free energy calculations.

Here, I present an integrated model of synaptic signaling in DA neurons developed from cellular and molecular structures and molecular dynamics. We investigate the effects of (I) the conformational kinetics of DATs, (II) the spatial complexity of DA terminals and *AZ*s based on fluorescence images, (III) the firing patterns, phasic *vs* tonic and (IV), the heterogeneous distribution of DATs on the plasma membrane based on experimentally observed DAT density fluctuations. Simulations reveal the strong dependency of local DA levels as well as overall DA clearance efficiency on the local geometry of axon terminals. They also reveal that the presence of DAT clusters (consistent with the DAT density heterogeneities observed in high-resolution images (Block et al., 2015)) causes a reduction in the efficiency of DA reuptake compared to uniformly distributed DATs with the same average surface density. This effect becomes more pronounced with increasing heterogeneity of the surface distribution of DATs.

2.2 METHODS

2.2.1 Confocal imaging of immunolabeled DATs in transgenic mouse brains

The procedure for preparing and imaging acute brain slices from transgenic knock-in mice of either sex expressing DAT molecules tagged with the hemagglutinin-A (HA) epitope (HA-DAT; (Rao, Richards, Simmons, Zahniser, & Sorkin, 2012) has been described in previous works (Block et al., 2015; Rao, Sorkin, & Zahniser, 2013). Briefly, brains were submerged into an ice slush of oxygenated artificial cerebrospinal fluid, and 0.8 mm thick sagittal slices were cut using microtome blades and a stainless-steel slicing block. The subcellular localization of cell-surface HA-DAT molecules was deduced from intact living DA neurons in acute sagittal brain slices as detected by mouse anti-HA antibodies with Cy3-conjugated anti-mouse antibodies (Block et al., 2015). Slices were incubated in artificial cerebrospinal fluid (ACSF) at room temperature with one µg/ml mouse anti-HA antibodies for 1 hour. After removing unbound antibodies, slices were incubated for one hour at 4°C in ACSF with 2.5 µg/ml Cy3-conjugated anti-mouse Fab fragments.

Dr. Sorkin and coworkers have not observed substantial differences in HA-DAT distribution between live-cell and post-fixation labeling with HA antibodies, suggesting that axonal varicosities revealed by DAT staining were not the result of blebbing during the labeling procedure of live slices. The binding of antibodies to live neurons followed by fixation provides much superior image quality and lower signal-to-noise ratio as compared to the conventional protocol of fixation first and then staining with antibodies. Importantly, live-neuron staining protocol allows labeling of cell-surface DATs, which is essential for defining the distribution of DATs on the neuronal surfaces in the model. Observations of DAT endocytosis (Block et al.,

2015), normal lateral membrane mobility of DAT, and healthy mitochondria in dopaminergic neurons from slices kept alive for at least two hours were indicative of functional neurons in these slices. Moreover, DA neurons labeled as described above have been observed to exhibit pH-dependent vesicular trapping of antipsychotic drugs (Tucker, Block, & Levitan, 2015).

Dr. Sorkin and coworkers obtained high-resolution 3D images of DA neurons, and a z-stack of 18 confocal images at 400 nm interstack distance was acquired 10 µm deep from the cut face of the slice through the 561 filter channel using a spinning disk confocal system based on a Zeiss Axio Observer Z1 inverted fluorescence microscope (with 63x Plan Apo PH NA 1.4 objective), equipped with a computer-controlled Spherical Aberration Correction unit, Yokogawa CSU-X1, Vector photo manipulation module, Photometrics Evolve 16-bit EMCCD camera, Hamamatsu CMOS camera, environmental chamber, and piezo stage controller and lasers (405, 445, 488, 515, 561, and 640 nm), all controlled by SlideBook 6 software (Intelligent Imaging Innovation, Denver, CO).

The image reconstruction and modeling described below are based on the combined use of slices of light microscopy images and electron microscopy images (Block et al., 2015) (Block et al., 2015) that were obtained on intact animals after cardioperfusion fixation by Sorkin and coworkers.

2.2.2 *In silico* reconstruction of DA axonal terminals in the striatum

I reconstructed *in silico* a 10 µm x10 µm x 7.2 µm volume from the above described striatal region using a semi-automated 3D reconstruction algorithm (Turetken et al., 2016). The 3D reconstruction algorithm uses integer programming to suggest the connections between the borders

of the cell membrane on each confocal image. Manually, suggested cells are a match, and the 3D geometry of DAT-expressing cells are generated. A detailed description of the reconstruction method is available in Fiji tutorials (ImageJ). The size of the simulation box was large enough to allow for the diffusion of DA over a sufficiently broad EC region, in accord with previous estimates (Venton, Michael, & Wightman, 2003), and the reconstruction yielded a realistic representation of both the heterogeneous shape of axonal terminals and the surface distribution of individual DAT molecules.

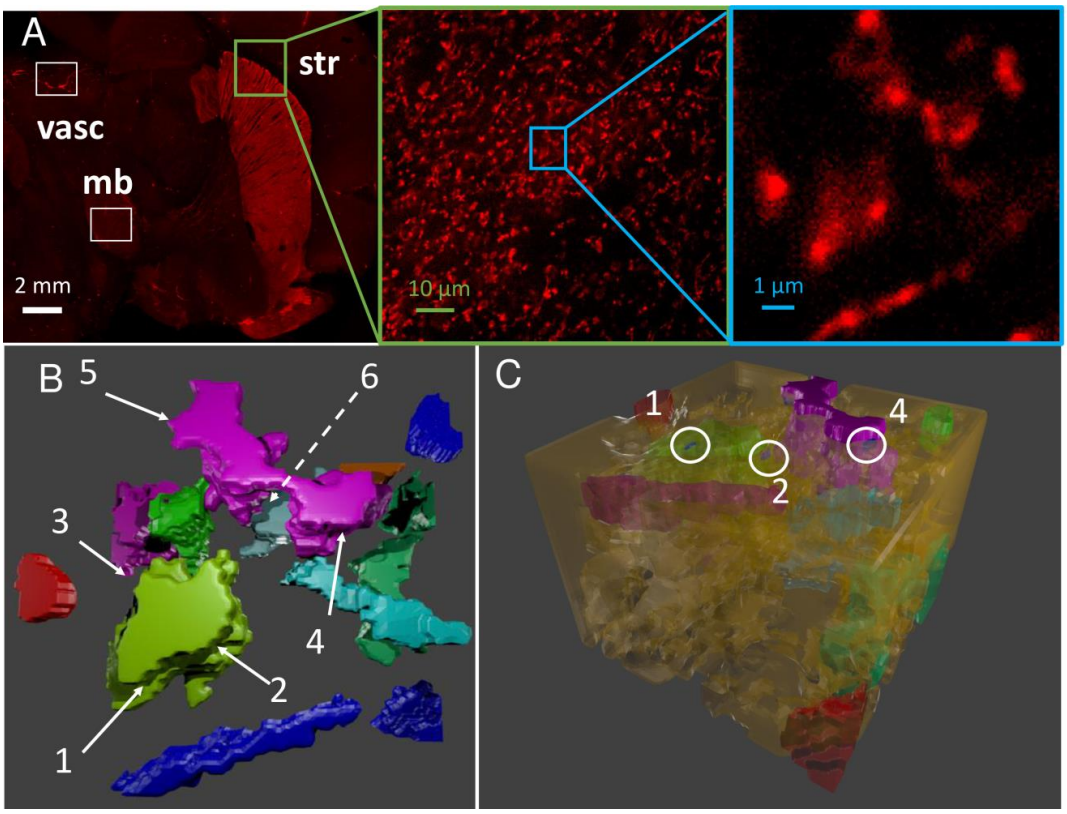

Figure 1. Reconstruction of the morphology of DA neuronal axons

A, HA-DAT distribution in different regions of mouse brain including midbrain (mb) and striatum (str) acquired from sagittal slices. The slices were labeled with HA11 antibody detected with Cy3-conjugated Fab IgG fragments (HA, red). Nonspecific staining of the vasculature (vasc) is also highlighted. White scale bar, 2 mm. B, Maximal-projection image of the first five (starting 10 m deep from the edge of the slice) confocal sections of the 3D image from the striatal region. The slice labels are same as those in A. Green scale bar, 10 m. C, Maximal projection of the first five sections of 3D image of the small striatal region, used to construct the simulation environment (inset), magnified from B. Blue scale bar, 1 µm. D, 3D reconstruction of the region shown in C, visualized using CellBlender (Bartol, Keller, et al., 2015), an add-on for Blender 2.78 (http://www.blender.org). Different colors refer to 13 different axonal varicosities (DA terminals). Cells that do not express DAT occupies the remaining portions. The location of six *AZ*s is shown by the labels 1– 6. The dashed line indicates an *AZ* that is not visible from this perspective. E, Full isometric view of the simulation box. White circles indicate the locations of three *AZ*s.

Table 1. Geometric characteristics of axon terminals reconstructed for simulations.

Subsystem		**V(μm)^3**	**Surface area (μm)^2**	**Available [3] Surface area (μm)^2**
DA axons	Terminal 1	1.22	6.8	5.47
	Terminal 2	24.63	59.47	53.83
	Terminal 3	3.53	20.18	18.03
	Terminal 4	15.84	56.33	51.11
	Terminal 5	4.72	25.14	25.14
	Terminal 6	1.71	10.12	10.12
	Terminal 7	0.82	5.57	5.57
	Terminal 8	2.04	12.94	12.94
	Terminal 9	15.32	46.86	39.08
	Terminal 10	15.18	58.65	55.5
	Terminal 11	3.85	18.99	18.98
	Terminal 12	9.69	34.31	31.75
	Terminal 13	2.58	12.35	9.64
	Total	101.03	367.71	337.16
Non-DA expressing cells		463.62	1058.00	0
DA axons + other cells		**564.65**	**1425.71**	**337.16**
Available EC volume [2]		**155.35**		

The reconstructed region contained 13 axon terminals (Figure 1B). The corresponding volumes and surface areas (listed in Table 1) were calculated using the NeuroMorph (Jorstad et al., 2015), a Blender add-on that uses triangular meshes to evaluate the surface area and corresponding normal to determine the volume of each tetrahedron. The total volume occupied by the 13 axon terminals was 101.03 μm^3, and the corresponding total surface area, 337.16 μm^2.

The DA axonal terminals reconstructed *in silico* contained six varicosities, i.e., 3D globular regions with densely expressed DATs, distributed over three DA terminals: one of the largest terminals had three varicosities, another had two, and the remaining varicosity was on a third terminal. *AZ*s lie within varicosities but are not usually populated with DAT molecules (Block et al., 2015); accordingly, sub-regions (of varicosities) which lacked DAT molecules within at least a 50 nm radius were identified as *AZ*s. The region between DAT-expressing cells (detected by fluorescence microscopy) and others, (not visible), was represented by an interstitial (void) space of 30 nm thickness surrounding the DAT-expressing terminals (Figure 1E). The void fraction is calculated as 0.21, consistent with previous estimates (Cragg et al., 2001), or an overall volume of 155.35 μm^3 (Table 1) that formed the available for DA diffusion. These narrow regions form the synaptic clefts and extra-synaptic regions available for the diffusion of DA molecules. The number of *AZ*s for a given volume was verified to be comparable to that used in other studies (Dreyer et al., 2010).

2.2.3 Distribution of DATs on the axonal surfaces

Next, I proceeded to the placement of DAT molecules on the membrane of axonal terminals. To investigate the effect of DAT surface distribution heterogeneities on the efficiency of DA reuptake, I examined four cases (Figure 2). Case 1 refers to the uniform distribution (Figure 2A), taken as $\rho(DAT) = 800/\mu m^2$, based on the electron microscopy images of gold particle labeled HA-DAT, assuming 10% labeling efficiency (Block et al., 2015). Case 2 is a non-uniform (bimodal) distribution (Figure 2B), outlined in accord with the actual distribution of DATs observed in experiments. High-density regions were detected in the fluorescence images, as continuous bright regions (Figure 1C). These regions covered ~10% of the plasma membrane area, and

approximately 90% of DATs were localized in these regions. The surface densities of DATs in the high- and low-density regions were taken as ρ_h = 6,339/μm^2 and ρ_l = 50/μm^2, respectively.

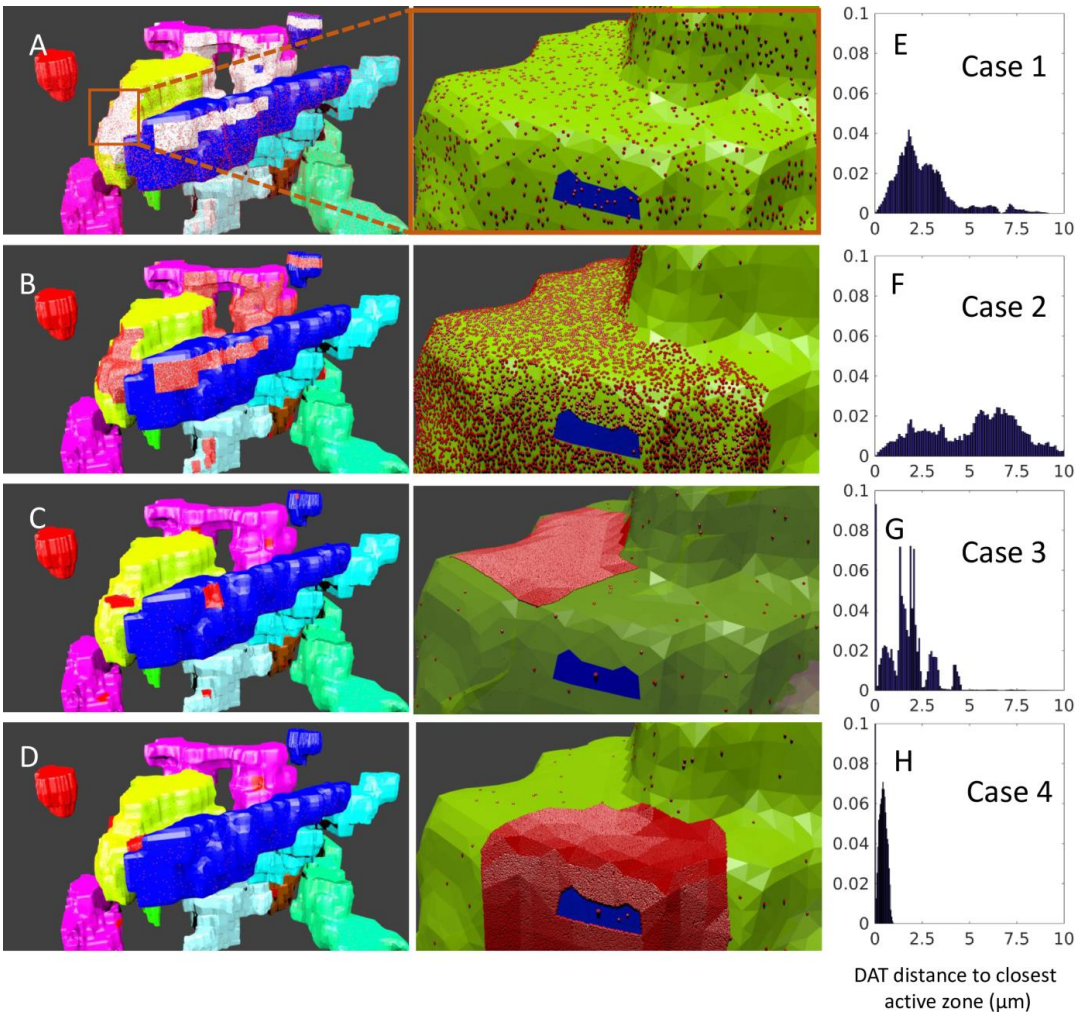

Figure 2. Four space-dependent models of different plasma distributions of DATs

A–D, Distant (left) and magnified (right) view of the axon terminals in cases 1– 4. Each color shows a different terminal, and the red dots represent the DATs. The white regions in A represent the regions with high fluorescence intensity, and those regions are filled with a high density of DATs (red dots), magnified in B, where the blue region shows the *AZ*. The red patches in B–D illustrate high-density regions where 90% of DATs are clustered. E–H, Distance distribution of DATs to closest *AZ* center, from 140 independent simulations.

Table 2. Parameters and properties used in MCell simulations

Parameter	Value	Unit	Reference
DA diffusion coefficient	4.00×10^{-6}	cm^2/s	(Rooney & Wallace, 2015)
Vesicle release probability	0.06		(Dreyer et al., 2010)
The average firing rate of DA neurons	4.00	Hz	
# of DA released per release event	3,250		(Pothos, Davila, & Sulzer, 1998)
OF → OF* rate constant (k_{12})	9.60×10^6	$M^{-1}s^{-1}$	(M. H. Cheng et al., 2018)
OF* → IF* rate constant (k_{23})	20.00	s^{-1}	
IF* → IF rate constant (k_{34})	5.00	s^{-1}	
IF ↔ OF forward rate constant (k_{41})	2.00	s^{-1}	
IF ↔ OF reverse rate constant (k_{14})	8.00	s^{-1}	
Total axonal surface area	337.16	μm^2	(Block et al., 2015)
Uniform DAT surface density, ρ(DAT)	800	$1/\mu m^2$	
High DAT surface density, ρ_h(DAT)	6,339	$1/\mu m^2$	
Low DAT surface density, ρ_l(DAT)	50	$1/\mu m^2$	
Very high DAT surface density, ρ_{h2}(DAT)	30,000	$1/\mu m^2$	

DA density of neurons, I_{DA}	9.3	$\mu g/cm^3$	(Bannon, Michaud, & Roth, 1981)
The ratio of the total DA released per AP	0.05%		(Gubernator et al., 2009)
Density of DA terminals, ρ_{term}	0.104	$1/\mu m^3$	(Doucet, Descarries, & Garcia, 1986)

In Case 3, the distribution is again bimodal, similar to Case 2, but the central parts of the high-density regions from Case 2 are selected as the new very-high-density regions, with ρ_{h2} = 30,000/μm^2; and ρ_l = 50/μm^2 elsewhere, which leads to a sharper heterogeneity in the spatial distribution of DATs (Figure 2C). In Case 4, DATs are assumed to be clustered in the immediate neighborhood of *AZ*s, as a mimic for conventional synaptic models where DATs act as gatekeepers near the synaptic cleft (Figure 2D) (Danbolt, 2001; Rothstein et al., 1994); and DAT surface concentrations in high- and low-density regions are the same as in Case 3. The histograms in Figure 2E-H describe the probability distribution of the distances of DAT molecules from the closest *AZ*.

2.2.4 MCell simulations of DA release and reuptake events in DA neurons

Spatiotemporally realistic simulations were performed using MCell (Kerr et al., 2008; Stiles et al., 1996), a 3D reaction-diffusion system solver that allows users to reconstruct complex geometries, define the subcellular localization of discrete molecules, and simulate their dynamics. There are four levels in the MCell simulation algorithm. The first level is the diffusion of the molecules in 2D and 3D. For diffusion of volume molecules, the direction and the length of the diffusion path

is determined using Monte Carlo methods. The probability distribution of the length of diffusion for a given time step is determined using the following equation:

Equation 1

$$\rho(r,t) = \frac{1}{(4\pi Dt)^{e/2}} e^{-r^2/4Dt}$$

where (r) is the distance a volume molecule traveled at the time step (t) and (D) is the diffusion coefficient of the volume molecule. For determination of the direction of the diffusion, two angles for the spherical coordinates are calculated. First, the azimuthal angle ϕ is sampled from a uniform distribution between 0 and 2π. The distribution for the polar angle is sinusoidal and generated using inverse transform sampling. The surfaces in MCell are divided into triangular tiles. In the 2D diffusion, like the 3D diffusion, a direction is selected in the plane of the tile that molecule resides. The molecule diffused in 2D using the similar strategy that is described for volume molecules. When the molecule changes a tile, the direction vector is transformed to the local coordinate system on the next tile. The second level of the simulation algorithm is the collision detection step. The collision detection is performed completely based on the distance between molecules. If the distance between two particles is less than a predefined collision radius, the molecules are evaluated for a bimolecular reaction. The third level of the MCell algorithm is the evaluation of bimolecular reactions. The propensity of each reaction is calculated using the bulk rate of each reaction. To obtain the correct bulk rate, a proper probability of reaction per collision should be selected. This value is determined by the following formula:

Equation 2

$$p = \frac{k}{A} f(D,t)$$

where (k) is the observed reaction rate, (A) is the tile area or cross-section of 3D diffusion. For surface volume reactions the probability per collision is defined as:

Equation 3

$$p = \frac{k}{A}\left(\frac{\pi\Delta t}{D}\right)^{\frac{1}{2}}$$

For the surface to surface reactions:

Equation 4

$$p = \frac{k}{A}\Delta t$$

For the volume to volume reactions:

Equation 5

$$p = \frac{k}{4A}\left(\frac{(\pi\Delta t)^{1/2}}{{D_1}^{1/2} + {D_1}^{1/2}}\right)$$

If the calculated probability is larger than 1, the reaction becomes diffusion limited, and if the collision occurs, the reaction is triggered. If the molecules are not part of a reaction, they can be part of unimolecular reactions. The fourth step of the MCell algorithm is the unimolecular reactions. In MCell, when a molecule is created, the time of next unimolecular reaction is identified using Gillespie's stochastic simulation algorithm. If the molecule does not undergo a bimolecular reaction, a unimolecular reaction occurs at the time calculated at the creation time.

There are a lot of diffusion and reaction parameters in MCell simulations, and the parameters used in the simulations are given in Table 2. Unimolecular reactions are scheduled according to defined

reaction rates, and bimolecular reactions occur with predefined probabilities that are chosen to match bulk reaction rates. Collisions between molecules are detected by ray tracing algorithm. We adopted Neumann boundary conditions like those used in recent simulations of Ca^{++} signaling (Bartol, Keller, et al., 2015), i.e., DA molecules are subjected to reflective boundary conditions at the simulation box walls. In addition, to reduce the bias from reflective boundaries, terminals within 1 μm from the box boundary were assumed to be inactive, such that the available surface area on DA axon terminals was 337.16 μm^2 (see Table 1). A detailed description of the MCell algorithm is provided in Appendix A.

The probability of a release succeeding an action potential depends on multiple factors (Dreyer et al., 2010), including the content of DA in the striatum (I_{DA}) (Bannon et al., 1981), the ratio of the amount of total DA released per action potential (R) (Gubernator et al., 2009), the volumetric density of DA terminals at *AZ*s (ρ_{term}) (Doucet et al., 1986) and the number of DA molecules released per quantum (N_0) (Pothos et al., 1998). The parameters are given in Table 2, which yielded a release event probability of 6% (Dreyer et al., 2010). Each *AZ* has a release site located at its center; and upon a release event, a total of N_0 DA molecules is assumed to be released from the release site. The MCell algorithm is applied to DA molecules with a fixed time step of Δt = 0.1 μs. The distribution of DA step sizes yielded an average of 13.3 nm using a DA diffusion coefficient of 4 x 10^6 cm^2/s. A time-step of 100 μs was used for the slow events such as the transition of DAT to reuptake-ready (EC-exposed outward-facing) state. 140 independent runs, each of 10s, were performed to extract statistically significant results.

2.2.5 Conformational dynamics of DAT

The recent dual-boost accelerated molecular dynamics (aMD) (Hamelberg, de Oliveira, & McCammon, 2007; Miao, Nichols, Gasper, Metzger, & McCammon, 2013) and conventional MD (cMD) simulations of DAT dynamics performed by Dr. Mary Cheng in the Bahar Lab showed that the DA transport cycle by DAT can be approximated by four necessary steps (Figure 3) (Mary Hongying Cheng & Bahar, 2015; M. H. Cheng et al., 2018): (1) recognition and binding of DA (and co-transported Na^+ ions) from the EC region to DAT in the outward-facing (OF) state. We designate the substrate- and Na^+-bound (or loaded) OF state as OF*; (2) global structural change of DAT from OF* to inward-facing loaded (IF*) state; (3) release of cargo to the IC region (IF* → IF); and (4), reverse transition of the unbound/apo DAT from IF to OF state. The respective forward rate constants are denoted as k_{12}, k_{23}, k_{34}, and k_{41}, and reverse rate constants are k_{21}, k_{32}, k_{43}, and k_{14} (Figure 3).

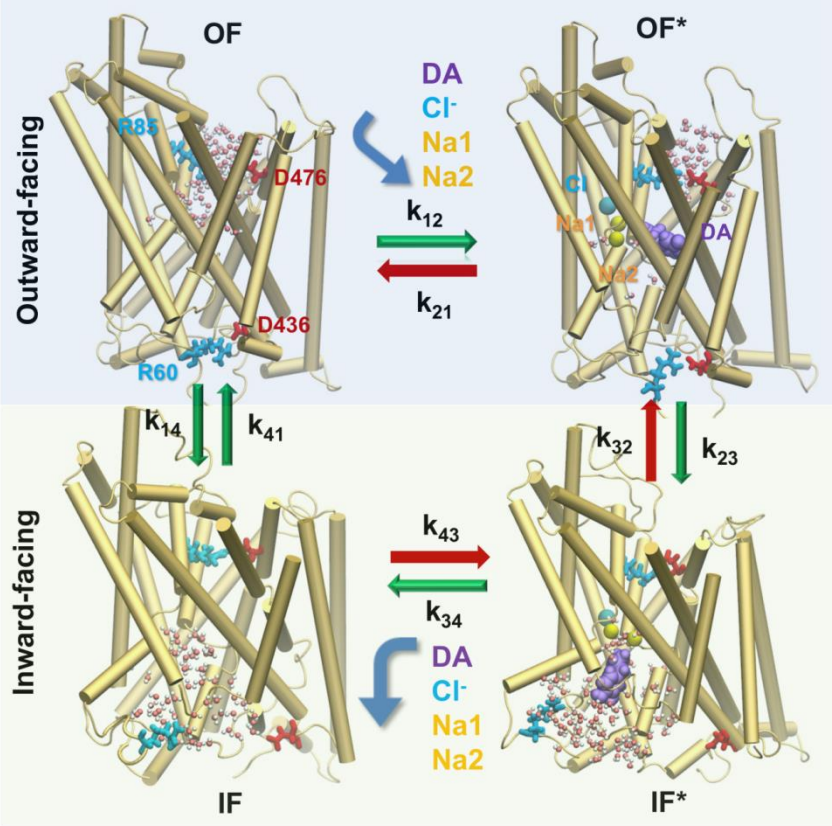

Figure 3. Schematic representation of the sequence of events occurring during the transport cycle

A succession of four major states is observed in MD simulations: unbound and DA/ion-bound outward-facing states (OF and OF) followed by unbound and bound inward-facing states (IF and IF). The corresponding hydration patterns (water molecules in white and pink spheres) and interactions of intra- and extracellular gating residues (R85-D476 and R60-D436, respectively, in stick representation) are displayed. Green arrows indicate the transitions that were observed and evaluated in molecular simulations (see Table 2). The events indicated by the red arrows were unlikely (k_{21}) or not observed (k_{32} and k_{43}) in MD runs. Curved arrows refer to the binding or unbinding of DA (purple, space filling), cotransported Na ions Na1 and Na2 (yellow spheres), and the chloride ion (blue sphere).

The molecular events of DA binding and unbinding to DAT generally involve local conformational changes, and their energetics can be estimated using established free energy calculation methods. Two methods have been used: (I) alchemical free energy calculation with

free energy perturbation (FEP) method (Pohorille, Jarzynski, & Chipot, 2010), and (II), potential of mean force (PMF) calculations using the adaptive biasing force (ABF) method (Chipot & Hénin, 2005), based on cMD trajectories. The FEP calculations yielded a binding free energy change of $\Delta G_{bind} = -7.8$ kcal/mol (M. H. Cheng et al., 2018) in excellent agreement with the experimental value of −7.4 kcal/mol (Dar, Metzger, Vandenbergh, & Uhl, 2006; Huang & Zhan, 2007). MD simulations indicated that the average time required to bind DA molecule originally placed at a distance of 15 Å from the binding site is approximately 125 ns. To convert this number into the binding rate constant k_{12}, we performed the following: First, using an EC DA concentration,7.5 nM (Feifel, Shilling, Kuczenski, & Segal, 2003) we calculated the density of DA molecules to be 7.5 10^{-9} moles/nm^3 x 6.02 x 10^{23} molecules/moles = 4.5 x 10^{-9} molecules/nm^3. The free volume (excluding that occupied by DAT itself) for DA translocation originally located at a separation of 15Å from the binding is evaluated to be 2 nm^3 using POVME (Durrant, de Oliveira, & McCammon, 2011). The number of DA molecules colliding with DAT based on this accessible volume is 2 nm^3 x 4.5 x 10^{-9} = 9 x 10^{-9}, which also represents the prior probability/frequency of collision of a given DA molecule. This leads to an effective binding time of 125 ns / 9 x 10^{-9} = 13.88 s. By normalizing with respect to EC DA concentration, the bimolecular reaction constant is determined as (1/13.88 s) / 7.5 x 10^{-9} = 9.6 x 106 $M^{-1}s^{-1}$.

Dr. Mary Cheng and I further observed that (I) the binding of Na+ ions was fast (< 100 ns) and the subsequent binding of DA readily prompted the closure of the EC gate such that the escape of DA (and ions) back to the EC region was negligibly small, i.e. $k_{21} << k_{12}$; (II) no DA efflux to EC region was detected (i.e., $k_{43} = k_{32} \approx 0$); (III) the DA-free (with Na^+/Cl^- bound) OF→IF transition (k_{14}) was two to three times slower than that in the DA-loaded transition (k_{23}); Na^+- and substrate-binding allosterically promoted a cooperative transition to IF* state (Cheng and Bahar, 2015;

Bahar et al., 2015), but such cooperativity was not observed in the apo state, and (IV), the DA-free IF→OF transition (k_{41}) was even slower than the OF→IF transition (k_{14}) due to the difficulty in closing the intra-cellular gates (M. H. Cheng et al., 2018). The *global* OF ⇔ IF transition rates were thoroughly examined in microseconds aMD simulations of DA-free DAT, which showed that the population of reuptake- ready (OF) conformers was lower than that of IF (or other intermediate) conformers by a factor of 4, or $k_{14}/k_{41} \approx 4$ (M. H. Cheng et al., 2018). These considerations provided us with robust information on the relative rates of the individual steps and led to the rate constants in Table 2, the absolute values of which were verified to be compatible with experimentally observed turnover rates and steady-state concentrations of DA molecules.

To investigate the sensitivity of DA reuptake efficiency to DAT conformational kinetics, we also performed global sensitivity analysis with respect to rate constants in Figure 3. We performed 729 independent runs with different combinations of k_{12}, k_{23}, k_{34}, k_{41}, and k_{14}, which we varied by three orders of magnitude. The results are presented in Figure 4. Each blue dot represents the outcome, EC DA concentration in the simulation box, $[DA]_{EC}$, from one run. A broad range of $[DA]_{EC}$ values, from 0.1 nM to more than 100 nM, are observed. Yet, an increase in DA binding rate k_{12} results in a more efficient clearance and thereby lowers the DA levels in the EC region (Figure 4A). A similar trend is detected with an increase in the transition rate k_{41} from IF to OF, which exposes more reuptake-ready DATs to the EC region (Figure 4C), and the reverse transition induces the opposite effect (Figure 4D). An even sharper effect is observed upon plotting $[DA]_{EC}$ against the ratio k_{14}/k_{41} highlighting the importance of the equilibrium population of the OF and IF states of DAT after releasing its cargo (Figure 4E). The examination of the relative effects of DA binding (k_{12}) versus back transition to the IF state (k_{14}) for the OF DAT also indicates that the OF DAT level is a major determinant of $[DA]_{EC}$ (Figure 4F). Further quantitative

assessment of the statistical significance of these observations using Spearman rank correlation coefficients confirmed that the binding rate constant k_{12} and the ratio k_{14}/k_{41} are two major determinants of DA clearance efficiency. No clear effect was seen for k_{23} (Figure 4B) or k_{34} (data not shown).

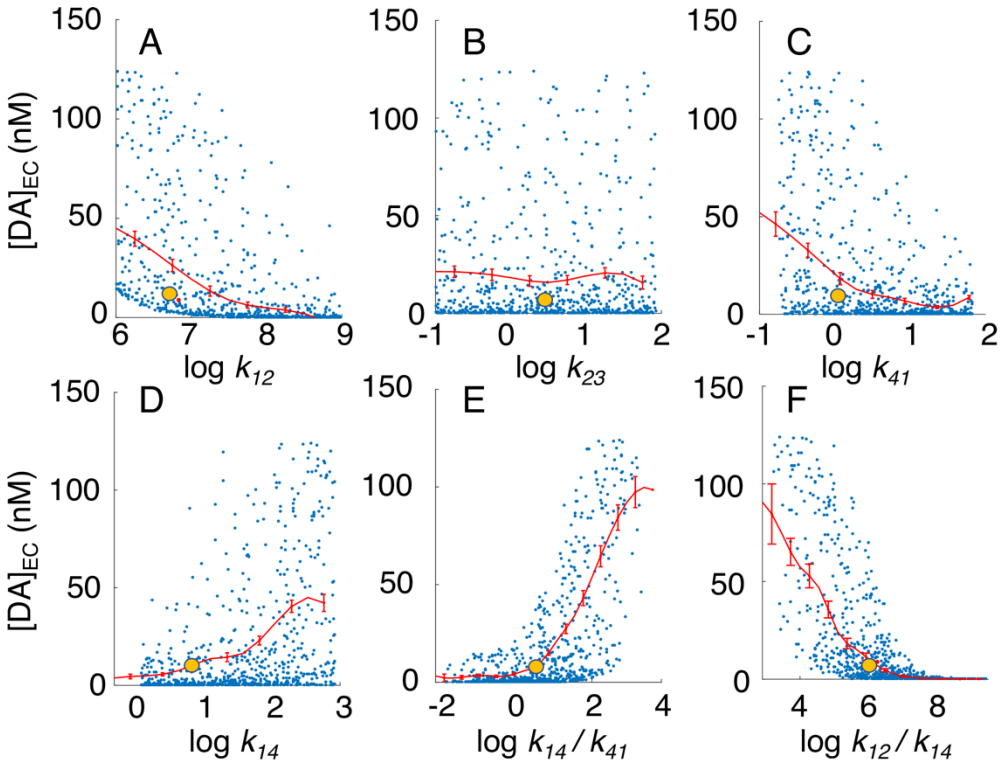

Figure 4. Results from global sensitivity analysis performed for kinetic parameters representing DAT conformational dynamics

Yellow dots represent the default parameters used in the present study, and blue dots show the results obtained by using as random input combinations of the parameters (k_{12}, k_{23}, k_{34}, k_{41}, and k_{14}) and their ratios. Results for k_{34}, which are very similar to those for k_{23}, are not shown. The red curves indicate the mean values and the standard error for successive bins of width 0.5. The Spearman correlation coefficients are – 0.71, 0.01, – 0.01, – 0.44, 0.44, 0.63, and – 0.48, in the six respective panels.

2.3 RESULTS

2.3.1 *In silico* turnover and $[DA]_{EC}$ at half-maximal-rate conform to experimental data

We first verified that MCell simulations yielded macroscopic properties consistent with experimental data. We calculated the turnover rate by adopting in simulations, the same protocol as that adopted in experiments (Rao et al., 2013): multiple runs are performed for a series of initial concentration of DA in the EC region, $[DA]_0$, and in each case, the mass of DA molecules transported per unit time is measured. The number of DA molecules transported per second, V_{max}, under saturation conditions ($[DA]_{sat}$ is of the order of tens of μM) is used to evaluate the turnover rate as the ratio of V_{max} to the total number B_{max} of DAT molecules present in the system. In a simulation environment, $B_{max} \approx 220{,}000$, based on fluorescence microscopy data (Block et al., 2015). To evaluate the turnover rate *in silico*, we counted the number of DAs transported as a function of $[DA]_0$ and examined for each concentration the number of DAs translocated per second. This led to a reuptake rate of 1.2×10^5 DAs/s at saturation (V_{max}). Division by B_{max} gave a turnover rate of 0.55/s, which is comparable to the reported values of 0.2/s (Rao et al., 2013), 0.9/s (Prasad & Amara, 2001) and 1.8/s (Beuming et al., 2008; Prasad & Amara, 2001; Rao et al., 2013).

The average DA level in the EC medium, $[DA]_{EC}$, observed in silico after reaching steady-state conditions was 7.8 nM (Figure 5A). The physiological concentration of DA in the striatum varies between 5 nM and 50 nM (Owesson-White et al., 2012), consistent with the large fluctuations (of the order of $\Delta[DA]_{EC} \approx \pm 10$ nM) we observed in $[DA]_{EC}$. Note that the saturating concentration for DATs is estimated to be ~ 10μM (Prasad & Amara, 2001; Rao et al., 2013).

Simulations yielded a substrate concentration at half-maximal-rate, Km value, of 2.2 µM, which falls within the broad range of reported experimental values of 50 nM to 6.6 µM (Beuming et al., 2008; Prasad & Amara, 2001; Rao et al., 2013). These data confirm that the MCell model and simulations reproduce macroscopic quantities consistent with observables such as the average DA concentration in the EC region at half maximal rate, and the overall turnover rate. We now proceed to a closer examination of microscopic properties.

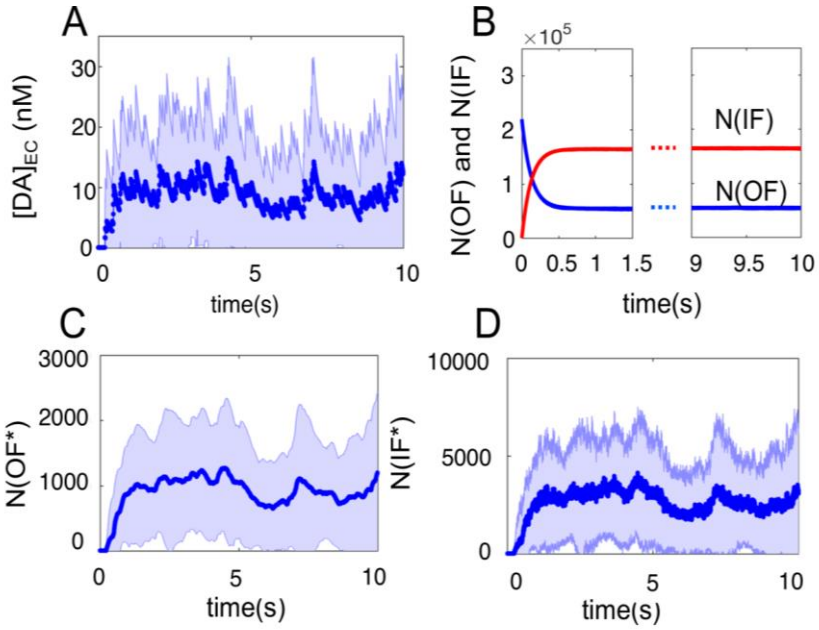

Figure 5. Time evolution of DA concentration and DAT conformational states averaged over 140 independent MCell runs

A, Extracellular DA concentration, $[DA]_{EC}$. The average concentration reached under steady-state conditions is 7.8 nM, and the standard deviation of the concentration is indicated by the shaded region is $[DA]_{EC}$ 10 nM. B, the number of DAT molecules, in the unbound inward- or outward-facing state (IF: red; OF; blue), denoted as N(IF) and N(OF), respectively, as a function of time. C, D, The average numbers of DATs in substrate-bound OF and IF states, N(OF) and N(IF), respectively. The light blue bands show the variance observed in multiple simulations.

2.3.2 DAT conformers reach a dynamic equilibrium within hundreds of milliseconds.

First, I examined the equilibration of the simulated system under the uniform surface distribution of DAT molecules on the axonal membrane. The four snapshots in Figure 6 illustrate the initial DA release events and the gradual equilibration of the conformational states of DATs. All DAT molecules are assumed to be in the OF state at $t = 0$ (*white dots* on the surface of the terminals). Simulations start with a first release event (at *AZ* 1; Figure 6A), followed by firings with Poisson distribution. The released DA molecules (*red dots*) rapidly diffuse to the vicinity of the release site, as illustrated in the snapshots at $t = 1$ and 5 ms (Figure 6B-C). At $t = 700$ ms, we observe a broad spatial distribution of DA (Figure 6D).

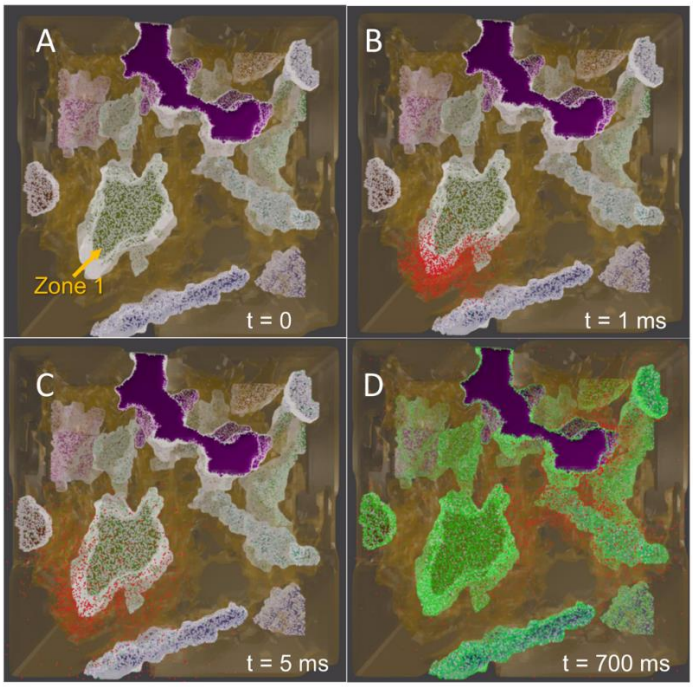

Figure 6. Snapshots from MCell simulations of DA release and reuptake by DATs on DA terminals.

Snapshots from an equilibration simulation of 1 s, initiated by a release event at t=0, and followed by AP firings at 4-Hz frequency are displayed, visualized using Blender. Color code: red, DA; white, OF DAT; green, IF DAT. The purple region shows an axon terminal that is inactive during the simulations. Initially, all DATs are in the OF state (A). A release event at 1 ms is shown in B, and another at 5 ms (C), where most of the DATs reside in the OF state. DA molecules diffuse to extra-synaptic regions in 10 ms. D, the high population of DATs in the IF state reached 700 ms.

Figure 6D shows that most of DATs reside in the IF state (colored *green*) at t = 700 ms. This is consistent with the equilibrium probabilities of the four DAT conformers (19.86% OF, 79.90% IF, 0.05% OF* and 0.19% IF*) which is reached within 500 ms. Figure 5B-D displays the time evolution of the population of the different states of DAT averaged over 140 independent runs of 10s duration each. Most of the DATs fluctuate between unbound OF and IF states, while the bound states (OF* and IF*) are short-lived. Due to their scarcity, the numbers of DATs in IF*

and OF* states show significant fluctuations during simulations (indicated the *light blue band* in Figure 5C-D).

2.3.3 DA levels exhibit large fluctuations depending on AZ structure and DAT surface distribution

I presented in Figure 5A the time course of the DA concentration in the EC region, $[DA]_{EC}$, averaged over 140 runs, which exhibited a standard deviation of ~10 nM about the mean value of 7.8 nM. These are *global* fluctuations, i.e., they refer to the average behavior of the overall microenvironment simulated by MCell. A look at *local* time- and space-resolved patterns of DA levels, on the other hand, reveals even broader fluctuations depending on the *AZ* and space- or time-window examined.

The curves in Figure 7A display the time evolution of the local concentration, $[DA]_{local}$, within a spherical shell of 1.5 μm thickness, with respective inner and outer radii of 1 μm and 2.5 μm (i.e. $1 \leq r < 2.5$ μm) centered at the release site, following a release event from the release site on each of the 6 *AZ*s. Results represent the averages over multiple release events (140 per *AZ*) observed within the time interval $0 < t < 40$ ms.

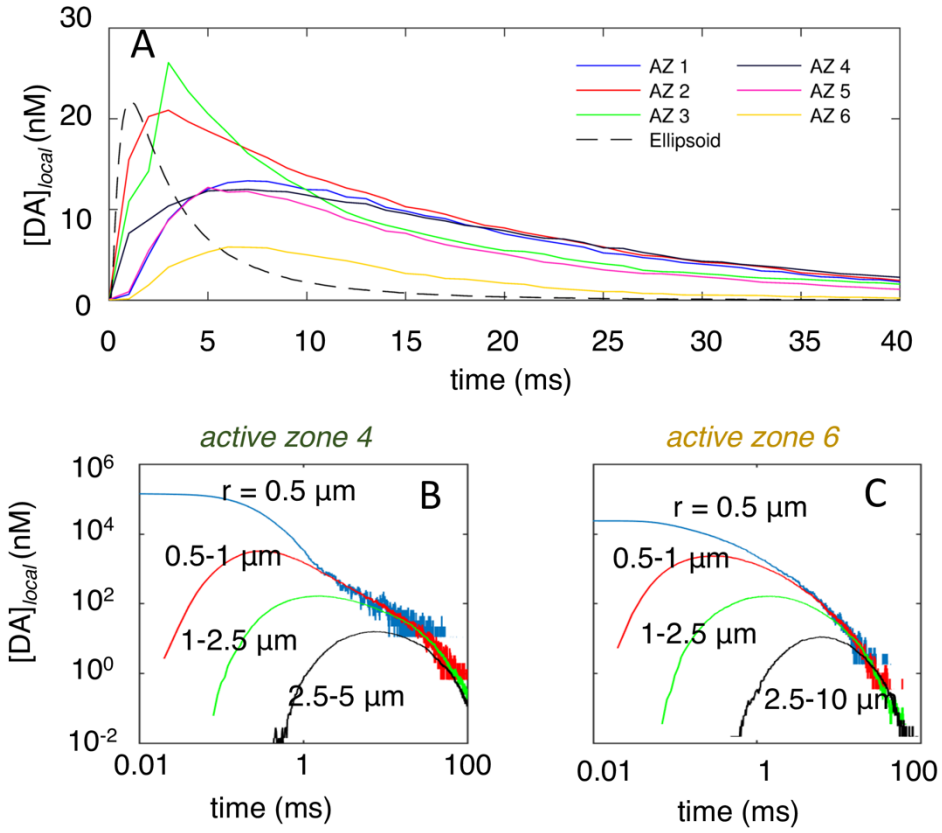

Figure 7. Time evolution of DA levels in the EC region after a single release event in different *AZ*s.

A, Time evolution of EC DA levels within a spherical shell of inner radius r_i 1 µm and outer radius r_o 2.5 µm centered at the *AZ* or top of the ellipsoid for six different *AZ*s and ellipsoid geometry with same volume and surface area (labeled *AZ*1–*AZ*6 and ellipsoid, shown in different colors and patterns; see inset labels). B, C, the local concentration of DA within spherical regions of radius 0.5 µm (blue) and within spherical shells of 0.5-1 µm (red), 1-2.5 µm (green), and 2.5-5 µm (black), near *AZ*4 (B) and *AZ*6 (C), as labeled.

A considerable variation in the maximum level of DA reached and in the succeeding decay rate is observed in Figure 7A, depending on the *AZ* that discharges the DA molecules. For *AZ 2* and AZ *3*, $[DA]_{local}$ can reach 20-25 nM, but for *AZ 6* it remains below 7 nM. *AZ 2* and *3* are on a surface-exposed region of axon terminal 2, near of non-DAT expressing cells (Figure 1C). *AZ 6*, however, lies inside a cavity on axon terminal 4 that harbors a large density of DATs (Figure 1C),

hence the rapid depletion of the released DA. Other *AZ*s (*AZ 1,4* and *5*) show an intermediate behavior because although they are exposed to the EC region, the DAT level in their vicinity is also relatively high (according to fluorescence images).

To examine the effect of neuronal region structural complexity, computations were repeated for a hypothetical EC region with a simplified (ellipsoidal) geometry that preserved the same EC volume and neuronal surface area as those of the simulated system, together with the same number of DAT molecules on the surface, thus maintaining the same DAT surface density as the above system. DA reuptake evaluated for the same spherical shell (Figure 7A, *dashed black curve*) centered around the release site was observed to be faster compared to that occurring in the realistic environment. The faster removal of DA molecules is due to the more efficient diffusion of DA in this hypothetical environment devoid of irregularities/obstacles.

To make a further quantitative assessment of the role of the *AZ* geometry and local structural heterogeneity in affecting the different time evolutions of DA clearance observed in Figure 7A, we examined the tortuosity and void fraction in the vicinity (within 2.5 μm radius) of each of the 6 *AZs*. To evaluate the tortuosity, I randomly selected 5,000 pairs of mesh points and evaluated the ratio of their shortest arc distance along the surface to the corresponding Euclidean distance. The calculations are performed using built-in Blender functions and Neuromorph add-on in Blender (Jorstad et al., 2015). The results are presented in Table 3. Both properties affect $[DA]_{local}$: the clearance of DA is less efficient when the void fraction is low, and the tortuosity is high (e.g., *AZ* 3, followed by *AZ* 2). While void fraction appears to have a dominant effect, tortuosity becomes an important factor when distinguishing the rise time and peak height between *AZs* that exhibit similar void fractions. *AZ* 6 has a high void fraction and a low tortuosity which

leads to rapid reuptake of DA. Another variable we examined is the distance to the closest DAT (Table 3), but it does not have a substantial effect since the diffusion is rapid.

Table 3. Structural properties near *AZ*s

Active Zone	Void Fraction	Tortuosity	Distance to closest DAT (μm)
1	0.35	1.22	0.20
2	0.22	1.38	0.21
3	0.20	1.56	0.24
4	0.31	1.28	0.20
5	0.37	1.36	0.89
6	0.36	1.23	1.22

Overall these results show that (i) the different time evolutions of $[DA]_{local}$ in response to DA release from different *AZs* can be traced back to differences in tortuosity and void fractions, and (ii) the adoption of uniform tortuosity and void fraction for all *AZs* would not provide a realistic representation of the heterogeneous synaptic structure, nor would it account for the differential reuptake efficiency originating from these local geometric effects.

Panels B-C of Figure 7 further illustrate the variations in $[DA]_{local}$ within gradually increasing distance ranges with respect to the release sites in *AZs* 4 and 6. $[DA]_{local}$ within a spherical volume of radius $r = 0.5$ μm remains above 10 μM for about 1 ms after DA release from *AZ 4* and that within $0.5 \leq r < 1.0$ μm rises more slowly and temporarily reaches 1 μM (Figure 7B). Comparison with *AZ* 6 shows the lower $[DA]_{local}$ near the release site ($r < 0.5$ μm) and the depletion

of DA at t ≈ 100 ms (Figure 7C). The large variations in $[DA]_{local}$ due to stochasticity and heterogeneity of the release sites occur during the entire course of the simulations.

The variations in $[DA]_{local}$ are critically important because, while $[DA]_{EC}$ may not be enough for activating DA receptors, $[DA]_{local}$ or the corresponding fluctuations Δ[DA], may bring the local DA concentration above the threshold levels required for activating even low-affinity receptors. These results underscore the significance of considering the space-dependent, stochastic nature of DA density fluctuations for estimating the probability of DA receptor activation in complex microenvironments.

2.3.4 Cellular structural complexity modulates the fractional occupancy of high-affinity DA receptors

Dopaminergic signals are transmitted upon DA receptor activation. There are five different types of DA receptors, commonly classified as D1-like (D1, D5), which have low-affinity for DA (EC_{50} ~1 μM), and D2-like (D2, D3, D4), which have high-affinity (EC_{50} ~10 nM) (Rice & Cragg, 2008). As shown in Figure 7B-C, $[DA]_{local}$ may reach 10-100 μM near an *AZ*, immediately following vesicular discharge, and low-affinity receptors may be activated if they are in proximity. However, DA molecules rapidly diffuse from the release site and the synaptic cleft (of ~ 0.25 to 0.5 μm radius) to extra-synaptic regions, such that synaptic [DA] decreases by ~3 orders of magnitude within tens of milliseconds.

We evaluated the fractional occupancy $f(t)$ of high-affinity DA receptors following a release event for each of the 6 *AZ*s. For the calculation of occupancy, high- and low-affinity receptors were assumed to be uniformly distributed on the membrane of all pre- and postsynaptic

cells similar to previous approaches (Dreyer et al., 2010). Note that the activation of low-affinity receptors requires high $[DA]_{local}$ values, and such high concentration levels are temporarily attained only in the proximity of the release sites. So, in practice, only those low-affinity receptors located sufficiently close to the *AZs* will be activated. As to high-affinity receptors, they are likely to be activated at all locations. To evaluate the fractional occupancy of high affinity DA receptors for each of the 6 *AZ*s, we analyzed 140 x 6 = 840 runs as follows: we divided the simulation box into cubic grids of 1 femtoliter (10^{-15} liters); we counted the number of DA molecules in each cube, to obtain the local concentrations. If the latter was zero at all time-points, the cube was labeled as an excluded volume (inaccessible to DA molecules); otherwise, the probability of satisfying the threshold level (10 nM) for high-affinity receptors was evaluated for each *AZ*, as a function of time elapsed after DA release. The results are presented in Figure 8A. $f(t)$ temporarily reaches a maximum f_{max} before it decays to near zero within ~ 100 ms. f_{max} shows a strong dependence on the release site, varying from 0.27 (*site 6*) to 0.78 (*site 3*), again indicating the importance of the local environment.

To compare simulation results with those predicted by the VT model, we first evaluated the two parameters of the model: the tortuosity of the terminals and the void fraction of cytoplasmic regions accessible to DA diffusion (Dreyer et al., 2010). of the average tortuosity of the surface is 1.79. The void fraction was 0.21, as noted above (Table 1). The results are displayed by the dashed curves in Figure 8A-B.

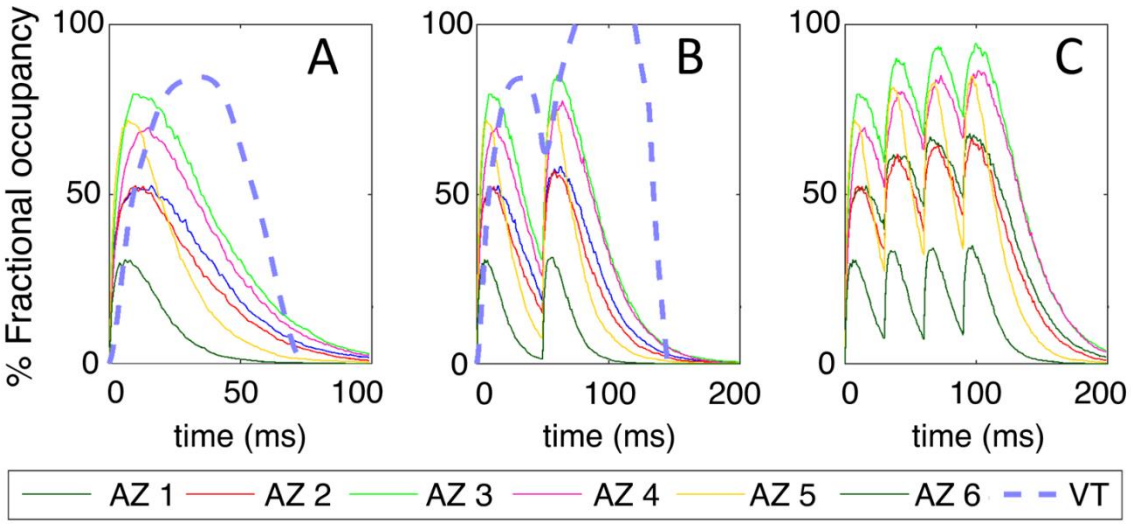

Figure 8. Expected fractional occupancy (or percentage saturation) of DA high-affinity receptors in response to successive releases.

Fractional occupancy as a function of time is based on the probabilistic occurrence of saturation conditions ([DA]local 10 nM) in the synaptic region associated with each *AZ*. Results are shown for different *AZ*s (as labeled) in response to single release (A), two releases with 50-ms interspike interval (B), and four releases with 30-ms interspike intervals (C). Results from the VT model are shown for comparison in A and B.

Figure 8 reveals several differences between the predictions of the VT model and those obtained by *MCell* simulations. The VT model predicts a higher percent saturation (based on 10 nM threshold value), slower binding kinetics (indicated by the longer time to reach the maximal occupancy, and faster decay kinetics, compared to *MCell* predictions. Furthermore, the VT model reaches saturation conditions after two releases with 50 ms spike interval (Figure 8B) - a level not reached in *MCell* simulations even after four spikes with inter-spike interval shortened to 30 ms (Figure 8C). Finally, the VT model cannot capture the variations in $[DA]_{local}$ depending on the *AZ*s (or their specific structure or nearby DAT density).

2.3.5 Phasic firing favors high transient levels in [DA] while retaining the average $[DA]_{EC}$

We investigated the effect of distinctive release patterns, tonic and phasic (Goto, Otani, & Grace, 2007), on DA reuptake efficiency.

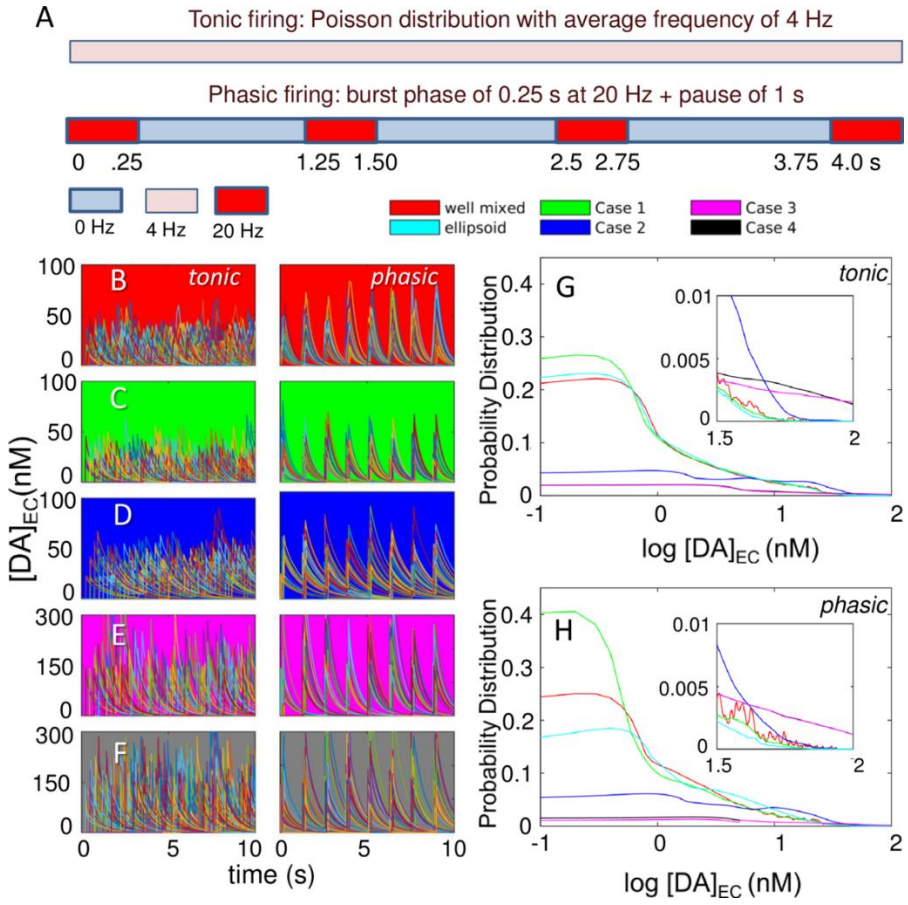

Figure 9. Comparative analysis of global EC DA levels under different firing patterns and the effect of the complexity of cell geometry and the heterogeneity of DAT surface density

A, Schematic description of the firing patterns: tonic (upper bar) and phasic (lower bar). Each color represents a different firing frequency. Tonic firing has a constant vesicular release frequency of 4 Hz throughout the complete duration of the simulations (here shown for 4 s). Phasic firing has burst periods of 0.25 s with a firing frequency of 20 Hz separated by pauses of 1 s. B–F, Time evolution of $[DA]_{EC}$ for five models: well-mixed (background colored red); MCell with uniform distribution of DATs (background in green); MCell with nonuniform distributions of DATs (cases 2– 4 in Fig. 2; background in blue, magenta, and gray, respectively), presented for tonic (left) and phasic (right) firing patterns. Each panel displays the results from 140 individual trajectories from independent runs. G, H, Probability distributions of log $[DA]_{EC}$ level observed in different runs, shown for tonic (G) and phasic (H) firing patterns. The respective insets show the behavior in the range log [DAEC/nM] 1.5. Results for ellipsoid geometry are presented in cyan. The principal semi-axis lengths of the ellipsoid are 8.73, 1.44, and 4.36 µm, which yield the same surface area and volume with the realistic geometry.

The tonic firing was implemented as random spikes generated from a Poisson distribution at 4 Hz frequency (Dreyer et al., 2010); whereas phasic firing consisted of a burst phase for 0.25 s at 20 Hz frequency followed by a pause of 1 s (Figure 9A), both yielding the same average frequency. The time evolution of $[DA]_{EC}$ was examined under those two firing patterns for five different models: a well-mixed system (Figure 9B), and four *spatially realistic* models derived from image data (Cases 1-4 in Figure 2), which differ in the membrane distribution of DATs. The cases are (1) uniform (Figure 9C), (2) non-uniform (Figure 9D), and (3-4) sharply non-uniform with two different localizations of high-density regions (Figure 9E-F) (see Table 2 for corresponding surface densities). Each panel displays 140 curves, each corresponding to an independent run.

Tonic and phasic firing patterns elicit markedly different fluctuations in $[DA]_{EC}$. Tonic firing shows irregular fluctuations (*left* panels in Figure 9B-F), which usually remain below 60 nM in panels B-F; whereas phasic firing in the same cases (*right* panels) easily exceeds 60 nM, especially when the surface density of DATs is non-uniform (panel D). Sharply non-uniform distributions of DATs (panels E-F**)** give rise to increased $[DA]_{EC}$, while the difference in the fluctuation behavior $[DA]_{EC}$ under tonic and phasic firing persists. These results suggest that phasic firing could more readily favor low-affinity DA receptor activation, even though the average $[DA]_{EC}$ values over the entire duration of simulations are comparable (Table 4), consistent with the same average firing frequency shared between the five cases.

Table 4. $[DA]_{EC}$ values (mean ± standard error of the mean) under different conditions

			$[DA]_{EC} \pm \Delta [DA]_{EC}$ (nM)	
Space		DAT distribution	Tonic	Phasic
	Well-mixed DA		8.16±0.92	8.29±1.41
	Ellipsoid geometry		8.21±0.85	8.33±1.44
Case 1	Complex space	Uniform	7.54±0.86	6.93±1.92
Case 2		Nonuniform	16.59±1.26	14.19±2.44
Case 3		Sharp bimodal	33.12±3.13	29.65±4.49
Case 4		Sharp bimodal	32.49±2.86	32.89±3.68

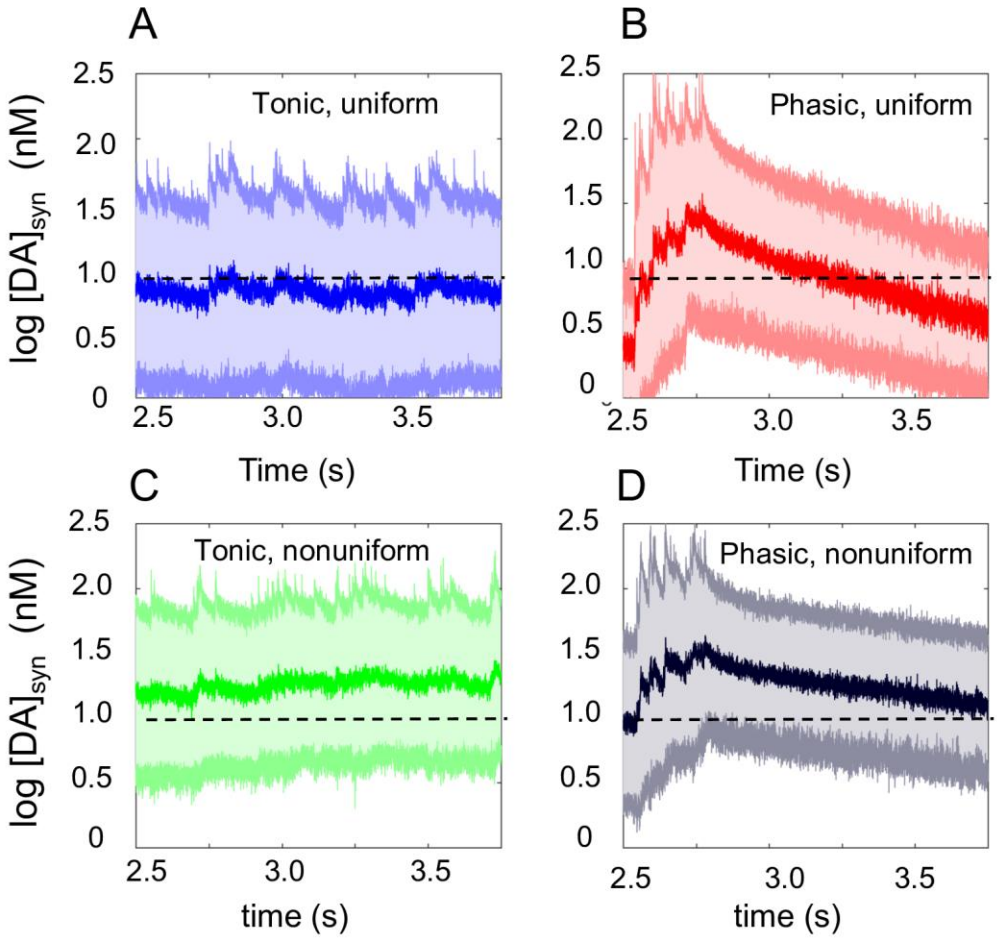

Figure 10. Time evolution of DA level in the synapse after a release event

A–D, $[DA]_{syn}$ as a function of time for tonic (left) and phasic (right) firing, under uniform (top) and nonuniform (bottom) distribution of DATs. The mean and variation in $[DA]_{syn}$ within 1 µm collected from 140 independent runs are displayed. Results are shown for the time interval 2.5–3.75 s as a single firing block, representative of dynamic equilibrium reached under stationary conditions. The thick line in the middle of the cloud is the mean value over all runs, and the cloud represents the standard deviation, highlighting the large fluctuations in the synaptic DA levels.

A closer examination of the transient DA levels within the synaptic region reveals the difference between phasic and tonic firing. We defined $[DA]_{syn}$ as the transient DA level within a

sphere of 0.5 μm radius centered at a release site and examined $[DA]_{syn}$ following a single release event. Figure 10 displays the mean (*central dark curve*) and the standard deviation (*light curves and shade*) in $[DA]_{syn}$ for tonic (A and C) and phasic (B and D) firing, under uniform (Case 1) (A and B) and non-uniform (Case 2) (C and D) distributions of DATs. Similar to the results for the overall EC (synaptic and extra-synaptic) region (Figure 9C-D), phasic firing temporarily leads to a higher accumulation of DA in the synapse compared to tonic, which, can more readily activate the high-affinity DA receptors (the dashed line indicates the threshold concentration, 10 nM, for their activation).

Finally, we computed the fractional occupancy of low-affinity receptors (Casado et al., 2009; Vivo, Lin, & Strange, 2006) during the burst and pause periods of phasic firing, and overall period of tonic firing. The results summarized in Table 5 show that the probability of reaching the threshold DA level of 1 μM for binding low-affinity DA receptors is enhanced by a factor of 2 to 5 in the burst phase of phasic firing, compared to tonic firing. Further computations by adopting a Michaelis-Menten type occupancy model with half-maximal substrate concentration (K_m) of 10 nM for high-affinity receptors and 1 μM for low-affinity receptors confirmed the same behavior. In the latter model, the occupancy of DA receptors as a function of [DA]local is given by $\theta([DA]_{local}) = \frac{[DA]_{local}}{K_m + [DA]_{local}}$, and the results in the last column of the Table 5 are obtained upon integration over snapshots at 1 μs intervals in 140 trajectories.

Table 5. Percentage of high- and low-affinity DA receptors that DAs can potentially bind

System Properties			Percent probability of DA binding to DA receptors	
DAT distribution	DA receptor type	Firing pattern and stage	based on saturation threshold levels	based on Michaelis-Menten kinetics
Uniform (Case 1)	High affinity	Tonic	40.26	45.98
		Phasic Burst	45.09	51.80
		Phasic Pause	4.54	50.07
	Low affinity	Tonic	0.40	2.22
		Phasic Burst	1.10	4.64
		Phasic Pause	0.06	1.92
Nonuniform (Case 2)	High affinity	Tonic	71.14	63.84
		Phasic Burst	65.88	62.70
		Phasic Pause	72.05	64.5
	Low affinity	Tonic	0.35	3.47
		Phasic Burst	1.97	5.47
		Phasic Pause	0.03	2.97

2.3.6 Non-uniform surface distribution of DATs is a major modulator of the strength and intensity of DA signaling

Results in Figure 9 and Table 4 reveal the strong dependence of DA clearance efficiency on DAT surface distribution. DA reuptake is significantly more efficient with a uniform surface distribution of DATs than with a nonuniform distribution, as evidenced by the relative heights of the peaks at low concentrations in the histograms displayed in Figure 9G-H and the average $[DA]_{EC}$ values listed in Table 4**.** We investigated the differences among well-mixed, simple spatial (ellipsoid), and complex realistic geometries while keeping the EC volume, surface area and total density of DAT fixed. Results suggest that the approximation of the axonal morphology by a simplified (ellipsoidal) geometry yields results comparable to those predicted by a well-mixed model. The inclusion of realistic geometry, on the other hand, leads to a broad range of results depending on the specific *AZ* (Figure 7 and Figure 8) and on the surface distribution of DATs (Figure 9G-H). The most efficient clearance is observed in MCell simulations with a uniform distribution of DAT. The bimodal distribution of DATs, on the other hand, shows a distinctive distribution of $[DA]_{EC}$ skewed toward higher concentrations, or a significantly suppressed DA reuptake efficiency, as can be seen more clearly in the insets, irrespective of the firing pattern (Figure 9G-H). This effect becomes more pronounced with increasing heterogeneity of DAT distribution, i.e., going from Case 2 to Cases 3 and 4.

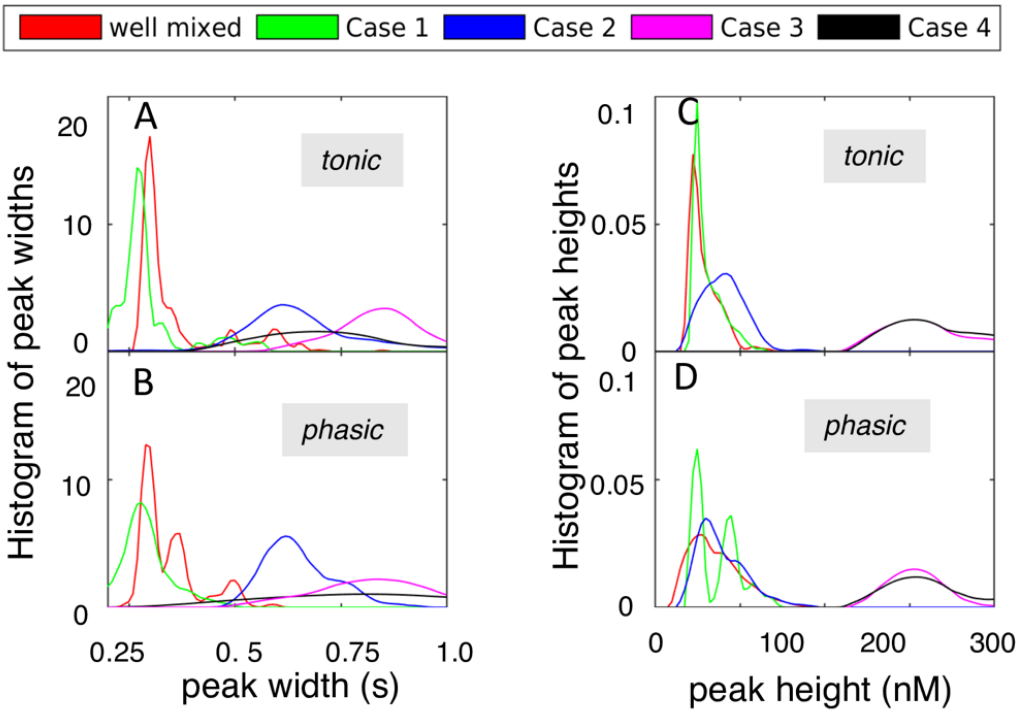

Figure 11. Distribution of peak heights and widths for EC DA levels

Results are presented for four different types of DAT distribution on the plasma membrane, in addition to the well-mixed case. The curves are color-coded, as labeled. The probability distributions of peak widths (A and B) and peak heights (C and D) are presented for tonic (tonic) and phasic (bottom) firing patterns.

We analyzed the peak heights and widths in Figure 9B-F, for a more critical assessment of the duration and intensity of excitatory stimulation induced in response to the two firing patterns, and under different spatial distributions of DATs. The results in Figure 11confirm that DAT spatial distribution is a major determinant of dopaminergic signaling strength and duration, while the effect of different firing patterns is moderate. In particular, the histograms of the peak widths in panels A-B, and peak heights in panels C and D clearly show that bimodal DAT distribution (*black and magenta curves*) leads to more sustained and stronger excitations compared to uniform (or well-mixed) cases (*green* and *blue* curves), originating from less efficient removal of DA. Note

that the bimodal distribution was selected to mimic the physiological density heterogeneities observed in high-resolution images (Figure 1 and Figure 2). The effect of DAT density heterogeneity manifested by an overall suppression in DA reuptake is further accentuated in sharply heterogeneous distributions of DATs (Cases 3 and 4). The most probable peak heights in those cases are of the order of hundreds of nM and may result in neurotoxicity. These results demonstrate that heterogeneity of DAT density can modulate DA signaling.

A comparison between Cases 3 and 4 further shows that the placement of DATs in the close neighborhood of the *AZ*s does not increase clearance. The diffusion of DA is fast enough to sample extra-synaptic regions and the localization of DATs with respect to the *AZ* has a minimal effect. These results suggest that the mechanism of local clearance as envisioned by the gatekeeper model (Rothstein et al., 1994) does not necessarily increase reuptake efficiency.

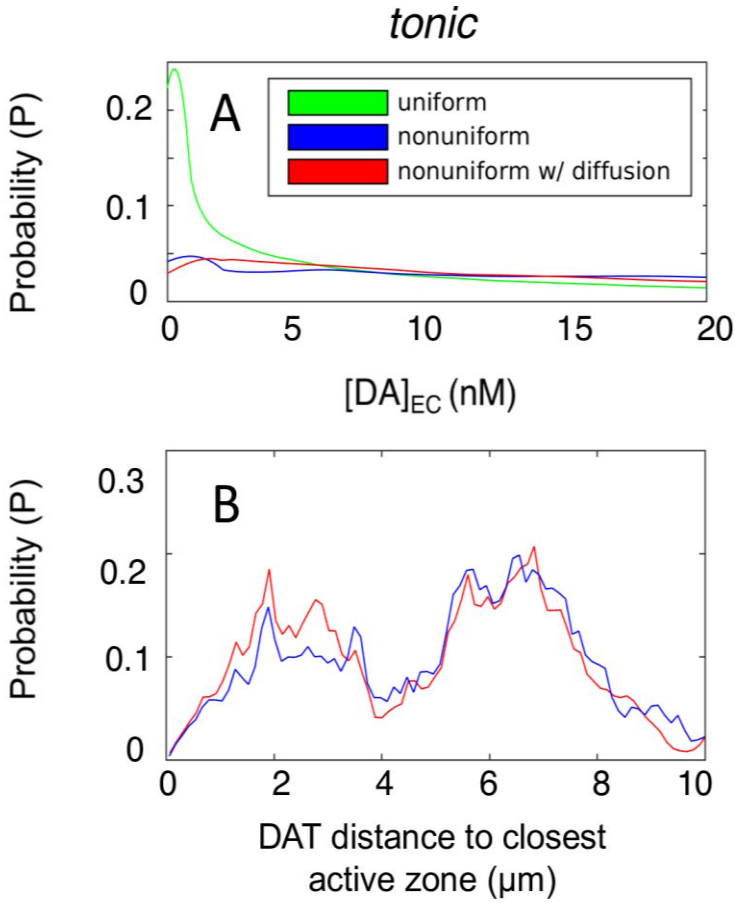

Figure 12. Probability distributions of $[DA]_{EC}$ level under lateral DAT diffusion and Probability distributions of DAT distances to closest *AZ*.

A, Probability distributions of $[DA]_{EC}$ level under lateral DAT diffusion, shown for tonic and $[DA]_{EC}$. Green, blue, and red represent uniform DAT distribution, nonuniform DAT distribution, and nonuniform DAT distribution with the lateral diffusion of DAT, respectively. B, Probability distributions of DAT distances to closest *AZ* from 140 independent simulations for the nonuniform DAT distribution with (red) and without (blue) lateral diffusion.

To examine the change in DA reuptake behavior possibly induced by DAT 2D displacement, we repeated the simulations by allowing DAT 2D diffusion with a coefficient of 3x10-10 cm2/s on the plasma membrane (Figure 12). Comparison of the initial and final (at the end of 10 s simulations) averaged over 140 independent runs showed that no significant change

occurred in the position of DATs, due to the slow diffusion of DATs compared to the timescale of simulations. Overall, these results show that increasing heterogeneity in the surface distribution of DAT leads to lower DA clearance efficiency and/or stronger and more sustained signaling.

2.4 DISCUSSION

2.4.1 Overview

In the present study, I reconstructed *in silico* the 3D structure of DA terminals, the location of *AZ*s and the spatial distribution of DATs based on EM and fluorescence microscopy data with transgenic mice (Block et al., 2015), and conducted a series of MCell simulations under different conditions. I determined the spatiotemporal distribution of DA molecules in the synapse and extra-synaptic regions in response to different firing patterns and in the presence of different surface distributions of DATs. These simulations show the effects of the synaptic and extra-synaptic morphology, as well as the heterogeneity of DAT surface distribution (as observed in experiments) on the overall efficiency of DA clearance and on the probability of activating high- and low-affinity receptors. Heterogeneous distribution of DATs is shown to reduce the clearance efficiency, the effect being sharper with increased heterogeneity, and not affected by DAT 2D diffusion on the plasma membrane. While DA dynamics is diffusion-controlled in general, a global sensitivity analysis indicated that the DA-binding rate of DAT and the relative population of its outward- and inward-facing conformers in the apo state (denoted as OF and IF) had significant effects on DA reuptake efficiency. Overall the results underscore the utility of conducting spatiotemporally realistic simulations in elucidating the dependence of dopaminergic signaling on both the surface distribution and conformational mechanics of DATs.

Recent MCell simulations of glutamatergic signaling based on EM images of hippocampal neuropil for investigation of the effect of spatial heterogeneities (Bartol, Bromer, et al., 2015; Bartol, Keller, et al., 2015; J. P. Kinney et al., 2013) also indicated the importance of including the microenvironment for an accurate description of the electrophysiology and biochemistry of neurotransmission events. No such simulations had been performed for DA neurons to date, mainly due to lack of high-resolution image data of DA terminals for reconstituting *in silico* the simulation environment. Recent advances in imaging DA neurons (Block et al., 2015) permitted us to overcome this barrier. Furthermore, improved understanding of the structural dynamics of DAT (Mary Hongying Cheng & Bahar, 2015; Mary Hongying Cheng et al., 2015; M. H. Cheng et al., 2018; Gur, Cheng, Zomot, & Bahar, 2017) helped us build a simplified kinetic scheme (Figure 3**)** that we adopted in MCell simulations.

2.4.2 DA reuptake simulations require spatially extended models

The simulation of dopaminergic signaling events presents new challenges compared to that of neurotransmission in glutamatergic synapses. The transporter cycle rate in the latter case is around 35 glutamate molecules per second per glutamate transporter, whereas the rate in dopaminergic neurons is 1-5 DA molecules per second per DAT (Povlock & Schenk, 1997; Prasad & Amara, 2001; Rice et al., 2011; Wadiche, Arriza, Amara, & Kavanaugh, 1995). Thus, simulation of DA clearance requires longer computing times. In addition, glutamate transporters are localized in pre- and post-synaptic regions and mostly in the surrounding glia in the close neighborhood of the *AZ* (Danbolt, 2001; Seal & Amara, 1999). DATs, on the other hand, are preferentially located in the extra-synaptic regions of the axons and dendrites and most of the reuptake events take place at distal sites from the *AZ*s (Block et al., 2015; Nirenberg, Vaughan, Uhl, Kuhar, & Pickel, 1996;

Rice et al., 2011). Realistic simulations of such spatially distributed events require the adoption of model systems composed of multiple synapses, multiple *AZ*s, and heterogeneous distributions of multiple DAT clusters. We reconstructed *in silico* a relatively large (10 µm x 10 µm x 7.2 µm) striatal region.

2.4.3 Spatial irregularities and hindrance in the interstitial region between neurons limits DA receptor activation

MCell simulations show that under conditions that reproduce physiological levels of DA and turnover rates (Beuming et al., 2008; Prasad & Amara, 2001; Rao et al., 2013), the complex geometry of DA terminals modulates the occupancy of high-affinity DA receptors to below 100%, even under sustained, elevated stimulation conditions (Figure 8A-C**)**, consistent with the concept of a dead-space (Kamali-Zare & Nicholson, 2013). In contrast, less detailed partial differential equation models (Dreyer et al., 2010) and algebraic models (Cragg & Rice, 2004) predict full occupancy of high-affinity receptors under the same conditions. This difference invites attention to the effect of EC spatial irregularities on dopaminergic signaling efficiency in the brain (Sykova & Nicholson, 2008).

2.4.4 Heterogeneous surface distribution of DAT reduces the effectiveness of DA clearance

EM and fluorescence images showed that the distribution of DAT is heterogeneous in different parts of the striatum (Block et al., 2015). Recent studies indicate that the population of DATs may vary depending on the membrane curvature (Caltagarone, Ma, & Sorkin, 2015) . Notably, selected DAT mutants that have disrupted OF conformations do not accumulate in filopodia, suggesting

that access to the OF/OF* state may be a prerequisite for DAT to populate the filopodia (Caltagarone et al., 2015). Further examination showed that binding of cocaine and its fluorescent analog JHC1-64 also alters the plasma membrane distribution of both wild-type and mutant DATs. Cocaine binding arrests DAT in the OF state, and cocaine-bound DATs predominantly localize in the filopodia (Ma et al., 2017). Likewise, zinc binding, also known to stabilize the OF state, led to an increase in the level of DAT mutants in the filopodia. These observations suggest that the membrane curvature is a determinant of DAT clustering, with the convex shape of the filopodia favoring the localization of DATs. Furthermore, the clustering of OF DATs could remodel the membrane to induce an overall outward bending (Ma et al., 2017). The present study suggests that such targeting of axonal protrusions by OF DATs, along with their membrane remodeling capacities, may regulate DA reuptake.

The total number of DAT molecules was sufficiently abundant in current simulations (around 200,000) to ensure standard DA clearance consistent with physiological levels. However, simulations repeated with the same number of DATs distributed non-uniformly on the neuronal membranes showed a reduction in reuptake capacity that became more pronounced with increasing surface density heterogeneity. The surface distribution of DATs indeed emerged as a major determinant of the efficiency of reuptake, or conversely, the strength and duration of excitatory signaling (Figure 9 and Figure 11).

In principle, one might expect that the increased population of DATs in dense regions would counterbalance the effect of lower surface area coverage on DA reuptake efficiency. However, DA diffuses fast enough to escape from these dense regions after a few encounters resulting in reduced DA reuptake. These observations further support the importance of adopting

a realistic representation of the heterogeneity of DAT surface distribution, especially with low copy numbers of neurotransmitters, for a realistic assessment of DA reuptake capacity.

2.4.5 Firing patterns determine the relative levels of inhibitory vs. excitatory responses

Simulations revealed that the average $[DA]_{EC}$ exhibited little dependence on firing pattern, provided that the average firing frequency was maintained, but the local levels within a synapse, or close to DA release sites exhibited strong dependencies. The size of the fluctuations Δ[DA] in DA levels was relatively small in tonic firing, but large in phasic firing, especially at the burst phase and under sustained phasic firing (Figure 9B-F). Low-affinity DA receptors need two orders of magnitude larger DA concentrations than high-affinity receptors to get activated. As a result, the activation of low-affinity receptors is limited, if not unlikely, with tonic firing (Table 5). Phasic firing, on the contrary, induces a more considerable variance both in global and local DA concentrations and is 2 to 5 times more likely to activate low-affinity receptors during the burst phase of DA signaling (Table 5). Previous work showed that the D1 receptors are mostly localized at the post-synaptic membrane (Cadet, Jayanthi, McCoy, Beauvais, & Cai, 2010); and MCell simulations show that only those low-affinity receptors localized near the synapse can be activated. In the case of high-affinity receptors, on the other hand, proximity to release site is not a requirement for being activated; high-affinity receptors located on distal regions may be equally activated.

DA receptors regulate the activity of DA neurons. One distinction between high- and low-affinity DA receptors is the type of response they elicit in the cell, inhibitory or excitatory (Keeler, Pretsell, & Robbins, 2014), following their activation upon DA binding. D1-like receptors, which

are usually low-affinity receptors, are involved in excitatory signaling; whereas D2-like receptors trigger inhibitory signaling processes. High-affinity receptors may be activated by both phasic and tonic firing. However, simulations suggest that low-affinity receptors would be instead activated upon phasic firing.

Among D2-like receptors, D2 autoreceptors are known to be critical regulators of DA transmission, located on most axon terminals (Ford, 2014). While D2-like receptors are usually high-affinity receptors, D2 autoreceptors exist in both high- and low-affinity states, and recent studies indicate that the functionally relevant D2-autoreceptors are predominantly in the low-affinity state. Their inhibitory action is particularly necessary for suppressing DA release from the presynaptic cell under a prolonged burst of action potentials. They suppress DA release in the striatum by several mechanisms, e.g., by inhibiting the voltage-gated calcium channels that trigger exocytotic DA release or increasing DAT activity or surface expression (Ford, 2014). Previous studies suggested that tonic firing does not raise $[DA]_{EC}$ to levels sufficiently high to activate those receptors activate D2-autoreceptor mediated DAT regulations (Beckstead, Ford, Phillips, & Williams, 2007; Ford, 2014). The low probability of binding low-affinity receptors under tonic firing demonstrated in the present simulations is consistent with the functioning of D2-autoreceptors as low-affinity receptors.

A previous model modified the probability of DA release upon an action potential according to high-affinity receptor occupancy (Dreyer & Hounsgaard, 2013). In the current model, receptor occupancy has not been coupled with DA release and reuptake. However, the suggested modeling framework allows for implementing a mechanistic model that incorporates the mediation of DA release and DAT expression by D2-autoreceptors. Such an extension may be crucial to improving interpretation of DA reuptake dynamics at longer time scales and under disease states.

2.4.6 The modeling framework is extensible to analyzing the effect of psychostimulants on DA reuptake dynamics

DAT kinetics is often described by the alternating access model (Vaughan & Foster, 2013). Most cell-level models of DA transport at the cellular level assume an immediate transition from IF to OF state right after DA release to the cell interior (Cragg & Rice, 2004; Rice & Cragg, 2008; Sulzer et al., 2016) and the transition from OF to IF in the unbound form is not explicitly considered. In contrast, molecular simulations revealed a complex dynamics (Mary Hongying Cheng & Bahar, 2015), which we reduced to a 4-state kinetic model (OF, IF, OF* and IF*). The translocation and release events after substrate binding are much faster compared to the return of apo IF state to OF state and succeeding substrate binding event which depends on prior probabilities of encounters between DAT and DA molecules. These features result in short lifetimes for the bound forms of DAT and the dominance of the relative populations of the unbound OF and IF states in determining the overall clearance rate (Figure 4). The balance between the OF and IF states, or the ratio of the associated rate constants, k_{14}/k_{41}, using detailed balance principle) emerged as a major determinant of reuptake efficiency, as it directly defines the fraction of reuptake-ready (OF) DATs.

Previous X-ray crystallographic studies (Penmatsa et al., 2015; Wang et al., 2015) as well as structure-based simulations (Mary Hongying Cheng et al., 2015) have shown how the conformational state of DAT and substrate binding affinity may change in the presence of different antidepressant and psychostimulants drugs, such as cocaine and amphetamine (AMPH). Antidepressants usually arrest DAT in OF state (and the same effect has been observed for the homolog serotonin transporter in the presence of antidepressants (S)-citalopram or paroxetine

(Coleman, Green, & Gouaux, 2016)), thus preventing the progress of the transport cycle, and causing an increase in EC DA levels. On the other hand, the occupancy of the Zn^{++}-binding site (Stockner et al., 2013) (by zinc or other transition metals) reduces the DA binding affinity of DAT (Li et al., 2017). The current modeling framework can readily be extended to incorporate such effects through a suitable readjustment of kinetic parameters in Figure 3.

AMPH, on the other hand, appears to be a substrate for DAT that competes with DA for transport (Zhu & Reith, 2008). AMPH is also known to promote both DA efflux (reverse transport from the cell interior to the EC region) and DAT internalization (Wheeler et al., 2015). The current simulations focused on the influx of DA from the EC region to the presynaptic cell interior, but the modeling framework is readily extensible to simulating DA efflux as well. Other extensions of the present framework could incorporate the effects of DAT internalization, membrane polarization (Richardson et al., 2016), or perturbations at the membrane-proximal N-terminal residues (Sorkina, Richards, Rao, Zahniser, & Sorkin, 2009). Thus, the present study opens the way to quantitative modeling of the effects of antidepressants, psychostimulants, and substances of abuse on the deregulation of DA signaling.

3.0 EFFECT OF PSYCHOSTIMULANTS ON DOPAMINERGIC SIGNALING

3.1 BACKGROUND

Drug abuse is one of the major threats to public health worldwide, and approximately 7% of the population are drug users (Council, 1993). Drugs such as opiates and nicotine cause addiction. A few therapy options exist for such conditions. Yet, many of them are ineffective, and the effective ones have significant failure rate due to side effects including life-threatening conditions (McLellan, Lewis, O'Brien, & Kleber, 2000). Therefore, there is a need to identify how the function of the central nervous system (CNS) is altered under drug abuse conditions and to design therapeutics against addictions. Drug addiction is a complex process that is mainly viewed as a neurobiological impairment with various influencing factors (Kozel & Adams, 1986). Many drugs disturb the activity levels of neurons in the CNS with an initial effect on transporters or receptors followed by a more substantial downstream effect on the regulatory pathways (Cosgrove, 2010). As a result, there are multiple components that contribute to drug addiction on different levels of the CNS. Such a complex problem with multiple lengths and timescales requires multiscale models to understand the interactions between proteins and drugs.

Dopamine (DA) is one of the critical components of many drug abuse problems due to its importance in motor control, cognition and reward pathways (Wise & Rompre, 1989). Deficient DA signaling is thought to underlie critical pathological features of a variety of brain disorders

including drug addiction (Money & Stanwood, 2013). DA neurons are functionally heterogeneous and morphologically complex (Block et al., 2015). Proper DAT distribution in the DA neuron is critical for understanding the functional difference of the dopaminergic system between its normal and disturbed states (Ma et al., 2017). The DA transporter (DAT) is responsible for the clearance of the extracellular (EC) DA, which terminates the DA receptor activation and regulates DA neurotransmission. DAT is the primary target of the psychostimulant cocaine (Bai et al., 2014). Cocaine competitively binds to DAT and blocks its activity (Beuming et al., 2008). As a result, the EC DA concentration remains higher, and the activity levels of DA receptors increase significantly. The effects of cocaine on the CNS have been investigated by both experimental and computational studies, but computational studies have not included the spatial complexity and DAT distribution, and the effect of the spatial complexity is not investigated in experimental studies.

Another psychostimulant that targets DAT is amphetamine (AMPH) which induces the non-vesicular release of DA from DAT via modifications in downstream signaling (Wheeler et al., 2015). AMPH enters the cell through DAT in a similar mechanism to DA and disrupts the downstream events such as the interaction between Rho and GTP. Consequently, AMPH induces DA efflux through DAT (Wheeler et al., 2015).

With recent advances in imaging technologies and high-performance computing, it is possible to explore the molecular basis of the deficiencies in neurotransmission underlying drug abuse and drug addiction. The changes in regulating molecules in the presence of psychostimulants such as cocaine and AMPH helped us to identify the major players in a complex downstream signaling pathway (Wheeler et al., 2015). As described in the previous chapter, quantitative characterization of the spatiotemporal distribution of DATs in the striatum enabled us to carry out

a spatiotemporally realistic simulation of DA reuptake. The effects of drugs under realistic spatial conditions are not well-established and coupling spatial complexity and the intracellular protein-protein interactions using network models provide new insights on the alteration of DA signaling.

Here, my coworkers and I developed and implemented computational approaches at both spatiotemporal and subcellular levels of DA signaling in the presence of psychostimulants. I used biological modeling tools to determine the effects of exposure to AMPH and cocaine on cell signaling and regulation. For cocaine exposure, I studied the effect of different concentration of cocaine levels on the DA neurotransmission. For AMPH, I connected the cellular interaction network model created by Dr. Bing Liu with the spatially realistic model of DA reuptake described in Chapter 2 and used the integrated model to model the effect of varying AMPH levels on extracellular DA levels. Results suggest that the effect of the cocaine is more drastic under higher cocaine concentrations. The spatial complexity and heterogeneous distribution of DAT attenuate the rate of AMPH influx and the effect on the intracellular signaling becomes minor at low AMPH concentrations. However, if a uniform distribution of DAT is assumed, the effects of AMPH become more pronounced due to an increase in the AMPH intake rate.

3.2 METHOD

3.2.1 Spatially realistic model of DA release and reuptake in the presence of psychostimulant cocaine

For the spatiotemporal dynamics of DA release and reuptake, we used the model that is described in Chapter 2.0In addition to the kinetics of DA binding/unbinding to DAT; I included an additional reaction with cocaine molecules. Cocaine molecules have diffusion properties similar to DA (K.

M. Kahlig & Galli, 2003). In terms of interaction with DAT, cocaine has a significantly higher binding affinity compared to DA (Gether, Andersen, Larsson, & Schousboe, 2006). The half-life of the cocaine is of the order of hours (Jufer, Wstadik, Walsh, Levine, & Cone, 2000), which is considerably higher than our simulation duration (10 s). The forward binding rate of cocaine to DAT is assumed to be 10-fold higher than DA-binding which approximates the cocaine binding as an irreversible reaction. The resulting kinetic scheme is given in Figure 13. The DAT states are in black, and the transitions are colored as green. The parameters of the system are given in Table 2. The only additional parameter is the cocaine binding rate to OF DAT which is $9.60 \times 10^{7}\ M^{-1}\ s^{-1}$ (Chapter 2.0).

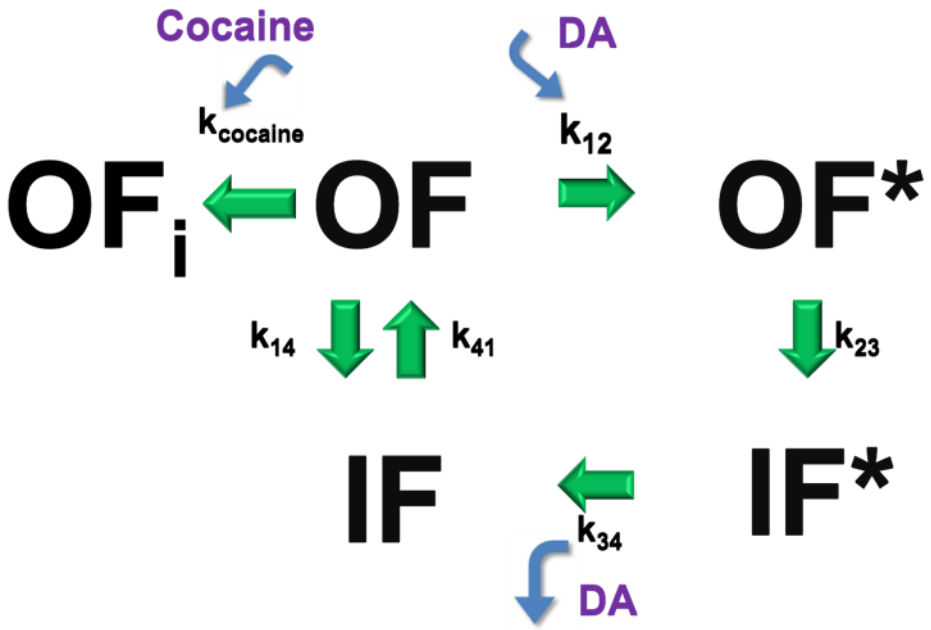

Figure 13. Kinetic scheme of cocaine and DA binding to DAT

The model created in Chapter 2.0is used as a basis. Different DAT states are colored as black, and the transitions are colored as green. The additional neurotransmitters/psychostimulants are shown in purple. In addition to four states described, cocaine bound DAT state OF_i is defined. The cocaine binding rate constant is $k_{cocaine}$. In this scheme, OF DAT can undergo three reactions instead of two and the equilibrium distribution of DAT states are changed with respect to cocaine concentrations.

3.2.2 Network model of intracellular dopamine dynamics

Dr. Bing Liu created a detailed mathematical model of the signaling network that governs AMPH-induced DA efflux and DAT trafficking. A detailed network diagram is in Figure 14.In the model, the effect of AMPH in intracellular signaling is initiated with the internalization of AMPH from DAT. Intracellular AMPH interacts with the trace amine associated receptor (TAAR1) and activates a common signaling complex composed of a transcription termination protein, Rho, and guanosine diphosphate (GDP). The Rho-GTP complex is assumed to be a central regulator of DAT

internalization (Freyberg et al., 2016; Wheeler et al., 2015). Also, TAAR1 activates subunit interactions of a family of guanine nucleotide binding proteins (G-proteins) that acts as molecular switches in the cell (Smrcka, 2008)and leads to the release of ɣ subunit. ɣ subunit of the G-protein activates protein kinase A (PKA); PKA interacts with Rho-GTP complex. Because of PKA activity, Rho is released from the complex in phosphorylated form. Phosphorylated Rho induces Ca^{2+} pathways and activates calcium-calmodulin-dependent kinase type II (CaMKII), which in turn phosphorylates DAT. Phosphorylated DAT exhibits an increase in the transport of intracellular DA to extracellular space (DA efflux). Phosphorylated DAT also tends to be internalized. Both effects may lead to excess DA accumulation in the synapse. In addition to direct interactions of AMPH, the ɣ subunit of the G-protein induces the release of Ca^{2+} from the endoplasmic reticulum (ER) via phospholipase C (PLC) and the inositol 1,4,5-triphoshate receptor (IP3R) resulting in an increase in the level of intracellular Ca^{2+}. Another AMPH interaction included in the model is its translocation via vesicular monoamine transporters (VMATs) into vesicles, which promotes the release of DA from the vesicles due to pH gradient, which, in turn, increases the amount of intracellular DA.

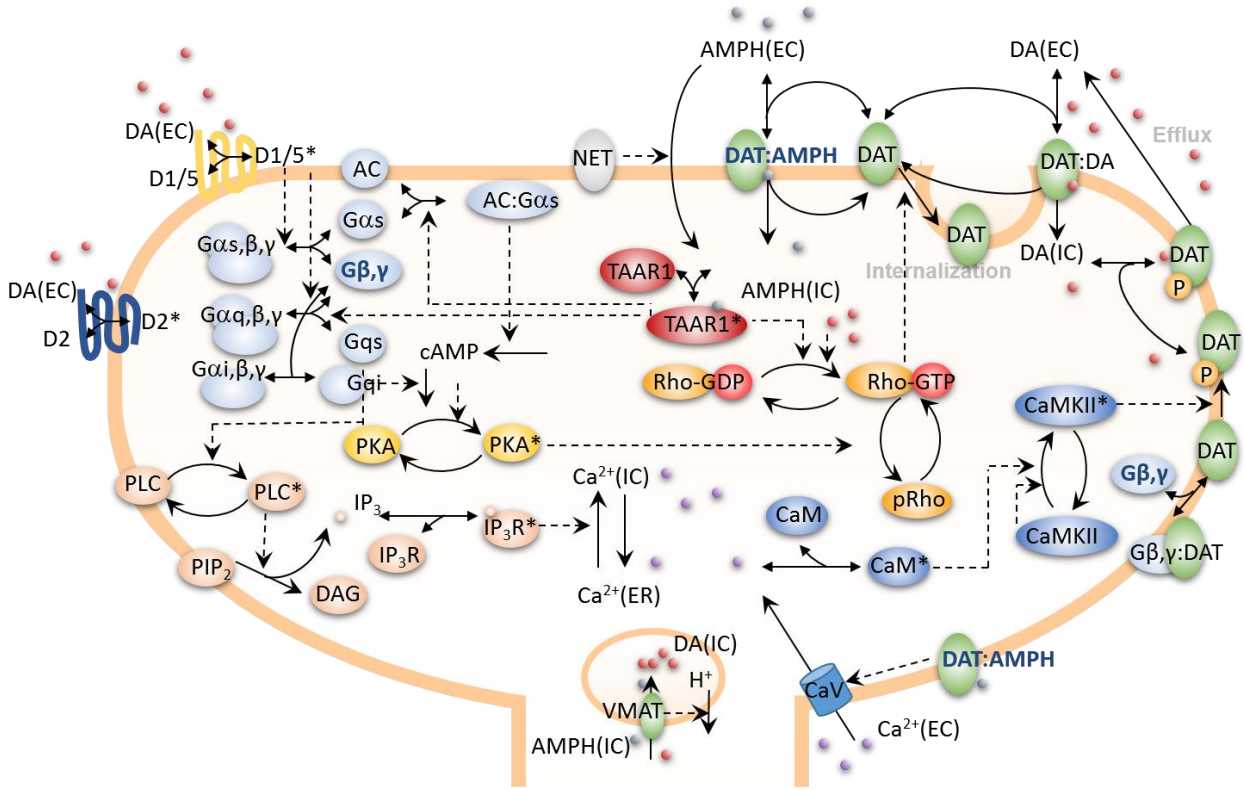

Figure 14. A detailed description of the AMPH-induced intracellular signaling model

The AMPH induced DA efflux pathway is shown. The pathway has several compartments. The first compartment is the part the DAT (green circle) uptakes DA (red dot) and AMPH (blue dot) into the cell. The second compartment is responsible for TAAR1 (maroon) activation by AMPH and phosphorylation of Rho-GDP complex. Rho is shown as an orange ellipse, and GDP/GTP is shown as a red circle. TAAR1 activates the third compartment which is composed of various G-protein subunits, DA receptors, PKA and adenylate cyclase (AC). The G-proteins and AC are shown as light blue. The DA receptors located on the membrane and shown as curved lines. D1 type of receptors are given in yellow and D2 type receptors are given in dark blue. PKA is shown as yellow ellipses. The G-proteins activate the next compartment which is composed of PLC, IP3R, and phosphatidylinositol 4-5 biphosphaste (PIP2). The proteins in this compartment are shown as pink ellipses. The last compartment is the compartment of Ca^{++} signaling. Calmodulin (CaM) and CaMKII are two major parts of this compartment, and they are shown as dark blue ellipses. The additional items are voltage-gated calcium channels (CaV) and the vesicular monoamine transporters (VMAT). VMAT is like DAT shown as green ellipses, and CaV's are dark blue cylinders on the membrane.

The model of AMPH-induced DA efflux and DAT trafficking consists of 49 ordinary differential equations and 66 kinetic parameters. Dr. Bing Liu performed the parameter estimation using the experimental data in the literature (Freyberg et al., 2016; Palaniappan, Gyori, Liu, Hsu, & Thiagarajan, 2013; Wheeler et al., 2015) with statistical model checking (Liu & Faeder, 2016).

3.3 RESULTS

3.3.1 Cocaine competitively inhibits DAT and exponentially increases DA receptor activity

The model developed in Chapter 2.0 is simulated in the presence of two different cocaine concentrations for 10 seconds. The first selected concentration is the cocaine concentration that reduces the visible activity of DAT by half, IC50, which is 380 nM (Reith, Berfield, Wang, Ferrer, & Javitch, 2001) . In addition to IC50 value, we also simulated the system with half of the IC50 level of cocaine to investigate the effect of low cocaine on the EC DA concentration.

Results show that there is a reduction in the activity of DAT, or accumulation of DA in the EC region, due to competitive inhibition from the cocaine molecules. At IC50 concentration, the EC DA concentration values close to zero are reduced regardless of the distribution of DAT, and the values at higher concentration levels are increased if the DAT distribution is nonuniform (Figure 15). However, the half of the IC50 level of cocaine's effect on the EC DA is not as drastic as the IC50 level. The difference between the DA levels in simulations with no cocaine and the simulations with half IC50 cocaine level is slight at the large EC DA concentrations. The main reason is due to the large number of DAT (< 220,000) on the surface in our simulation environment of 720 fl, and 75% of the DAT molecules are in the inward-facing state (Chapter 2), which does not bind cocaine. When the majority of outward-facing DAT molecules are blocked by cocaine,

inward-facing DAT molecules start to transition into an outward-facing state. Accordingly, the reuptake efficiency is only slightly downregulated at low cocaine concentrations. If the cocaine concentration is high enough to reduce the amount of OF DAT significantly such as IC50 level, the effect of cocaine becomes more pronounced. Since the DA receptor activity is directly related with the EC DA concentration, it is possible to assume that high cocaine concentrations increase the DA receptor activity by reducing DA reuptake efficiency.

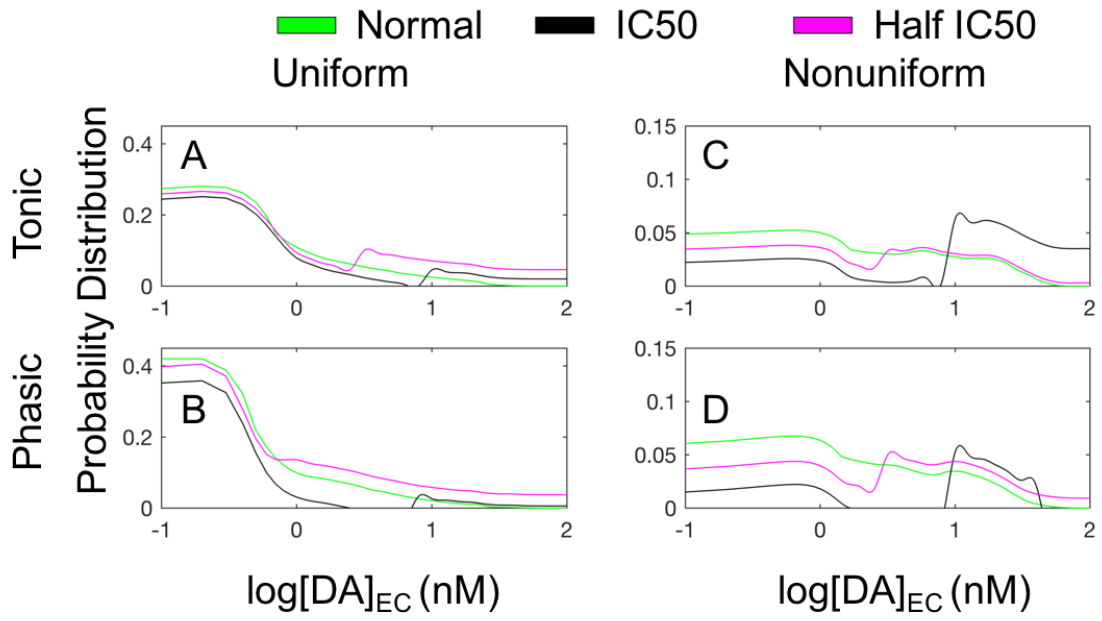

Figure 15. Comparative analysis of EC DA concentration under different cocaine concentrations

The probability distribution of the logarithm of the EC DA concentration is obtained from multiple runs shown for tonic (A, C) and phasic (B, D) firing patterns and uniform (A, B) and nonuniform (C, D) DAT distributions. The distribution of the EC DA concentration is shown between 0.1 to 100 nM. The cocaine concentration is denoted as three different colors. The simulation with no cocaine (green), half of the IC50 level (magenta) and IC50 level (black) are performed.

3.3.2 Hybrid spatial-network model of AMPH-induced DA efflux

The efflux model is constructed using DA reuptake model as a basis. All model equations and parameters are used as described in Chapter 2. The primary driver of the DA efflux is the AMPH uptake to the cell. AMPH and DA are similar molecules. Therefore, AMPH diffusion and reaction constants for interactions with DAT are assumed to be the same as those of DA. In the DA reuptake model, the intracellular DA concentration was not tracked, and it was assumed that each re-uptaken DA molecule was degraded for simplicity. However, a DA efflux is triggered by the interactions of AMPH with intracellular signaling molecules. Thus, we need to track AMPH in the cell. AMPH has two significant effects in the cell, both resulting in the accumulation of DA in the synapse. First, AMPH induces the phosphorylation of outward facing DAT via CaMKII signaling cascade, which promotes DA efflux (Figure 14). Second, AMPH triggers the Rho pathway and initiates Rho-dependent DAT internalization.

To estimate how intracellular AMPH induces DAT phosphorylation, I used data generated from the network model of AMPH-induced DA efflux by Dr. Bing Liu. To introduce diffusion limitations to the model, I considered the relation between the rate of DAT phosphorylation and intracellular AMPH concentration. According to the intracellular network model, the forward rate constant for DAT phosphorylation is 0.184 s^{-1} without the direct influence of AMPH concentration. The rate of DAT phosphorylation is evaluated at steady state conditions under different AMPH concentrations. The relationship between intracellular AMPH concentration and DAT phosphorylation rate is modeled (Figure 16A). From the fit of the intracellular AMPH concentration to DAT phosphorylation rate, the following relation is obtained for DAT rate constant based on intracellular AMPH concentration. Instead of checking the AMPH concentration

at every time step, the rate parameter is updated in every half second intervals based on current intracellular AMPH concentrations since it is not possible to identify concentration-dependent kinetic rates in MCell.

Equation 6

$$k_{DATp} = \frac{-1.26 \cdot 10^{-7} \cdot \log([AMPH_i]) - 9.5 \cdot 10^{-8}}{[AMPH_i]}$$

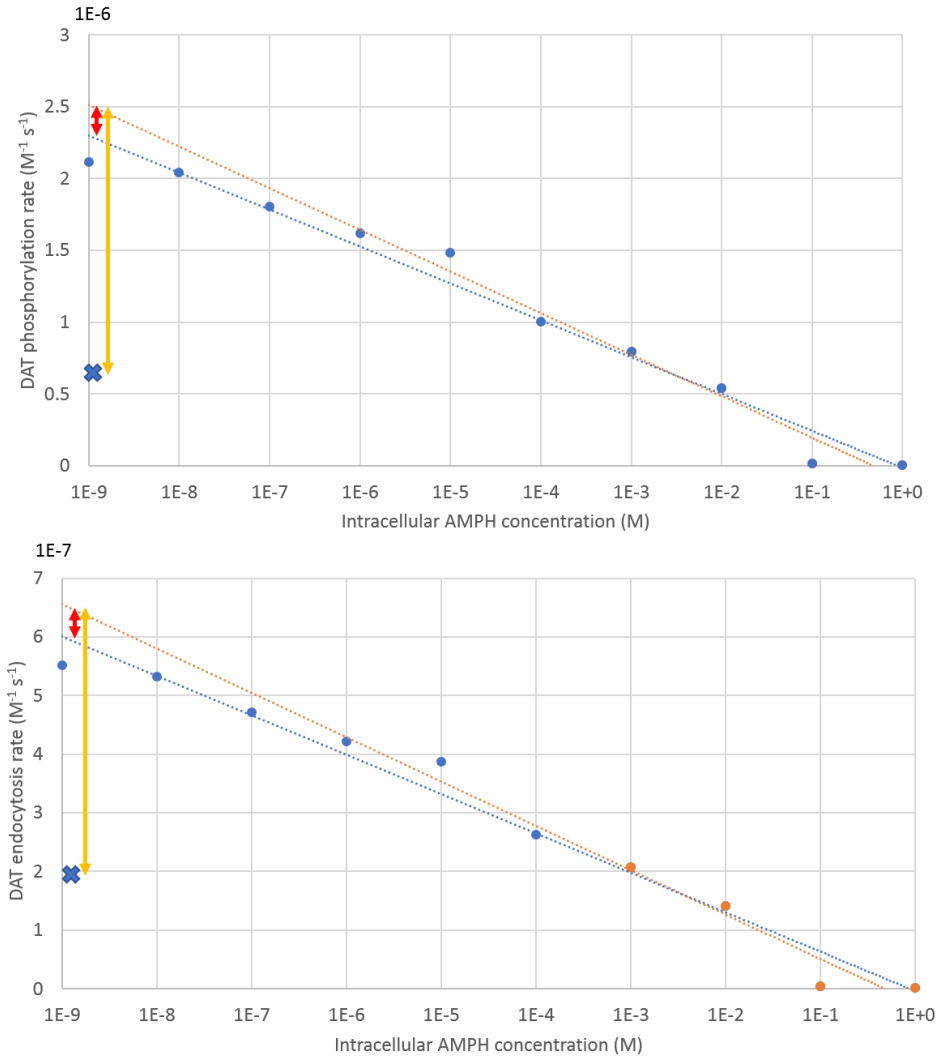

Figure 16. Correlation between intracellular AMPH concentration, DAT phosphorylation rate, and DAT endocytosis

The relations of steady-state intracellular AMPH concentration with the DAT phosphorylation rate (A) and DAT endocytosis rate (B) are given. The blue dots show the calculated reaction rates at the steady state generated from the intracellular network varying EC AMPH concentration from 1 nM to 100 µM, and orange dots show the same rate between 1 mM to 1M. The fits are shown with dashed blue and orange lines. The difference between simulations with no diffusion component has a minor difference at low concentrations. However, the rates differ significantly due to the presence of diffusion. The expected reaction rates are shown as blue "X" and the difference is shown with a yellow arrow. Notably, at low AMPH concentrations, the effect of diffusion is more pronounced.

A similar strategy is used to understand how AMPH induced the endocytosis of the DAT. To avoid the limitations that are due to the diffusion of the AMPH in the cell, only large concentration values are used for estimation. Based on the steady-state values of outward facing DAT and the rate constants provided from the network model, the relation between intracellular AMPH concentration and the rate constant of rho-dependent endocytosis rate is determined. The following equation shows how intracellular AMPH regulates the DAT endocytosis rate.

Equation 7

$$k_{DAT\_ENDO} = \frac{-3.28 \cdot 10^{-8} \cdot \log([AMPH_i]) - 2.48 \cdot 10^{-8}}{[AMPH_i]}$$

Similar to DAT phosphorylation rate constant, DAT endocytosis rate constant is also updated every half second. According to the results from the simulation of the network model at both high and low AMPH concentrations, the intracellular AMPH concentration reaches the equilibrium level after a second (Figure 17). Therefore, choosing an average length for time intervals is an excellent strategy to avoid issues arising from AMPH concentration spikes. A schematic description of the spatial AMPH induced DA efflux model is given in Figure 18.

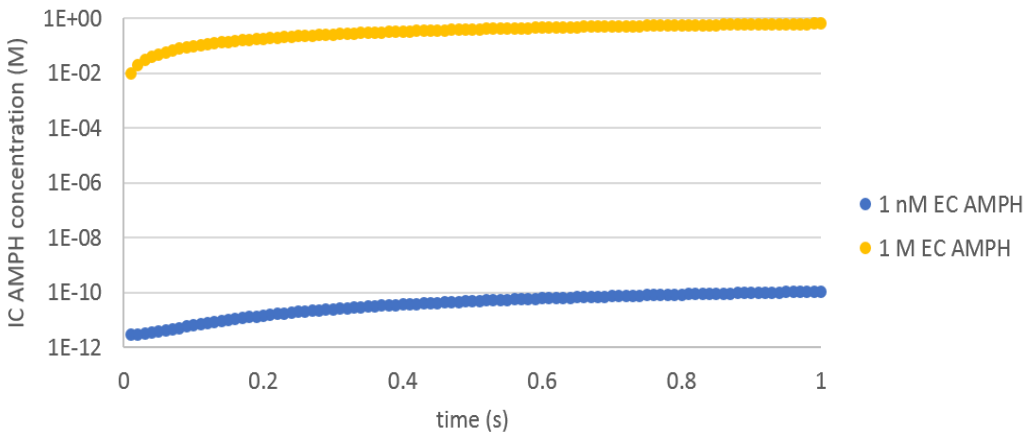

Figure 17. Intracellular AMPH dynamics in the intracellular network model

The change in the intracellular AMPH concentration calculated from the nonspatial network model. The blue dots show the intracellular AMPH concentration for 1 nM EC AMPH concentration and orange dots shows the IC AMPH concentration for 1 M EC AMPH concentration. The results show that both simulations converge around 1 second.

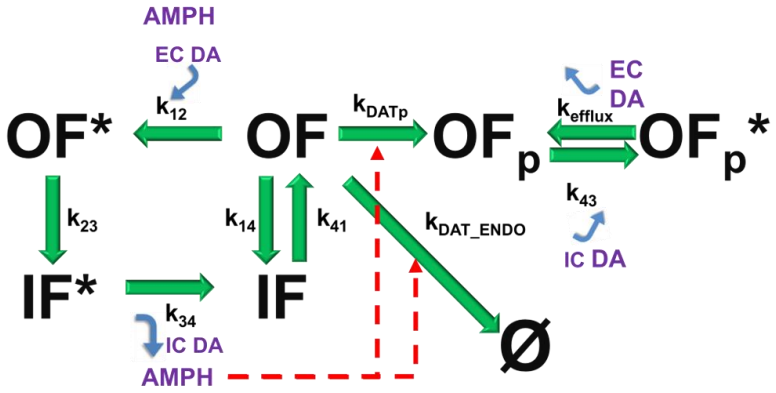

Figure 18. Spatial model AMPH-induced DA efflux

The simplified spatial AMPH-induced DA efflux model is shown. In addition to states that are used in Chapter 2.0three new states are introduced. A phosphorylated DAT state (OF_p), phosphorylated and DA bound DAT state (OF_p*) and the state of DAT after endocytosis (Ø) Direct interactions are shown with green arrows and the induced relations are shown with red dashed arrow. Three new rates parameters (k_{efflux} , $k_{DAT\_ENDO,}$ and $k_{ICDA\_binding}$) are introduced.

In Figure 18, the green arrows show the interactions used from the DA reuptake model in Chapter 2.0The new additions are the following: (i) AMPH uptake from outward-facing DAT (OF), (ii) DAT phosphorylation regulated by AMPH (OF → OF_p), (iii) DAT endocytosis regulated by AMPH (OF → Ø), (iv) IC DA recruitment to phosphorylated DAT (OF_p → OF_p*) and (v) DA efflux (OF_{p*} to OF_p). The primary assumption of this model is the following. The phosphorylated DAT is assumed to be in the outward-facing state, and IC DA can bind to outward-facing state. In reality, DA binds to phosphorylated and inward-facing DAT, and DA is released afterward. For simplicity, this two-step process is reduced into a single reaction. In addition, the endocytosis event is only assumed to be occurring at OF state for increased efficiency in computation. This event can take place in all the states of DAT. This model is simulated under varying DAT distributions (uniform and non-uniform), action potential firing patterns (tonic and phasic), and AMPH concentrations (1 nM and 10 nM).

3.3.3 DAT distribution affects the activation of DA efflux from DAT

I performed simulations under two different extracellular AMPH concentrations using the model described. Under uniform DAT distribution, EC DA concentration is considerably higher compared to that observed in the absence of AMPH (Figure 19A,B) The AMPH uptake efficiency is considerably higher than that in the simulations with non-uniform DAT distribution. As a result of high intracellular AMPH concentration, DAT endocytosis and DAT phosphorylation are triggered. Both of these events increase the EC DA concentration by reducing the DA reuptake and triggering DA efflux, respectively. On the contrary, the effect of nonuniformity of DAT distribution on the EC DA concentration is weak (Figure 19C and D). At low AMPH levels and nonuniform distribution of DAT, the amount of intracellular AMPH is considerably small due to

the reduced efficiency of AMPH uptake. As a result, DAT endocytosis and DAT phosphorylation events are not triggered.

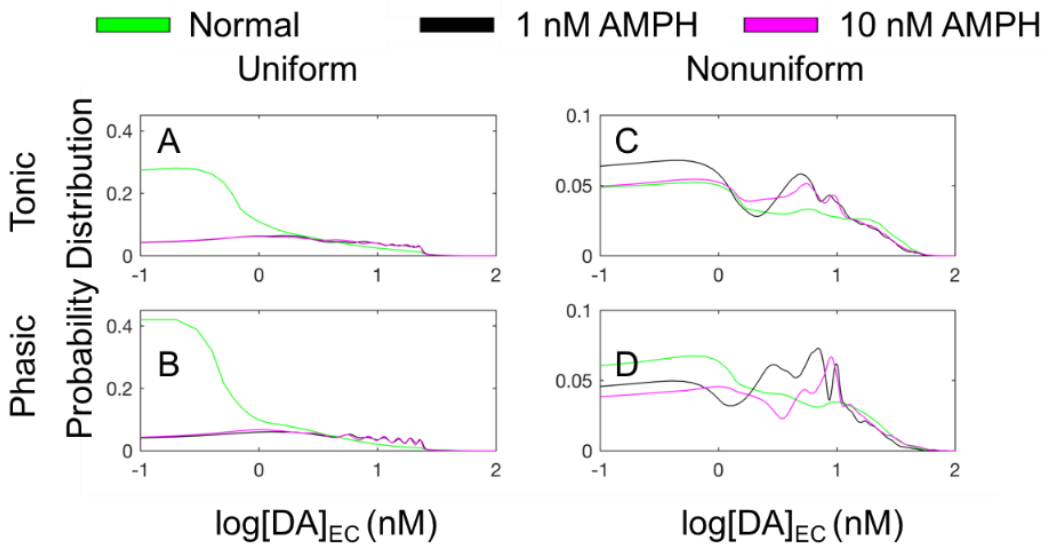

Figure 19. Comparative analysis of EC DA concentration under different AMPH concentrations

The probability distribution of the logarithm of the EC DA concentration is obtained from multiple runs shown for tonic (A, C) and phasic (B, D) firing patterns and uniform (A, B) and nonuniform (C, D) DAT distributions varying AMPH concentrations. The distribution of the EC DA concentration is shown between 0.1 to 100 nM. Three different AMPH concentrations, 0 nM (green), 1 nM (black) and 10 nM (magenta) are used.

A secondary reason for the increased EC DA concentration under uniform DAT distribution is the increase in the number of interactions between DATs and intracellular AMPH molecules. Since DAT endocytosis and DAT phosphorylation events are initiated by intracellular AMPH, increased number of contacts results in higher EC DA concentration. Finally, the simulations are performed with low AMPH concentrations. The effect of the concentration of AMPH on the EC DA levels is determined to be similar under uniform DAT distribution (Figure 19). This is due to the diffusion limited nature of the model and the fact that the Rho activity from

AMPH is a rapid process. Simulation with higher AMPH concentrations is significantly slow due to the nature of spatial stochastic simulators. It will be valuable to see how one order of magnitude higher level of AMPH affects the efflux rate.

3.4 DISCUSSION

3.4.1 Overview

In this chapter, I expanded the model that is described in Chapter 2.0with the addition of psychostimulants and their interactions and performed MCell simulations with varying action potential firing patterns and DAT distributions. I determined the effect of cocaine is dependent on the concentration of cocaine at realistic DAT distribution. At low cocaine concentrations, the DATs in inward-facing states will overcome the shortage of the outward-facing DAT molecules and recover the DA efficiency. At high cocaine concentrations, cocaine can block a significant amount of DAT molecules, and the DA clearance efficiency reduces such that the EC DA concentrations increase. No simulations have been performed with a realistic description of cocaine molecules in a realistic geometry to date. The geometry and the localization of the molecules play a significant role in the function of cocaine since the measurements on the different regions of the brain such as substantia nigra (SNc), Nucleus Accumbens (NAc) and dorsal striatum (Str) showed that the effect of cocaine is significantly different (Nelson, Larson, & Zahniser, 2009). SNc and Str differ based on tortuosity of the cell membranes, void fraction of the space, density and distribution of DATs (Hoffman, Lupica, & Gerhardt, 1998; Rice & Cragg, 2008). Therefore, having a realistic geometry of the DAT can improve the accuracy of the prediction of the effect of cocaine.

The model developed in Chapter 2.0 is also expanded with the addition of AMPH molecules and its intracellular interactions. AMPH interacts with various molecules including G-proteins, Ca^{++} signaling proteins, and Rho. These interactions lead to two crucial mechanisms, DAT endocytosis and DAT phosphorylation, followed by DA efflux that modulates the EC DA concentration. MCell simulations were performed to investigate the effect of spatial complexity and firing patterns on the EC DA concentration with the presence of varying AMPH concentration. Under the uniform surface distribution of DAT, DATs efficiently uptake AMPH molecules, and the intracellular interaction network is activated. As a result, DAT endocytosis is promoted, and phosphorylated DAT starts to release DA molecules to EC space. The DA reuptake is also more efficient with a uniform distribution of DATs. The effect of AMPH on DA efflux and endocytosis is stronger than the effect on DA reuptake. Therefore, the EC DA concentration increases. On the other hand, nonuniformly distributed DATs are not able to uptake enough AMPH molecules to activate the AMPH-induced DA efflux pathway. Therefore, the effect of low AMPH concentrations under a non-uniform distribution of DAT is considerably small. The main addition of the realistic spatial model is the addition of the diffusion limitations for molecules like AMPH at low concentrations.

3.4.2 Cocaine inhibits DA reuptake at sufficient concentrations

MCell simulations were performed with three different cocaine concentrations: 0, half IC50 and IC50 levels of cocaine. The results show that under realistic DAT localization and distribution, the former two do not have a visible effect on the EC DA concentration. The mechanism of action of cocaine on DAT is competitive inhibition. Cocaine binds to the extracellular substrate-binding pocket of DAT and blocks the binding and translocation of DA molecules. In Chapter 2.0, the

steady-state distribution of DAT states was presented. A significant number of DATs is in the inward-facing state, which cannot be targeted by cocaine molecules. At low cocaine concentrations, inward-facing DATs transition to outward-facing conformation and keep DA clearance efficiency at a certain level. At high concentrations, the effect of inhibition is more pronounced since the amount of DAT molecules that are transitioned to the outward-facing state cannot keep DA clearance rate at a basal level. Simulations indicate features similar to those observed in experimental studies that measured the dose-dependency of the cocaine inhibition on DAT (Ferris et al., 2012). Generally, experimental studies are performed to understand the effect of repetitive administration of cocaine for an extended period of times such as hours and days (Ferris et al., 2012; Jones, Garris, & Wightman, 1995). However, the effect of cocaine at sufficiently high levels is visible regardless of the duration of the experiment.

3.4.3 AMPH uptake is the main regulator of DA efflux at low AMPH concentrations

MCell simulations were repeated with the addition of different concentrations of EC AMPH molecules. The results show that the AMPH has a significant adverse effect on DA clearance rate under a uniform distribution of DAT; whereas the effect is minor under nonuniform distribution. The main difference between uniform and nonuniform distribution is the efficiency of DA clearance rate due to the limited likelihood of interactions between volume molecules such as DA and AMPH with DAT (Chapter 2.0). The model is simplified from a complex reaction network composed of 66 reactions and 49 species by reducing the total number of reactions to 20 and species to 11. All the reactions inside the cell are assumed to be rate-limited except the interactions of AMPH with DATs, and the rate of AMPH and DAT interactions are modulated by the intracellular concentration of the AMPH. The DAT distribution also has a negative effect on the

likelihood of interactions between DAT and the intracellular AMPH. Therefore, the effect of AMPH is weakened both by AMPH uptake and intracellular AMPH diffusion. The uniform distribution of DAT shows that AMPH significantly affects the EC DA concentration.

AMPH is involved in several other interactions in the cell in addition to DAT endocytosis and DAT phosphorylation. It can induce vesicular release upon its interaction with VMATs. The model assumes that AMPH interaction with DAT is the critical modulator instead of the intracellular DA concentration. This assumption was justified in a previous study by using a reserpine-like compound which induces depletion of vesicles and increases in cytoplasmic concentrations (Jones, Gainetdinov, Wightman, & Caron, 1998). Even with the addition of reserpine-like compounds, the EC DA concentration is mainly controlled by AMPH concentration. Our simulations were performed at low concentrations of AMPH since it is computationally expensive to track intracellular molecules without degradation. In the DA reuptake model (Chapter 2.0), intracellular DA molecules were assumed to be degraded since the intracellular DA concentration is not a quantity of interest. Although, the concentrations of AMPH used in MCell simulations are slightly lower than those used in previous AMPH-induced efflux studies which are around 1-10 μM (Wheeler et al., 2015), high concentrations of AMPH did not result in higher efflux rate and additional AMPH molecules diffusion to nerve terminals due to the lipophilic nature of AMPH (Kristopher M. Kahlig et al., 2005).

3.4.4 Addition of key modulators to simulation environment make simulations more realistic

The current model reduced all the elaborate interaction scheme described in Figure 14 to two reactions: AMPH induced DAT endocytosis, and AMPH induced DAT phosphorylation. However, the AMPH molecules need to diffuse to intracellular regions to have interactions with signaling molecules such as Rho, TAAR1, and VMAT. It is possible to add those signaling molecules inside the cell with no diffusion to speed up the simulations. The interactions between AMPH and these molecules can be modeled to change the state of AMPH from inactive to an active state that can trigger the internalization and the phosphorylation of DATs. These reactions guarantee diffusion of AMPH molecules to intracellular regions which makes the model more accurate in terms of DAT activation. The high likelihood of interactions between intracellular AMPH and DATs exaggerate the rate of DA efflux and DAT endocytosis under uniform DAT distribution. In addition, the interactions between different states of DAT and intracellular AMPH could differ as explained in a previous study (Kristopher M. Kahlig et al., 2005).

4.0 MODELING AND ANALYSIS OF THE SUBUNIT EXCHANGE MECHANISM IN CAMKII SIGNALING

4.1 BACKGROUND

The primary function of the brain is to process information from the environment and respond accordingly. Neurons process information, receive and make connections with other neurons. On average, there are billions of neurons in the human brain, and the number of connections is in the order of trillions (Herculano-Houzel, 2009). The connections among neurons are called "synapses" and the signal is propagated through action potential in the central nervous system (CNS). Action potential causes depolarization on the presynaptic membrane of the neurons. The vesicles that contain neurotransmitter molecules move to the regions that are called 'active zones' on the presynaptic membrane because of depolarization and many neurotransmitters released to synapse from these regions. Neurotransmitter molecules diffuse and activate the receptors on the postsynaptic cells and trigger the downstream signaling. Depending on the response of neurotransmitters, neurons are divided into two categories: inhibitory and excitatory (Kennedy, 2013). In this chapter, I focused mainly on the excitatory synapses.

A large number of excitatory neurons are on the spinal regions. The number of synapses on such neurons is generally in the order of thousands (Kennedy, 2013). A typical example of an excitatory synapse is located between hippocampal (*Cornu Ammonis*) CA1 and CA3 neurons which plays a

crucial role in memory and learning. The postsynaptic membrane of this type of synapses has ligand-gated ion channels that are activated by neurotransmitters such as glutamate. The two receptor types that are activated by glutamate are α-amino-3-hydroxy-5-methyl-4-isoxazolepropionic acid (AMPA) receptor and N-methyl-D-aspartate (NMDA) receptor. AMPA receptor is activated by glutamate binding, and its primary function is the influx of sodium (Na^+) ions. NMDA receptors are structurally more complicated, and in addition to Na^+ ions, they allow calcium (Ca^{++}) ions into the cell. (Mayer, Westbrook, & Guthrie, 1984; Nowak, Bregestovski, Ascher, Herbet, & Prochiantz, 1984)

One of the most important mechanisms that are related to memory and learning is the synaptic plasticity, and it can be defined as the long-lasting strengthening or weakening of the spinal connections depending on the activity patterns. In high-frequency activation patterns, synapses become stronger by an increase in size and by addition of new receptors. This process is called 'long-term potentiation', LTP. On the other hand, low-frequency activity leads to a reduction in the size of synapses and the number of receptors. This process is called, 'long-term depression', LTD (Franks & Sejnowski, 2002). The effect of LTP and LTD remains longer than the duration of the activation. Both processes are controlled by Ca^{++} signaling.

One of the central regulators of calcium signaling in post-synaptic cells and LTP is the calcium-calmodulin-dependent kinase type II (CaMKII). CaMKII is activated by active calmodulin (CaM) and Ca^{++} complex. CaMKII and the Ca^{++} signaling pathway causes recruitment of AMPA receptors (Opazo et al., 2010) to the post-synaptic membrane and phosphorylation of the AMPA receptors that increases sodium conductivity leading to more efficient synapses (Lisman, Yasuda, & Raghavachari, 2012). CaMKII is one the highly expressed signaling kinases in the brain and more specifically in the excitatory neurons (Bennett, Erondu, & Kennedy, 1983;

Erondu & Kennedy, 1985; Sik, Hajos, Gulacsi, Mody, & Freund, 1998). CaMKII is located in various regions in neurons, but the highest expression level is in the postsynaptic density (PSD) which is the closest region to the postsynaptic membrane in the excitatory neurons (Kennedy, 2013).

CaMKII holoenzyme is structurally dodecamer, and the Ca^{++}/CaM activation has complex intramolecular dynamics (Bennett et al., 1983; Kolb, Hudmon, Ginsberg, & Waxham, 1998). Each subunit has an association module and a catalytic module which includes a flexible linker and a kinase domain. Association domains and kinase domains are connected via flexible linker region. The dodecamer holoenzyme is kept together with interactions between the association domains (Rosenberg et al., 2006; Rosenberg, Deindl, Sung, Nairn, & Kuriyan, 2005). Six of these association domains create a ring-like structure which is called 'central hub' (Stratton et al., 2014). Two of these hexamer structures compose the dodecamer holoenzyme. In the inactive state, the flexible linker folds and the catalytic domain positions very close to association domain. The binding region of the Ca++/CaM complex is very close to the linker region and kinase domains opens upon Ca++/CaM binding. There are three important threonine residues on the linker region, and phosphorylation of such residues regulates the activity of CaMKII (Rellos et al., 2010).

The first significant threonine residue is (T286) is an only catalytic module and located near the kinase domain. The phosphorylation of T286 keeps the kinase domain open even if the Ca^{++} concentration drops to a low level or CaM unbinds from the complex (Miller & Kennedy, 1986; Miller, Patton, & Kennedy, 1988). More interestingly, T286 phosphorylation is an inter-subunit event meaning that only an active (Ca^{++}/CaM bound or auto-phosphorylated) and neighboring CaMKII subunit can phosphorylate a Ca^{++}/CaM bound subunit (Hanson, Meyer, Stryer, & Schulman, 1994; Rellos et al., 2010). Thus, the initial CaMKII activity is strongly

dependent on the active CaM concentration, and the rate of Ca^{++} influx indirectly regulates the initiation of the CaMKII activity (Chao et al., 2010).

The other two threonine residues (T305 and T306) are located on the CaM-binding domain of the subunit and phosphorylation of such residues block Ca^{++}/CaM binding (Patton, Miller, & Kennedy, 1990). The effect of these two phosphorylation sites is not as apparent as T286, yet a knock-in study in mice shows the importance of learning and memory (Elgersma et al., 2002). Since this phosphorylation blocks the reactivation of the CaMKII by Ca^{++}/CaM binding, the protein phosphatases such as protein phosphatase 1 (PP1) and protein phosphatase 2 (PP2A) bring the CaMKII back to inactive state (Shields, Ingebritsen, & Kelly, 1985).

Recently, it is proposed that activated CaMKII subunits can initiate a subunit exchange between CaMKII holoenzymes (Stratton et al., 2014). The existing of such process is proved using a group of in vitro experiments. The suggested mechanism of the subunit exchange is the following: (I) Following T286 and T305 phosphorylation, the kinase domain docks on top of the association domain, (II) upon docking of the kinase domain, a vertical dimer of subunits can release from a holoenzyme, and (III), a free vertical dimer can bind to a holoenzyme and create a tetradecamer form of the holoenzyme (Bhattacharyya et al., 2016). Since the autophosphorylation of T286 is dependent on the activity level of a neighboring subunit, the subunit exchange mechanism is a plausible mechanism to spread CaMKII activity even in the absence of Ca^{++}/CaM (Lisman, 1994).

In modeling CaMKII dynamics, it is preferred to use a reduced kinetic scheme to overcome the combinatorial complexity caused by the multimeric structure of the holoenzyme. A mean field approximation of the kinetics with dimer or trimer holoenzyme assumption can reproduce the

frequency dependence of the CaMKII activation at short time scales (Michalski, 2013; Michalski & Loew, 2012). However, subunit exchange mechanism needs a proper description of the holoenzyme structure since the mechanism is involved in vertical CaMKII dimers. A complete deterministic model requires species with several states in the order of thousands. Therefore, building a network among such complex species is generally computationally expensive, and it is often impossible to generate reaction network above a certain size threshold. Network-free simulation approaches can efficiently deal with the problem of combinatorial complexity (Sneddon, Faeder, & Emonet, 2011).

The calibration of biological models is generally challenging due to the scarcity of experimental data and a large number of parameters involved with the system. Since these simulations of such models are computationally expensive, it is required to implement an efficient and scalable method to estimate the parameters of biological models. Genetic algorithms (GA) are one of the most widely used heuristic methods to solve optimization problems. However, it still needs to generate full-length trajectories to calculate the objective function of an individual parameter set. Online model checking (OMC) is a proper strategy that suggests terminating a simulation if a trajectory does not provide a pre-defined logic (Liu & Faeder, 2016). A genetic algorithm implementation with online model checking (GA/OMC) can provide a significant improvement on the performance of the parameter estimation.

Here, I build a detailed model of activation-triggered subunit exchange in CaMKII. The model is calibrated with a hybrid genetic algorithm implementation with online model checking based on experimental data of frequency dependence of the CaMKII activation at short time scales, and the amount of subunit exchange at long timescales. Even though the online model checking

and parallelization provides significant improvements, the parameter estimation procedure did not converge due to the size of the parameter space and slow simulations.

4.2 METHODS

4.2.1 Model construction

Rule-based modeling is a way of representing the interactions of multiple interacting molecules with multiple parts and states (Faeder, 2011). Because of a considerable number of interactions that are involved in multiple types of molecules, the total number of interaction possibilities grows exponentially. To capture all the possible interactions, an extensive network with a lot of edges and nodes is required (Hlavacek, Faeder, Blinov, Perelson, & Goldstein, 2003). Rule-based modeling provides a local representation of the molecular interactions. The local representations could convert into an extensive network using graph enumeration methods. For multimer molecules with multiple intramolecular interactions, the rule-based modeling is the only plausible method to construct a large model. BioNetGen language (BNGL) is a rule-based modeling language that uses graph formalism to enumerate all possible species and reactions of the system (Blinov, Faeder, Goldstein, & Hlavacek, 2004; Faeder, Blinov, & Hlavacek, 2009).

I constructed a detailed model of activation-triggered subunit exchange using a previously published model of CaMKII interactions as a basis (Michalski & Loew, 2012). This model includes interactions for an individual subunit, between subunits and holoenzyme level. The rules for intramolecular interactions can be divided into two groups depending on the species. The first group of rules identifies how Ca^{++} ions bind to CaM molecules and create Ca^{++}/CaM complexes then bind to CaMKII to trigger activation (Xia & Storm, 2005). There are four Ca^{++} ion binding

sites on CaM. Even though partially active CaM molecule with less than four Ca^{++} ions can bind and activate CaMKII, only CaM with four Ca^{++} ions assumed to be the trigger of the activity of CaMKII for simplicity (Michalski, 2013). The second group of the rules contains information related to different states and their transformations in CaMKII subunits. The CaMKII molecule has six individual states that are based on Ca^{++}/CaM binding, T286 phosphorylation and T305/6 phosphorylation (Figure 20A). CaMKII is an inactive state without any Ca^{++}/CaM molecules since the kinase domain is docked on the association domain and the substrate binding site is blocked (D_{uu}) (Rellos et al., 2010). Upon Ca^{++}/CaM binding, the kinase domain is displaced from the association domain (C_{uu}). In such a state, both the substrate and ATP binding sites are exposed, and the CaMKII is active (Rellos et al., 2010). The Ca^{++}/CaM bound state of the CaMKII can be autophosphorylated at T286 by a neighboring active CaMKII subunit (C_{pu}) (Rich & Schulman, 1998). Auto-phosphorylated subunit remains active even after the release of Ca^{++}/CaM complex. The T286 phosphorylation suppresses linker folding and keeps the activity of CaMKII (D_{pu}) (De Koninck & Schulman, 1998). Upon release of Ca^{++}/CaM complex T305/6 is being exposed and can be phosphorylated (D_{pp}) (Mukherji & Soderling, 1994). The T305/6 phosphorylation prevents Ca^{++}/CaM binding (Hanson et al., 1994) and it can return to inactive states via phosphatases PP1 and PP2A. Finally, an inactive CaMKII subunit can be phosphorylated at T305/6 with a slow rate (Dup) (Colbran, 1993). This state is inactive and inhibits the Ca^{++}/CaM binding (Figure 20B).

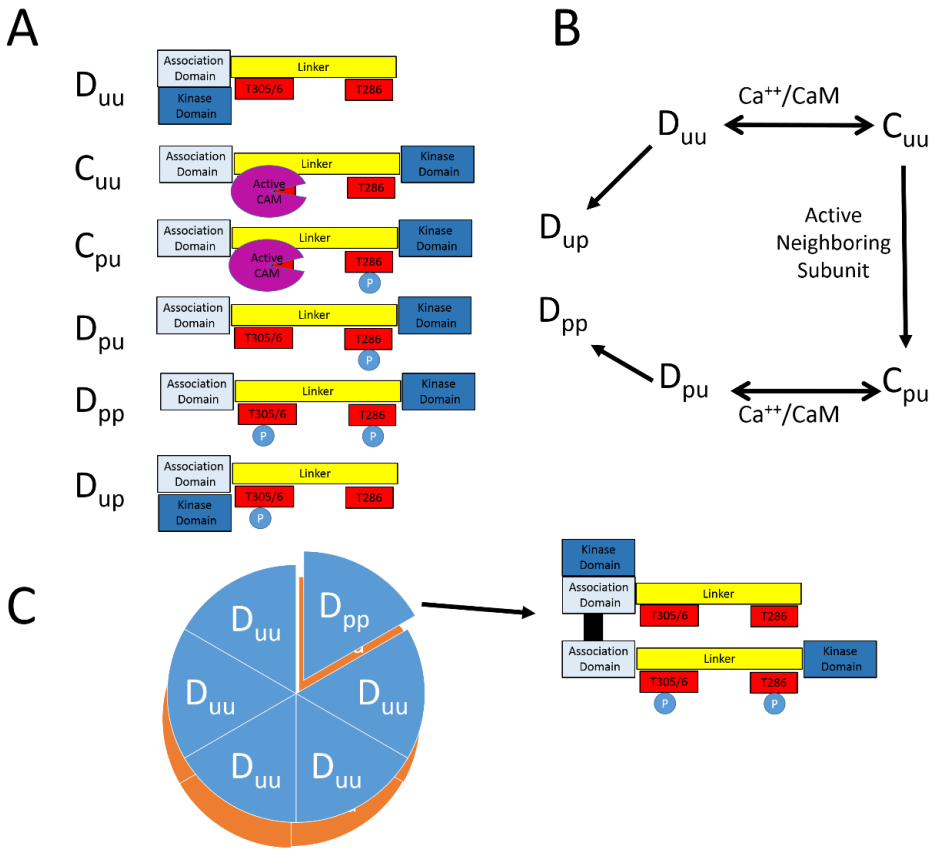

Figure 20. CaMKII model

A - The relevant states of CaMKII subunit. CaMKII subunit has three different domains. These domains are association domain (light blue), linker domain (yellow) and kinase domain (dark blue). The CaM is shown as a purple circle, and the phosphorylation sites are shown as red rectangles on the linker domain. D_{uu} state denotes the inactive state with no CaM and phosphorylation. C_{uu} state denotes the active CaMKII subunit with CaM and no phosphorylation on threonine residues. C_{pu} state denotes the CaM bound, and T286 phosphorylated active CaMKII subunit. D_{pu} is another active state with only T286 phosphorylation. D_{pp} is the active state with phosphorylation on both T286 and T305/6 sites. D_{up} is the inactive state with only T305/6 phosphorylation. In active states, the linker domain unfolds, and kinase domain is far from association domain. Both phosphorylation sites are on linker of close to the linker. B - Interactions in individual CaMKII subunit. The T286 phosphorylation is triggered by active neighboring subunit. C – The subunit exchange mechanism in holoenzyme. If one of the molecules is in D_{pp} state two vertical CaMKII subunit (vertical dimer) can release from CaMKII holoenzyme regardless of the state on the vertical neighbor. The thick black bond between association domains shows the binding between two association domains of the vertical dimer.

In a previous study (Michalski & Loew, 2012), the CaMKII holoenzyme is assumed to be a dimer, trimer or hexamer and the reduced scheme is hard-coded as an ordinary differential equation model. In my rule-based model, CaMKII holoenzyme is either dodecamer or tetradecamer and is formed by two vertical ring-like hexamer or heptamer structure. The subunit exchange mechanism includes six distinct process: (i) tetradecamer opening, (ii) release of a vertical subunit from tetradecamer, (iii) diffusion and binding of vertical dimer to open dodecamer, (iv) tetradecamer closing, (v) dodecamer opening and (vi) dodecamer closing (Bhattacharyya et al., 2016). For the simplicity opening and closing events are assumed to be more rapid compared to release and binding events. A vertical dimer could be released if one of the subunits is in D_{pp} state Figure 20C. The kinetic parameters of the interactions of individual subunits are used from a previous study (Michalski & Loew, 2012) and given in Table 6. The parameters for subunit exchange are estimated.

Table 6. Kinetic parameters of the CaMKII model adopted from (Michalski & Loew, 2012)

Parameter	Explanation	Value	Source
$k_{on,0}$	1st Ca++ binding	2.5 μM^{-1} s^{-1}	(Chiba, Schneider, Matsuoka, & Noma, 2008)
$k_{off,0}$	1st Ca++ unbinding	50 s^{-1}	
$k_{on,1}$	2nd Ca++ binding	88.25 μM^{-1} s^{-1}	
$k_{off,1}$	2nd Ca++ unbinding	50 s^{-1}	
$k_{on,2}$	3rd Ca++ binding	12.5 μM^{-1} s^{-1}	
$k_{off,2}$	3rd Ca++ unbinding	1250 s^{-1}	
$k_{on,3}$	4th Ca++ binding	250 μM^{-1} s^{-1}	
$k_{off,3}$	4th Ca++ unbinding	1250 s^{-1}	
$k_{off,u}$	CaM unbinding from unphosphorylated CaMKII	2 s^{-1}	(Meyer, Hanson, Stryer, & Schulman, 1992)
$k_{on,u}$	CaM binding to unphosphorylated CaMKII	30 μM^{-1} s^{-1}	
$k_{off,p}$	CaM unbinding from phosphorylated CaMKII	0.001 s^{-1}	
$k_{on,p}$	CaM binding to phosphorylated CaMKII	10 μM^{-1} s^{-1}	
r_1, r_2	C_{uu} to C_{uu} phosphorylation	1.0 s^{-1}	(Michalski & Loew, 2012)

r_3	D_{pu} or D_{pp} to C_{uu} phosphorylation	0.8 r_1	
r_{305}	D_{pu} to D_{pp} phosphorylation	10 s^{-1}	
r_{basal}	Basal phosphorylation	5 x 10^{-4} s^{-1}	(Colbran, 1993)
k_{cat}	Phosphatase catalysis rate	1.72 s^{-1}	(Bradshaw, Kubota, Meyer, & Schulman, 2003)
K_m	Phosphatase half-max concentration	11 µM	

4.2.2 Experimental data

The constructed model has some missing parameters, and these parameters need to be estimated. For the estimation of the subunit exchange parameters, two groups of experimental data are used. The first group is the CaMKII activity level data response to various Ca^{++}/CaM stimulations with various dose, frequency, and stimulation period (De Koninck & Schulman, 1998). In(Michalski & Loew, 2012), it is stated that the given parameter set reproduces the input frequency dependence of CaMKII activation (Michalski & Loew, 2012). Therefore, the addition of subunit exchange should not change the activity levels of CaMKII on the experimental data. The second group of the data contains the colocalization amount of the red and green fluorescence. As a result of activation-triggered subunit exchange of CaMKII holoenzymes with different Ca^{++}/CaM concentrations and some genetic modifications on CaMKII subunits (Stratton et al., 2014).

The first group of the data is collected from the following three different types of experiments. The first type of the experiment is the activity level at 6 seconds after continuous exposure to varying concentrations of Ca^{++}/CaM levels for 6 seconds (Figure 21A). The second

experiment is the response level of the CaMKII to various frequencies of 200 ms pulses of 0.1 μM of Ca^{++}/CaM complex (Figure 21B). The third experiment is the measurement of CaMKII activity level with respect to different pulse durations with various frequencies leading up to the same exposure time to Ca^{++}/CaM complex in total (Figure 21C). These experiments are completed in a short time scale with a maximum of 100 seconds.

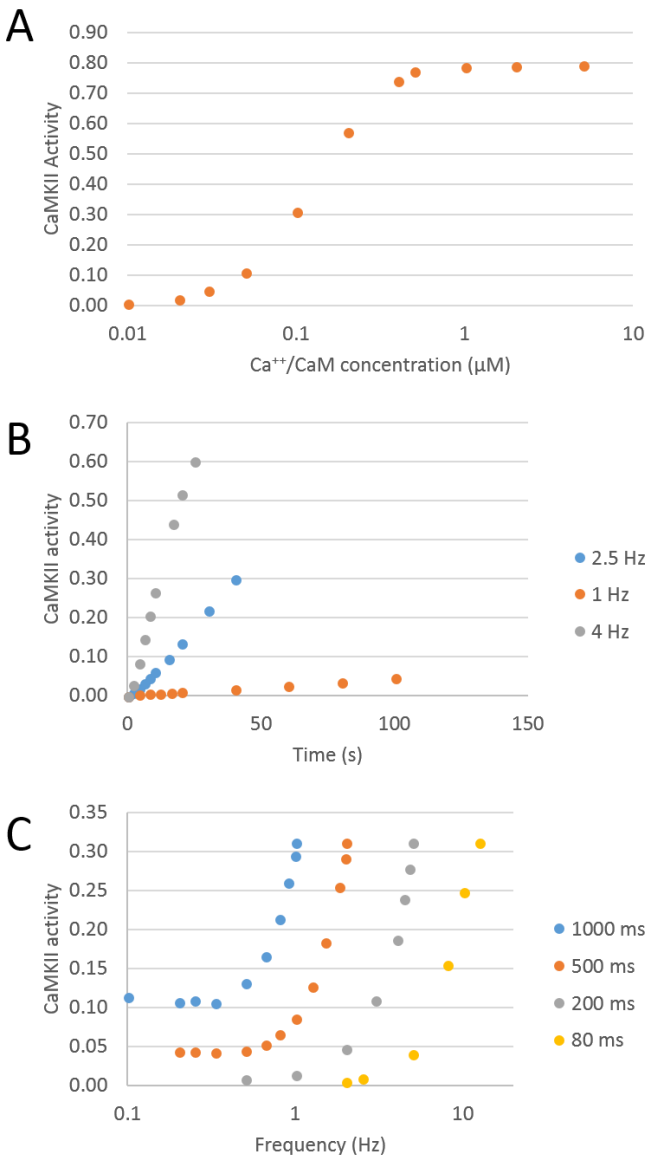

Figure 21. Frequency-dependent CaMKII activation data

A – Activity level of CaMKII to continuous 6 seconds exposure to varying concentrations of CaM. The EC50 values are around 0.2 µM. B – CaMKII activity as a function of time with different frequencies of 1 Hz (orange), 2.5 Hz (blue) and 4 Hz (gray) of 200 ms pulses. The number of pulses for frequencies are 100, 40 and 25 for 1 Hz, 2.5 Hz, and 4 Hz, respectively. The total duration of the exposure to Ca^{++}/CaM is the same for all three frequencies. C – CaMKII activity as a function of frequency and individual pulse duration. The different pulse lengths 1000 ms (blue), 500 ms (orange), 200 ms (gray) and 80 ms (yellow) are shown. The total CaMKII exposure time for each data point is 6 seconds.

The second experiment is the measurement of the colocalization of different colored CaMKII molecules with different concentration of Ca^{++}/CaM and modifications of CaMKII subunits such as mutations at phosphorylation sites (Stratton et al., 2014). In the experimental setting, half of the CaMKII holoenzymes are tagged with red color Alexa 594 fluorescent dye and the other half are tagged with green color Alex 488 fluorescent dye. All CaMKII holoenzymes are immobilized using the biotin-streptavidin connection on polyethylene glycol (PEG)-treated glass (Figure 22A). At certain time points, a portion of the CaMKII molecules are removed from the experiment, and a multicolor total internal reflection fluorescence (TIRF) microscopy is performed. The colocalization data is filtered, and the ratio of the colocalization to the maximum colocalization observed if all the CaMKII holoenzymes have both red and green color is reported. The experimental data reported for different concentrations of Ca^{++}/CaM (Figure 22B) and, for complete mutation of T286D which creates constitutively active CaMKII in the absence of Ca^{++}/CaM (Figure 22C). These experiments are completed in timescales of minutes to hours that is larger compared to the first group of experiments. There is a major drawback of these experimental data. There are 66 different configurations with red and green color colocalized CaMKII subunits. The colocalized holoenzymes might have only one red and eleven green subunits or six green and six red subunits. Therefore, experimental data may not be the best data to use for a quantitative task, yet it is the only available quantitative data to fit in this context.

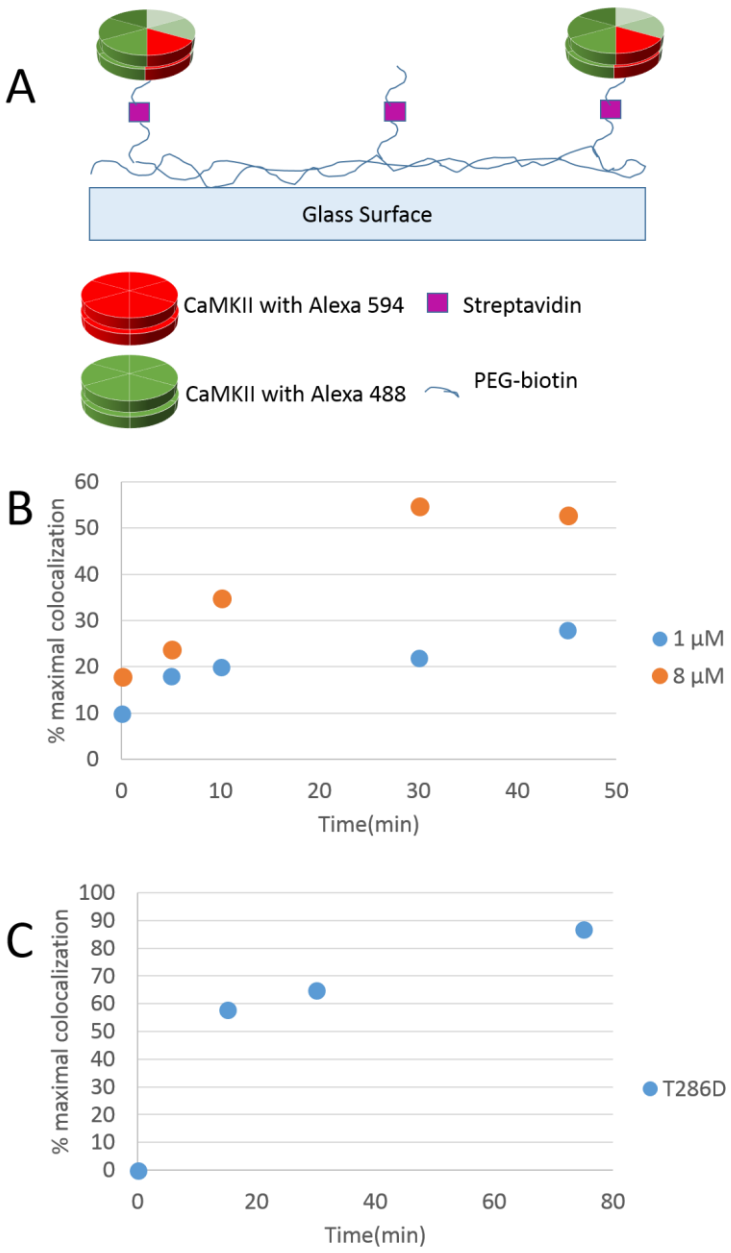

Figure 22. Activation triggered subunit exchange data

A – CaMKII holoenzymes are immobilized using PEG-biotin-streptavidin functionalization. Because of subunit exchange, green and red subunits are colocalized. B – The percent colocalization to maximal colocalization under different Ca^{++}/CaM concentrations, 1 µM (blue) and 8 µM (orange). The experimental data is collected for 45 minutes. C – The percent colocalization to maximal colocalization wit T286D mutation. The T286D mutation makes CaMKII subunit active regardless of Ca^{++}/CaM concentration.

4.2.3 Network-Free simulations

In conventional rule-based modeling, the interactions of individual species are defined as rules, and all possible combinations of rules (reactions) are generated using graph enumeration strategies. In general, small to medium size rule-based models (<10000 reactions) can be simulated using network generation followed by integration of ordinary differential equations or application of a stochastic method such as Gillespie (Sneddon et al., 2011). If reaction network size is larger than 10000 or infinite, rule-based models are simulated using a network-free strategy to overcome the problem of combinatorial complexity.

In network-free simulations, each species is defined as a particle, and their transitions are regulated by the rule definitions. A Monte Carlo update scheme is used to transform each species to its next state at runtime (Monine, Posner, Savage, Faeder, & Hlavacek, 2010). At each time step, the following procedure is followed: (i) patterns of reactants are defined at rules are identified in the molecular complexes, (ii) propensities of rules are calculated, (iii) depending on the propensity of a rule, transformations are selected and (iv) transformations are applied to a randomly selected species that contains the reactant pattern of the rule. The propensities are calculated, and transformations are triggered at runtime. There is no need to create a reaction network as in the case of network-based simulation methods. An efficient implementation of network-free simulations for rule-based models is available in NFsim tool (Sneddon et al., 2011). NFsim provides a flexible environment for simulating models that are built in BNGL framework and have a large number of states/reactions. In this study, all CaMKII models are simulated using NFsim software.

4.2.4 Genetic algorithms with online model checking

Parameter estimation is a common problem in building models of biological systems. For small rule-based models, it is generally preferred to use Bayesian techniques such as Markov Chain Monte Carlo. However, such methods require a large number of model simulations and Markov Chain properties limit the parallelization capabilities (Ballnus, Schaper, Theis, & Hasenauer, 2018). In the case of large models that require long CPU time, it is better to use a heuristic method with a parallel implementation. GA is one of the most commonly used optimization methods due to easy parallelization (van Soest & Casius, 2003).

GA has the following steps: (i) Simulate the model and evaluate the objective function for each parameter set. (ii) Create a new population based on pre-defined rules such as selection, crossover, mutation. The selection is defined as the removal of parameter sets with high objective functions. The crossover is defined as the exchange of parameters between the two parameter sets. The mutation is defined as a random change of an individual parameter in a single parameter set. (iii) Replace the high objective function parameter sets with the newly created ones. Since the simulation of a trajectory is entirely dependent on the individual parameter set, all the trajectories can run in an embarrassingly-parallel way. With a large number of processors, the generations are faster, and the estimation problem can rapidly converge. BioNetFit is an efficient, flexible, open-source implementation of parameter estimation tool using GA for BNGL models (Thomas et al., 2016). BioNetFit has its own parallelization method that can work on various computer cluster environments.

Even with a complete parallelization of the simulations, GA methods may not converge due to time limitations on a computer cluster environment. The most computation intensive part

of any parameter estimation procedure is generating a trajectory for each parameter set. Online model checking, combines simulation with model checking in shorter time intervals instead of a complete simulation followed by objective function evaluation (Liu & Faeder, 2016). The model checker returns a decision at each time point with an experimental data. If the trajectory significantly diverges from the experimental data, the parameter set is terminated, and a new trajectory with a new parameter set is initiated (Figure 23).

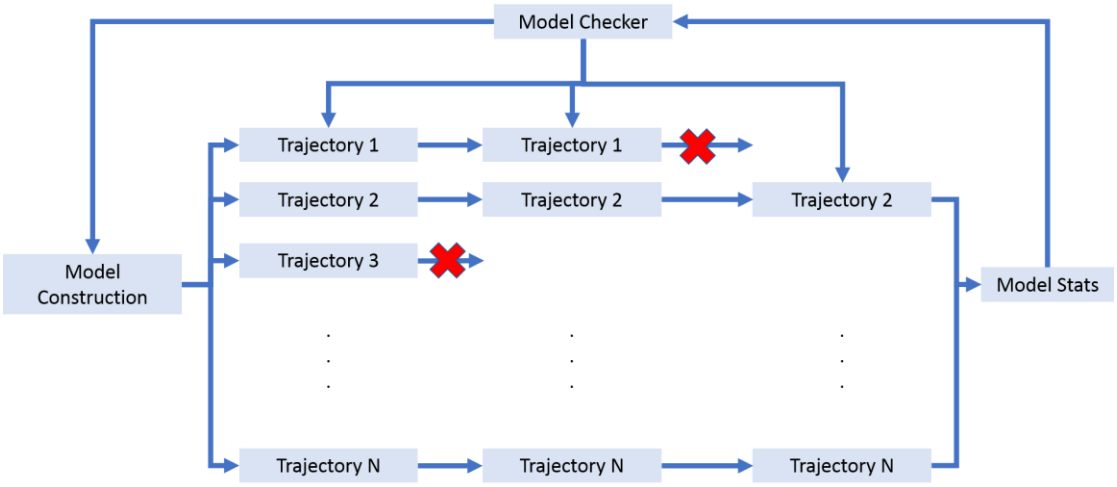

Figure 23. Schematic description GA implementation with model checking

Multiple trajectories with different parameter sets are created for a given model. Instead of a full trajectory, simulations are performed until a time point with pre-defined logic information. At this time point, each trajectory is evaluated for the pre-defined logic. If it fails, the simulation is started from the previous checkpoint. If it is successful, the simulation proceeds until the next time point. Many trajectories are rejected before they reach to complete length of trajectory. Instead of linear CPU time per generation, an adaptive CPU time per generation model is used.

4.3 RESULTS AND DISCUSSION

4.3.1 Subunit exchange can take place in timescales from minutes to hours

Prior to parameters estimation, a sensitivity analysis of the dissociation constant of vertical dimer from tetradecamer CaMKII is performed. The range of the parameters in the scan is ranging from 0.01 μM to 100 μM. The model simulated for 6 seconds of the continuous pulse of Ca^{++}/CaM complex with varying concentrations. A total of 1 μM CaMKII subunits are in the solution. The results of the parameter scan are given in Figure 24. The results show that changing the value of the dissociation constant does not have any significant effect on the CaMKII activity (Figure 24A). It is expected because the subunit exchange events started to occur after longer time scales around minutes. The CaMKII subunits need to reach to double phosphorylated and CaM unbound state (D_{pp}) 6-second simulations are not enough to D_{pp} state of CaMKII.

On the other hand, regardless of the dissociation constant of the vertical dimer, vertical dimer release is almost never observed in Figure 24B because CaMKII subunits never reach to D_{pp} state. Further analysis on the amount of CaMKII in D_{pu} state shows that after CaMKII binding and T286 phosphorylation, CaMKII subunit remains in D_{pu} state for hours. Therefore, the model does not thoroughly capture the subunit exchange dynamics of CaMKII.

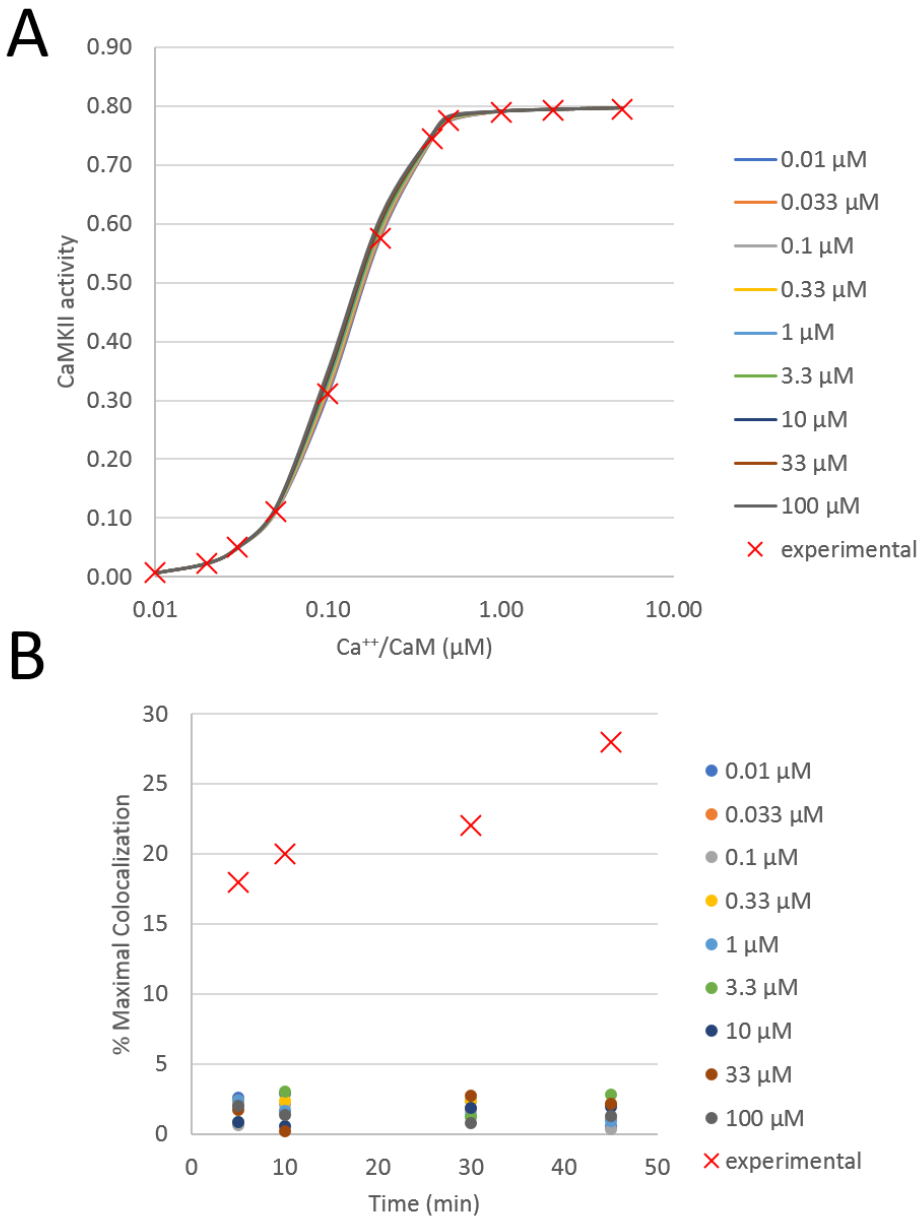

Figure 24. Parameter scan results for varying dissociation constant.

A – The CaMKII activity level is evaluated with varying Ca^{++}/CaM concentrations of 6 seconds of the continuous pulse. Different colors denote different dissociation constant for vertical dimer binding/unbinding to holoenzyme. The difference between the curves is slight. The experimental data are shown as red "x". B – The percent maximal colocalization is evaluated for 45 minutes varying vertical dimer dissociation constant from holoenzyme. Each color shows a different dissociation constant denoted in the legend. The experimental data are shown as red "x."

A widely studied mechanism in CaMKII intrasubunit dynamics is the 'Calmodulin Trapping' mechanism. An active Ca^{++}/CaM complex binds to CaMKII, and upon phosphorylation at the T286 site, Ca^{++}/CaM complex moves to a different region on CaMKII surface with a high binding affinity. Thus, CaM is trapped in CaMKII which keeps it activated for a long time. However, the existence of subunit exchange shows that the CaM trapping should not last longer than subunit exchange occurrence. Previous models that are calibrated based on short time scale experiments modeled the CaM unbinding from the C_{pu} state with mass action kinetics and select a binding rate which is thousand times slower than CaM unbinding rate from C_{uu} state. The results show that parameters such as binding/unbinding rate constants of CaM from/to C_{pu} state and D_{pu} to D_{pp} phosphorylation rate constant also needs to be estimated.

4.3.2 GA implementation with NFsim fails due to the size of the model

Since the size of the model is extremely large (over a billion reactions) and several of the molecules are not considerably small (>1000), using a conventional Bayesian technique for parameter estimation is not feasible. GA method is a parallel heuristic algorithm that is used for optimization problems. BioNetFit is an efficient and flexible GA implementation for BNGL models. BioNetFit provides a scalable implementation for parameter estimation tasks on models with one or multiple types of experimental data using NFsim as the simulation engine. Due to the stochasticity of the network-free simulations, it is required to have repeated simulations to have statistically significant estimates, and it is possible to simulate individual trajectories with the same parameter set for multiple times.

For objective function definition, a chi-square function is used. For each time point, the Z-score is calculated using the mean value and the standard deviation. The chi-square error is calculated with the following formula:

Equation 8

$$\chi = \sum_i \frac{(y_i - \hat{y}_i)^2}{{\sigma_i}^2}$$

where y_i is the simulation data, $\hat{y}_i$ is the mean value of the experimental data at time point i and σ_i is the standard deviation at time point i. The other important parameters are selected as the following: recombination rate of 0.5, the mutation rate of 0.2 and mutation amplitude of 0.1 are used. Using a GA implementation with a population size of 50, repeat number of 50 and a total of 300 generations, the subunit exchange rate constants and Ca^{++}/CaM binding/unbinding rate constants for phosphorylated CaMKII (C_{pu}) are estimated. A large group of trajectories are not completed or failed to simulate due to limitations on the computer infrastructure and limitations on the memory. NFsim calculates the propensity for each individual rule based on pattern matching on individual species. Since the size and the structure of the species are quite large in CaMKII model, is the task is memory intensive. Reducing the number of repeats to 3 helped GA to converge based on relative change in the objective function yet the final objective function is not ideal. A large portion of data from the frequency dependence of the CaMKII activation experiments are in good agreement yet there is a significant difference between subunit exchange experiment values. Therefore, a more efficient parameter estimation strategy which is less memory intensive needs to be implemented. A hybrid GA/OMC strategy can resolve the memory problems.

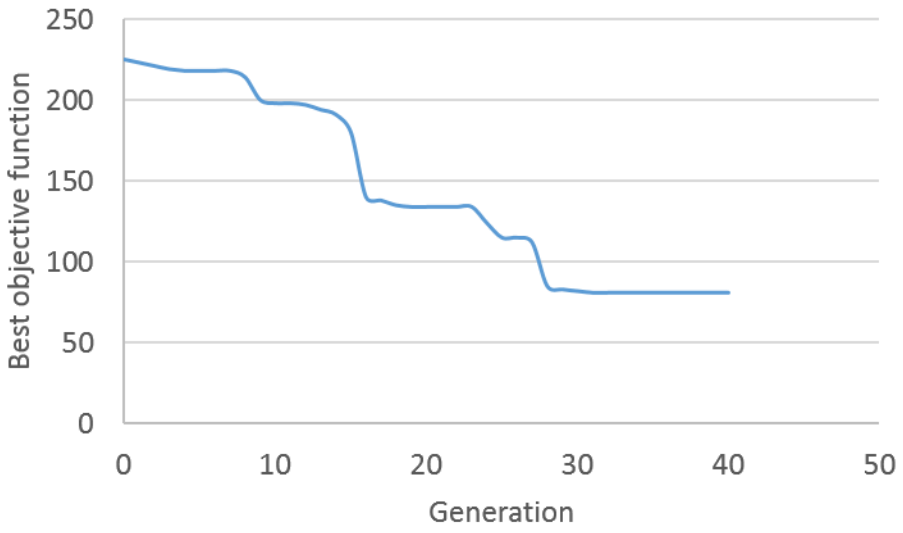

Figure 25. Best calculated objective functions for different generations

The chi-square objective function is evaluated for each parameter set at each generation, and the lowest chi-square value is plotted. After 40 generations, the objective function stuck around 81, and the simulation is converged since the best objective function did not change for 10 generations.

4.3.3 GA with Online Model Checking

Online model checking is an auxiliary parameter estimation strategy that speeds up the convergence rate of the optimization. The most expensive calculation in any parameter estimation method is the trajectory generation. In the offline mode of the genetic algorithm, all trajectories are entirely generated for each parameter set then parameters are updated according to estimated objective function. Many of the generated trajectories have large objective functions and do not provide useful information for the generation of the next parameter set. In online mode, each simulation trajectory is simulated for a shorter amount of time and based on a pre-defined logic; model checker decides to proceed with the next time interval or terminate the simulation and initiate a new simulation with a new parameter set. Since CaMKII model does not have any pre-

defined logic, model checker checked that the absolute error of an individual trajectory is less than one standard deviation at this time point.

Before applying OMC on the CaMKII model, the method is tested on the trivalent ligand and bivalent receptor (TLBR) model. TLBR model is a simple model with only three rules and two molecule types. However, the receptor has two identical binding sites, and ligand has three identical receptor binding sites. Therefore, two molecule types and three rules create a reaction network with infinite size due to the presence of the identical binding sites on multiple molecules. A detailed description of the model is given in (Monine et al., 2010). For the simplicity, instead of using NFsim as simulation engine, we used the SSA method (Gillespie, 2007). We kept the maximum iteration number as three in network generation and a reaction network with 19 species, and 29 reactions are created. Using the parameters given in Table 7, the output is generated at 10 different time points and due to stochasticity simulations are repeated 50 times. The total number of LR clusters, LR motifs, free receptor sites and free receptor monomers are generated. The average values and the standard deviations are used to prepare a synthetic experimental data as input to hybrid OMC/GA. The generated experimental data with standard deviations are given in Figure 26.

Table 7. Parameters for TLBR model

Parameter	Value	Unit
Total Ligand	50000	
Total Receptor	3000	
Free binding parameter	2.7	s^{-1}
Crosslinking parameter	16.8	s^{-1}
Dissociation rate	0.01	s^{-1}

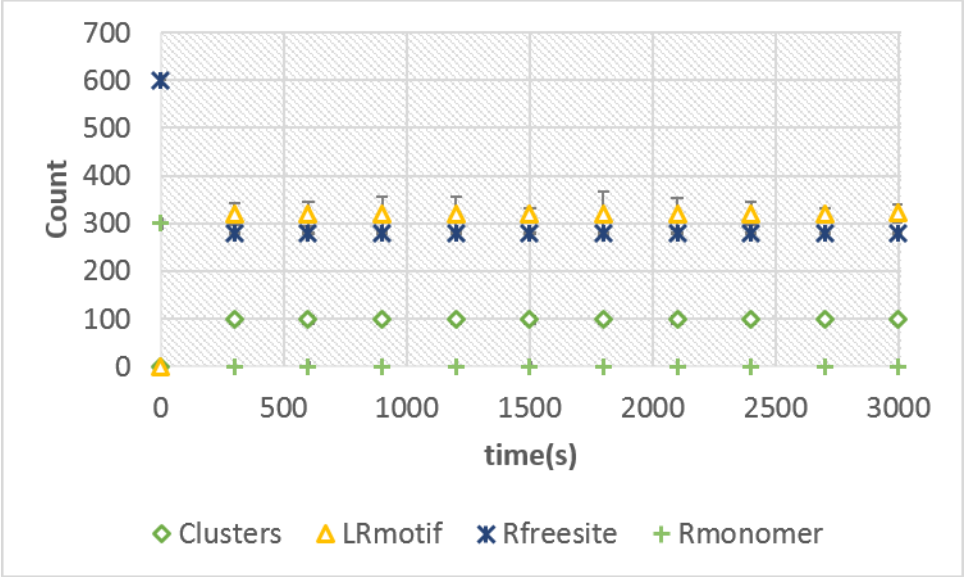

Figure 26. The data generated for parameter estimation from TLBR model.

The synthetic data is presented. The clusters (green diamond) are the species with at least two receptors cross-linked with ligands. The LRmotif (yellow triangle) is the number of ligand-receptor bounds. Rfreesite (blue "X") is the total number of ligand binding sites on the receptors. Rmonomer (green cross) is the total number of receptors that do not have any bound with ligands. The simulations are performed for 3000 seconds and every 300 seconds the mean and the standard deviation of the simulation output is calculated as synthetic data.

The parameter estimation is performed with conventional GA and GA/OMC methods. The parameters for the GA implementations are the following: recombination rate of 0.5, the mutation rate of 0.2 and mutation amplitude of 0.1. Each generation has 50 parameter sets, and each parameter is simulated 50 times with a different random number of seeds until convergence. The change in the best objective function for each generation and the total number of model evaluation are plotted in Figure 27. Since the trajectories which are one standard deviation away from the average experimental data points at a given time point are rejected, GA/OMC drops down to a reasonable parameter value in the first generation. However, the GA method stays at a high objective function value for many generations. The number of function evaluations in the

GA/OMC method is significantly larger compared to the GA method for the first couple generations due to online rejections. Even though the number of function evaluations is significantly large, none of the rejected trajectories simulated until it reaches to last experimental point. In the initial stages of the conventional GA method, the drop in the objective function is considerably slow compared to GA/OMC.

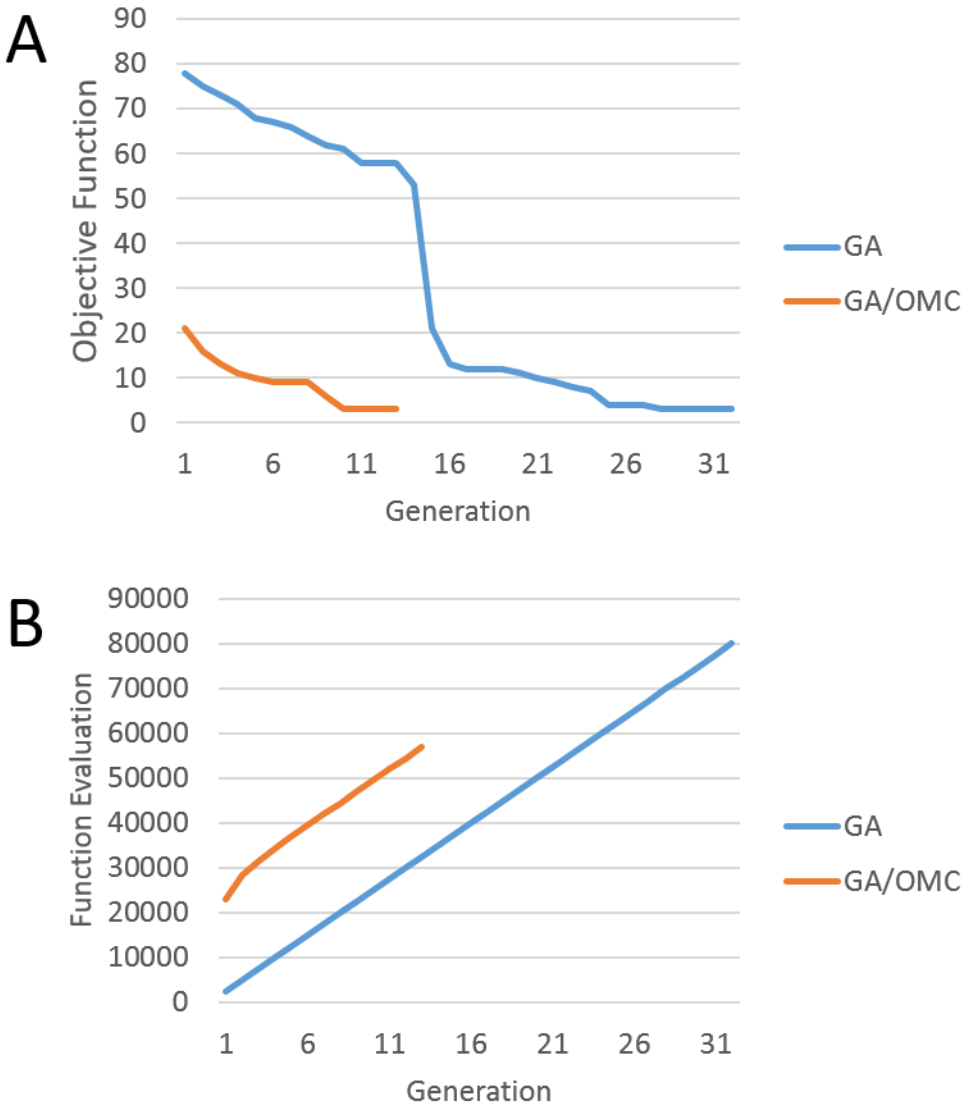

Figure 27. Performance of the hybrid GA/OMC method

A – The change in the best chi-square objective function evaluated for each generation is plotted. The blue curve shows the GA output, and the orange curve shows the GA/OMC output. In GA/OMC method, the best objective function at the end of the first generation is significantly small. In GA, the objective function drops after 13th generation. B – The total number of function evaluations are plotted. The linear blue curve shows the GA and orange curve shows the GA/OMC. GA/OMC have a significantly large number of function evaluations at first generation, and it converges to the same number of function evaluations with GA after a couple generations.

The results show that GA/OMC method converges significantly faster compared to conventional GA method both in terms of generations and number of function evaluations. A significant portion of the computation is performed at the early generations due to rejections based on pre-defined logic, and later stages have the same number of function evaluations with conventional GA. A hybrid GA/OMC method may overcome the efficiency issues of GA.

I tried to apply the GA/OMC method to the subunit exchange model of the CaMKII. NFsim can output the current state of the simulation and can load a given state as input if species have less than 20 molecules. If a species contains more than 20 molecules, NFsim cannot load such species without losing information and results are considerably different from the real trajectory. Due to limitations in NFsim, it is impossible to test the suggested GA/OMC method on a model with the size of CaMKII.

4.4 CONCLUSION

CaMKII is one of the most complex proteins in human CNS. It is generally known for its long-lasting activity after long-lasting stimulation, which can be explained by the activation-triggered subunit exchange mechanism identified in recent qualitative experimental studies [REF]. Constructing a quantitative model of such an extensive system still remains a challenge. The following lessons were learned from the construction of the model: (i) CaMKII models constructed based on rapid events after exposure to Ca^{++} cannot quantitatively reproduce the activation-triggered subunit exchange mechanism. (ii) The parameter search space for CaMKII is large, and even scalable heuristic methods for parameter estimation, such as genetic algorithms, fail to find the global optimum. (iii) The model checker implementation improves the efficiency of the

parameter estimation by application of genetic algorithms. However, the improvement is still not adequate to perform parameters estimation with CaMKII model.

5.0 CONCLUSION

In this work, I built a detailed 3D structure of dopamine (DA) neurons including the location of the active zones and surface distribution of dopamine transporters (DATs) from various microscopy studies. I performed spatial diffusion-reaction simulations with varying firing patterns and transporter surface distributions. I reported the effect of simulation conditions on the local and global distributions of DA molecules in the striatum. These simulations provide information on how cellular morphology and surface distribution can affect DA clearance efficiency and DA receptor activation. It is shown that heterogeneity in the surface distribution of DAT reduces the DA clearance rate, and increasing heterogeneity makes the effect more drastic. The results show that the DA dynamics are diffusion controlled. However, in addition to DA-binding kinetics to outward facing DAT, the equilibrium distribution between the inward- and outward-facing DAT is also a major factor for DA clearance efficiency.

I created a multiscale model to study the effect of psychostimulants on DA signaling in the presence of spatial complexity. The effects of cocaine and amphetamine (AMPH) are studied using a spatially realistic model. The mechanism of action of the cocaine is straightforward: cocaine completely shuts down the DAT and DA clearance, and the spatial complexity does not have a significant effect. For AMPH, it is required to build a two-scale model, an inner one with spatial resolution and an outer one that treats the network components as well-mixed. The network level model provided information related to intracellular AMPH concentration and the DA efflux from

DAT, and the spatial model focused on how DA is cleared and AMPH translocated into the cell. The results show that even low doses of AMPH can disturb the Rho pathway and increase the rate of DA efflux by 1000-fold.

I also built a detailed quantitative model of calcium-calmodulin-dependent kinase type II (CaMKII) dynamics with an activation-triggered subunit exchange mechanism. Rule-based modeling and network-free simulation tools enabled us to develop and simulate a large CaMKII model with an infinite number of possible reactions. The constructed model is calibrated using heuristic parameter estimation approaches. Due to the long time required for individual simulations and limitations on the simulation software, the parameter calibration did not converge to a reasonable parameter set even using advanced methods for optimization. A recently developed hybrid model checking/genetic algorithm method shows promising results for efficient parameter estimation that can overcome this bottleneck. Further development on the network-free simulations with this hybrid method can help the estimation of subunit exchange related parameters in activation-triggered subunit exchange model for CaMKII. The calibrated model might provide insights into the activation dynamics of CaMKII.

5.1 LIMITATIONS

The results presented in this dissertation show that our multiscale model for DA signaling is accurate, and our quantitative CaMKII model includes a detailed description of critical intramolecular events, but the following limitations need to be considered when interpreting the results:

a. The molecular simulations yield insights about events and provide reasonable estimates for accessible states, their equilibrium probabilities, and relative interconversion rates, which are used in the cellular simulations. However, the absolute rates of transitions involve many factors, and it is currently not possible to accurately predict those values.

b. The box of 10 x 10 x 7.2 μm^3 is large enough to simulate diffusion events that are of the order of seconds and take place around the synapse and surroundings. If there are events that are initiated at relatively distant loci from the synapse, such as DAT recycling, a larger simulation box is required.

c. The intracellular signaling pathway does include major players related to DA efflux. However, all intracellular reactions are assumed to be diffusion independent except AMPH reactions. If some of the intracellular signaling molecules are limited to specific compartments such as endoplasmic reticulum, the compartmental localization of these biomolecules needs to be specified in the model.

d. The CaMKII model can only be simulated with a limited number of CaMKII molecules. The network-free simulations use an agent-based strategy that keeps information about the state and interactions of every single species in the simulation. As a result, the number of CaMKII and CaM molecules in the simulations and the memory requirements are correlated. If the number of molecules reaches more than 10,000,000, it is not possible to simulate the system with 32 GB of memory. Such large numbers of molecules can be required to simulate multiple post-synaptic cells or to simulate a full post-synaptic cell with many CaM molecules. Even though CaMKII

molecules are limited to post-synaptic density area, CaM can be uniformly distributed. Therefore, the CaMKII model has size limitations for network-free simulations.

5.2 FUTURE WORK

The work presented in this dissertation suggests the following future directions:

5.2.1 Parkinson's disease condition implementation

In Parkinson's disease, DA neurons lose their function and stop releasing DA to the extracellular (EC) space. A simple implementation of this disease is based on rendering some of the DA active zones inactive. These simulations are performed, and preliminary results show that the EC DA concentration is significantly reduced if the number of active axons is reduced. Because of low activity at active zones, the EC DA concentration is dropped down to low levels (< 10 nM) locally. Another aspect of the Parkinson's disease is the shrinkage of inactive DA neurons. In the spatial model, the void fraction could be increased. Consequently, the EC DA concentration would be reduced due to increased extracellular space. The Meshmorph is an algorithm to adapt the void fraction of a given geometry without causing disruptions on the surface (J. Kinney, 2009). The DA receptor activation can drop to low levels as a result of the low activity.

5.2.2 Improvement of vesicular DA release mechanism

The vesicular release mechanism is dependent on the magnitude and the frequency of the action potential (Lodish, 2000). In the spatial DA reuptake model, a heuristic equation is used to

determine that an action potential triggers a vesicular DA release (Dreyer et al., 2010). However, the vesicular release event is the last step of a complex pathway triggered by calcium that is transported to the cell by voltage-gated calcium channels. The voltage-gated calcium channels uptake Ca^{++} ions from extracellular space. Ca^{++} ions can diffuse through intracellular regions and bind to synaptotagmin molecules which control the release events at the docked vesicles in the active zone. There are computational spatial models available for both N-type Ca^{++} channels (Dittrich et al., 2013), which are highly populated on DA neurons and DA vesicular release activation on Ca^{++} (Nadkarni, Bartol, Sejnowski, & Levine, 2010). The input of the N-type calcium channels is the membrane potential with respect to time. To generate changes in membrane potential, it is possible to use NEURON, a software that uses the cable equation to simulate the dynamics of neurons and neural networks (Hines & Carnevale, 1997). There is also a database called "ModelDB" for models that can be simulated by NEURON (Hines, Morse, Migliore, Carnevale, & Shepherd, 2004). A network model of DA neurons under different stimulation patterns (tonic and phasic) is also available in the database (Canavier & Landry, 2006). Use of the NEURON model to generate membrane potential data is a proper way to provide action potential input to voltage-gated calcium channels followed by Ca^{++} uptake into the cell.

5.2.3 A more realistic placement of DA receptors

In the spatial DA reuptake model, DA receptors are not explicitly defined and are assumed to be uniformly distributed. Based on the half-activation concentration (EC50 values) of low- and high-affinity receptors, the activation amounts are determined. The low-affinity DA receptors are generally activated around the DA synapses since their EC50 values are around 1 µM. On the other hand, high-affinity receptors are generally on DAT expressing cells, but their localization is not

known. The explicit representation of DA receptors can be implemented in the DA reuptake model by assuming a uniform distribution of DA receptors on DA neurons. To make more precise predictions, it would be possible to use another imaging study (Sedaghat, Nantel, Ginsberg, Lalonde, & Tiberi, 2006) to determine the heterogeneous distribution of DA receptors. The effects of the distribution of receptors in addition to that of transporters could be examined as another model parameter.

5.2.4 The effect of the DA auto-receptor activation on the DA release and reuptake process

The D2 auto-receptors, located on DAT expressing cells, regulate three mechanisms on DA neurons (Ford, 2014): inhibition of DA release by blocking the activity of voltage-gated calcium channels, increasing the DAT activity, and reducing the synthesis of the DA molecules. A previous study used the effect of the D2-autoreceptor activation as a regulator of DA release probability by an action potential (Dreyer & Hounsgaard, 2013). A simple implementation of D2 receptors is the addition of explicit D2 autoreceptors with a uniform distribution on DA releasing neurons. From the number of activated D2 auto-receptors, the release rate could be increased. A more realistic implementation is an explicit definition of α-, β- and ɣ-subunits and interacting molecules. Like the AMPH-induced DA efflux model, the signaling molecules that interact with D2 autoreceptors need to be included in the model. It could increase the number of molecules in the spatial model. The computational cost is exponentially correlated to the number of molecules. Hence, it may not be plausible to simulate it with an explicit definition of receptors. A simplified scheme can be implemented using a similar strategy that is used to calculate the relation between intracellular AMPH concentration and the rate of phosphorylation. The relation between D2 auto-receptor

activity and DA release, DA synthesis, and DAT activity can be estimated. All the rate constants are modified based on the amount of D2 auto-receptor activity at a given time.

5.2.5 Signaling molecules can change the outcome of the AMPH-induced DA efflux model

In the current AMPH-induced DA efflux model, the only diffusion limited interaction is the diffusion of the AMPH inside the cell. However, AMPH can interact with various signaling molecules such as Rho, TAAR1, and CaMKII which eventually phosphorylate DAT or trigger the endocytosis of DAT. Depending on the concentrations of these signaling molecules, immobile and uniformly distributed molecules can be used in simulations. In addition to individual diffusion of AMPH molecule, some additional states that denote the previous interactions with other signaling molecules can be introduced. Because of the addition of the states related to the AMPH interactions, the DAT phosphorylation, and DAT endocytosis rates need to be re-evaluated. A more complex reaction scheme can also be implemented with the addition of more signaling molecules.

5.2.6 Proper implementation of hybrid genetic algorithm/online model checking with NFsim

NFsim does not have a proper way to stop and start simulations if the aggregate sizes are larger than 20. However, NFsim can provide an output of the model for individual time points without stopping the simulation. The model checker can decide to terminate or continue a trajectory without stopping the simulation engine. Due to the asynchronous nature of stochastic simulations, all runs have a different trajectory, and it takes different CPU-time to reach same time points in

the simulation. Instead of stopping a simulation and waiting for other repeats to reach the same simulation time, all the simulations are kept running until they reach a time point with pre-defined logic. When the last repeat reaches the time point with pre-defined logic, the termination criterion for the parameter set is evaluated. Depending on the logic evaluation, the model checker makes the decision to terminate or proceed with the other simulations, which reduces the amount of CPU-time that is required to generate individual trajectories.

5.2.7 Spatial modeling of CaMKII dynamics

CaMKII is activated in the post-synaptic cells of the glutamatergic synapses. A detailed spatial model of the glutamatergic synapses and ionotropic glutamate receptor activation was developed in a previous study (Bartol, Keller, et al., 2015). This model has a simplified scheme for CaMKII kinetics where each CaMKII is assumed as a monomer. If the model calibration for activation-triggered subunit exchange mechanism is completed, a comprehensive model of the glutamatergic signaling starting from action potential to CaMKII activation could be built. This model would provide a mechanistic description of multiple components of the computational model such as voltage-gated calcium channels, activation of glutamate release by synaptotagmin, AMPA receptors, NMDA receptors, CaM and CaMKII. With the implementation of network-free simulations in MCell algorithm, the elaborate kinetic scheme that is described in Chapter 4.0 could be simulated in a spatial setting. Since the size of the postsynaptic synapse is one order of magnitude smaller than the simulation box that is described in Chapter 2.0, it may be possible to simulate the glutamatergic synapse model with MCell efficiently. Therefore, more extended simulations could be performed to investigate the sustained activity of CaMKII associated with memory formation.

APPENDIX A CELL SIMULATIONS

In this chapter, I describe how I built the spatially realistic model of DA signaling in the model description language (MDL) that is used as input to the MCell simulator. The MDL syntax and file modules created are explained in detail.

A.1 ANATOMY OF AN MCELL MODEL

There are 12 different modules that describe a spatial model in MCell. All 10 modules are imported in the main file, and all modules are simulated. The main file includes all the modules and additional specifications of the model. All those modules are explained in detail below:

A.1.1 Simulation specifications and main file

The main file includes the general information for the simulation, and the main file is divided into four different sections. The first section is the definition of the simulation parameters. Some example simulation parameters that need to be specified in the main file are the time step, the number of iterations and the seed number for random number generation. This first block also includes information related to simulation optimization through partitioning and checkpointing if defined. Partitioning reduces the total number of collision detection and speeds up the simulation. Checkpointing is a useful feature to use for long simulations. These parameters are defined in the following syntax:

```
ITERATIONS = 10000000
TIME_STEP = 1e-06
```

The second section is the definition of the mesh objects in the simulation system. All these objects are instantiated in this block. This block starts with an instantiate command followed by the name of the objects used in the model. The syntax for this block is the following:

```
INSTANTIATE Scene OBJECT
{
axon1 OBJECT axon1 {}
axon10 OBJECT axon10 {}
}
```

The third section in the main file is the definition of the molecule placements. Each release site is defined in this block. In the same block with the definition of the mesh objects, the release sites are also defined. An example of a release sire definition is given in the following:

```
rel_axon1_datall RELEASE_SITE
{
SHAPE = Scene.axon1[DAT_all]
MOLECULE = DATo'
DENSITY = 800
RELEASE_PROBABILITY = 1
}
```

The name of the release site is given as ‘rel_axon1_datall’ which contains the information related to how DAT placed on a surface based on given information. ‘SHAPE’ argument shows the surface that the molecules located. ‘MOLECULE’ describes the type and the orientation of the molecule. There are three different orientation definition exists in MCell. The outward facing molecules are defined with “’” sign, inward-facing molecules are defined with “,” and the orientation ignored molecules are defined with “;” sign. In our case, DAT molecules are in outward facing orientation. For surface molecules, the density arguments show the surface density in

several molecules per μm^2. Release probability argument can be used for molecules that can be placed with a probability. In our case, all DATs are placed with release probability of 1. All regions that are determined from fluorescence images are tagged in the geometry files, and the release sites are identified from the definition of the site. For volume molecules, the release site information can be included in a different form:

```
DA_release5 RELEASE_SITE
{
SHAPE = Scene.rel4
MOLECULE = DA
NUMBER_TO_RELEASE = 3250
RELEASE_PROBABILITY = 1
RELEASE_PATTERN = DA_release5
}
```

The shape is defined as the name of the object that DA molecules are released. In this model, rel4 object is a sphere with 0.01 μm diameter with all transparent surfaces to DA molecules. Similarly, all six DA active zone have the same diameter and surface properties. These objects act as a point source for DA release. The last parameter "release pattern" is an explicitly defined set of values that describe properties of a release event. These parameters are explained in detail below.

The last section of the main MCell file is the inclusion of the other modules of the model. An example of module inclusion is given in the following:

```
INCLUDE_FILE = "Scene.molecules.mdl"
INCLUDE_FILE = "Scene.surface_classes.mdl"
```

The definitions and descriptions in included files are added to the main simulation file at runtime.

A.1.2 Simulation environment and geometry

The second component of the MCell model is the geometry definition. The geometry definition includes the information about the vertices, edges, and surfaces. An example description of the geometry file is the following:

```
Cube POLYGON_LIST
{
 VERTEX_LIST
 {
  [ 5.10000228881836, 5.10000228881836, -2.2518424987793 ]
  [ 5.10000228881836, 5.10000228881836, 5.34815740585327 ]
                                .
                                .
                                .



 ELEMENT_CONNECTIONS
 {
  [ 3, 0, 2 ]
  [ 7, 2, 6 ]
  [ 5, 6, 4 ]
  [ 1, 4, 0 ]

          .
          .
          .


DEFINE_SURFACE_REGIONS
 {
  DAT1
  {
   ELEMENT_LIST = [4843, 4911, 4980, 4981, 5036, 5168, 5239, 5243, 5287, 5358, 5402,
5455, 5461, 5462, 5465, 5504, 5510, 5511, 11590, 11733, 11802,
  }
}
```

"Cube" is the name of the simulation box in the geometry file. In "VERTEX_LIST" block, the cartesian coordinates of individual vertices are connected. In MCell, the coordinates and the

index of an individual vertex are stored. In “ELEMENT_CONNECTIONS” block, the vertices that create triangles faces are reported. MCell also stores the index of a triangle and the indices of the vertices of the triangle. Finally, in “DEFINE_SURFACE_REGIONS” block, the name of the surface region and the indices of the triangles that define that surface. The geometry is defined using fluorescence images, and the extracellular geometry is imported to Blender. All surfaces are triangulated using built-in functions in Blender, and the regions are identified using Blender interface. Finally, the geometry files are exported by “Cell Blender” , a special purpose add-on to create and simulate MCell models.

A.1.3 Parameters

The third module of an MCell file is the parameter block. All simulation parameters can be defined in any module. However, it is cleaner to define all the model parameters in a single parameter block for readability purposes. The parameter definitions are given in the following format:

```
large_dat = 0.00000
small_dat = 800.000000
```

A.1.4 Molecules

The fourth module is used to define the properties of the molecules. The two main properties of a molecule are the name and the diffusion constant of a molecule. The molecules are defined in the following way:

```
DEFINE_MOLECULES
{
 DA
 {
  DIFFUSION_CONSTANT_3D = 4e-06
 }
 DATi
 {
  DIFFUSION_CONSTANT_2D = 0
  CUSTOM_TIME_STEP = 1e-04
 }
}
```

The block starts with 'DEFINE_MOLECULES' command, and for any molecule, name and the diffusion constants are specified. If required, custom time or diffusion step may be defined to optimize the simulation. For example, inward-facing DAT molecules (DATi) have transition rates of 8.33 s^{-1} and 20 s^{-1} . Therefore, it is not required to calculate the propensity of the reactions of the DAT every time step and the custom time step specifies the time intervals the DATi transition propensities are calculated.

A.1.5 Reactions

The fifth module is the block that the reactions are specified. In MCell reactions, reactants and products with orientations and rate constants need to be identified. An example of a reaction is the following:

```
DEFINE_REACTIONS
{
 DA' + DATo' -> DA_DATo' [>9.6e+07] : r1
}
```

In the example reaction above, DA molecule on the outward facing side of the membrane and outward facing DAT on the outward facing side of the membrane reacted to produce a DA,

DAT complex which is also in the outward facing orientation. The term in square brackets shows the directionality of the reaction and the rate constant. Finally, the name of the reaction is defined. Reaction names are also useful in MCell simulations since it is possible to track how many times a reaction triggered.

A.1.6 Surface classes

The sixth module is the definition of the definition of the properties of specific surface regions. The transparency of a surface for a specific type of molecule is defined in this module. An example surface definition is the following:

```
DEFINE_SURFACE_CLASSES
{
  DA_trans
  {
    TRANSPARENT = DA;
  }
}
```

The surface class defined in the snippet is 'DA_trans' which modifies surfaces that are transparent to DA molecules. The absorptive, reflective or transparent properties of the surfaces are defined using this module.

A.1.7 Surface modifications

The seventh module is the block that the defined surface classes are assigned to surface regions. In "MODIFY_SURFACE_REGION" block, the specified region of a mesh object is assigned to a predefined surface class. As described below, all point sources that used for DA release are spherical objects with transparent DA surfaces. The assignment is given in the following:

```
MODIFY_SURFACE_REGIONS
{
  rel6[region]
  {
    SURFACE_CLASS = DA_trans
  }
}
```

"rel6" is the release site around the sixth active zone. The triangle that created this mesh object names as "region". Since the "region" part of the mesh object assigned as "DA_trans", this region is transparent to DA molecules.

A.1.8 Release patterns

The eighth module is the block that the release patterns are identified. In MCell, there are a large variety of release patterns. It is possible to set a specific time for a release or define a periodic release with specific release durations and frequencies. A simple DA release event is given below:

```
DEFINE_RELEASE_PATTERN DA_release3
{
DELAY = 8.016
RELEASE_INTERVAL = 1e-6
TRAIN_DURATION = 1e-6
TRAIN_INTERVAL = 1e-6
NUMBER_OF_TRAINS = 1
}
```

The release pattern DA_release3 is defined in the given block. The first parameter "DELAY" means that the DA release event occurs at 8.016 seconds after the simulation is started. Since this is an instant release, "RELEASE_INTERVAL" needs to be set to a smaller value than the time step of the simulation. The other parameters are used to define periodic release events which I do not use in dopaminergic signaling model.

A.1.9 Model outputs

The ninth and tenth modules are the blocks where the reaction output and the visualization outputs are specified. An example reaction output is given in the following:

```
REACTION_DATA_OUTPUT
{
 OUTPUT_BUFFER_SIZE = 1000
 STEP=1e-04
 {COUNT[DA,WORLD]}=> "./react_data/seed_" & seed & "/DA.World.dat"
 {COUNT[r1,WORLD]}=> "./react_data/seed_" & seed & "/r1.World.dat"
}
```

"OUTPUT BUFFER SIZE" argument specifies how often MCell dumps the reaction output to specified file. "STEP" argument defines the time interval that the reaction outputs are stored. For instance, MCell stores reaction output every 100 μs but it only writes the output to a file at every 10 ms. The "COUNT" command counts the specified molecule in each compartment. In MCell simulation, "WORLD" is defined as an infinitely large simulation box, and everything in the system is counted. The count output is written on the specified file in the right-hand side of the count statement. An example visualization output is given in the following:

```
VIZ_OUTPUT
{
 FILENAME = "./viz_data/seed_" & seed & "/Scene"
 MOLECULES
 {
  NAME_LIST {ALL_MOLECULES}
  ITERATION_NUMBERS {ALL_DATA @ [[0 TO 100000 STEP 1000]]}
}
```

In the block above, a file name is defined to output the location of individual molecules in the MCell simulation. The molecules should be specified as an argument to "NAME_LIST" block, and the output frequency and the length can be defined in "ITERATION_NUMBERS" block.

The final block is the initialization block of MCell simulations. This section includes various parameters about the properties of the simulator. All the warnings and notifications that MCell creates throughout the simulation is defined in this block. A detailed description of the initialization parameters is provided in MCell quick reference guide. For our model, the surface grid density parameter set to 10000 μm^{-2} to enable MCell to have dense clusters of DAT. An example MCell model of DA signaling is available at https://github.com/cihankayacihan/dopamine_striatum_mcell.git

APPENDIX B BIONETGEN MODEL OF ACTIVATION-TRIGGERED SUBUNIT EXCHANGE OF CAMKII

Similar to MCell models, models that are described in BioNetGen Language (BNGL) are composed of different parts. A BNGL file consists of at least seven different parts. I will explain these seven parts for the activation triggered exchange model.

B.1 PARAMETERS

The first part of a BNGL model is the parameter block. An example of a parameter block is given in the following:

```
begin parameters
Nav             6e23
Vol                     2e-14
CaM_in_conc 5e-6
CaM_in          CaM_in_conc*Nav*Vol # count
end parameters
```

After the “begin parameters” line, each parameter is defined. The variable definitions do not have an equal sign as in MCell models. Instead, any white space character on the same line set the parameters. In BNGL, parameters do not have defined units. Therefore, the modeler needs to take care of all unit conversion and conservations. Finally, it is possible to define parameters from the other parameters defined in the block. For instance, the parameter “CaM_in” which is the

number of calmodulin (CaM) molecules at the beginning of the simulations is defined using three other parameters: Avogadro's number "Nav", the volume of interest "Vol", and the initial concentration of the CaM "CaM_in_conc". All constant parameters such as forward and backward rate constants, half-max concentration, and forward rate for Michaelis-Menten kinetics and Hill coefficients are defined in this block. All blocks are finished with an "end" statement in BNGL.

B.2 MOLECULE TYPES

The second block is the molecule type definition block. The following shows the definition of molecule types in BNGL.

```
begin molecule types
        Ca(cam)
        CaM(ca,ca,ca,ca,camk)
        CaMK(cam,t286~u~p,t305~u~p,camk6left,camk6right,vert,color~red~green)
end molecule types
```

The molecule names, binding sites, and states need to be defined in molecule types block. The first example in this block is the calcium molecule "Ca". Calcium molecules can only bind to CaM molecule, and this binding site is denoted as "cam". The second molecule type "CaM" has multiple binding sites. First, "CaM" has four identical calcium binding sites that are denoted as "ca". In addition, an activated CaM molecule can bind to a CaMKII subunit. For this purpose, the binding site "camk" is added. The CaMKII subunit is the most complicated molecule type in this model. Since CaMKII is activated by CaM molecules, it needs to have a binding site for CaM "cam". It also has two phosphorylation sites named as "t286" and "t305". The unphosphorylated states and phosphorylated states at these two sites are denoted with "u" and "p", respectively. The "~" notation enables the user to define all possible values for a given state definition. The ring

structure in CaMKII holoenzyme is composed of individual subunits. Each CaMKII subunit has a connection with its counter-clockwise and clockwise neighbor. These two connections are denoted as binding with two CaMKII subunit. Each subunit has a “camk6left” and a “camk6right” binding site. In addition, two hexamer rings create the dodecamer holoenzyme. Therefore, a subunit at the bottom ring needs to be connected to a specific subunit on the top ring. These subunits are also connected through binding at “vert” binding site. Finally, in the colocalization experiment, each CaMKII subunit has a fluorescence color, which could be red or green. These states are defined in molecule type definitions.

B.3 INITIALIZATION

The third block of the BNGL model is the block that specifies the number of all species at the beginning of the simulation. The “seed species” block is defined as the following:

```
begin seed species
    Ca(cam)         Ca_in
    CaM(ca,ca,ca,ca,camk) CaM_in
    CaMK(cam,t286~u,t305~u,camk6left!1,camk6right!2,vert!13,color~red).CaMK(cam,t28
6~u,t305~u,camk6left!2,camk6right!3,vert!14,color~red).CaMK(cam,t286~u,t305~u,camk6left!
3,camk6right!4,vert!15,color~red).CaMK(cam,t286~u,t305~u,camk6left!4,camk6right!5,vert!16,
color~red).CaMK(cam,t286~u,t305~u,camk6left!5,camk6right!6,vert!17,color~red).CaMK(cam,
t286~u,t305~u,camk6left!6,camk6right!1,vert!18,color~red).CaMK(cam,t286~u,t305~u,camk6le
ft!7,camk6right!8,vert!13,color~red).CaMK(cam,t286~u,t305~u,camk6left!8,camk6right!9,vert!
14,color~red).CaMK(cam,t286~u,t305~u,camk6left!9,camk6right!10,vert!15,color~red).CaMK(
cam,t286~u,t305~u,camk6left!10,camk6right!11,vert!16,color~red).CaMK(cam,t286~u,t305~u,c
amk6left!11,camk6right!12,vert!17,color~red).CaMK(cam,t286~u,t305~u,camk6left!12,camk6ri
ght!7,vert!18,color~red) CaMK12_in_red
    CaMK(cam,t286~u,t305~u,camk6left!1,camk6right!2,vert!13,color~green).CaMK(cam,t
286~u,t305~u,camk6left!2,camk6right!3,vert!14,color~green).CaMK(cam,t286~u,t305~u,camk6
left!3,camk6right!4,vert!15,color~green).CaMK(cam,t286~u,t305~u,camk6left!4,camk6right!5,v
ert!16,color~green).CaMK(cam,t286~u,t305~u,camk6left!5,camk6right!6,vert!17,color~green).
CaMK(cam,t286~u,t305~u,camk6left!6,camk6right!1,vert!18,color~green).CaMK(cam,t286~u,t
305~u,camk6left!7,camk6right!8,vert!13,color~green).CaMK(cam,t286~u,t305~u,camk6left!8,c
amk6right!9,vert!14,color~green).CaMK(cam,t286~u,t305~u,camk6left!9,camk6right!10,vert!15
,color~green).CaMK(cam,t286~u,t305~u,camk6left!10,camk6right!11,vert!16,color~green).Ca
MK(cam,t286~u,t305~u,camk6left!11,camk6right!12,vert!17,color~green).CaMK(cam,t286~u,t
305~u,camk6left!12,camk6right!7,vert!18,color~green) CaMK12_in_green
    CaMK(cam,t286~u,t305~u,camk6left!1,camk6right!2,vert!15,color~red).CaMK(cam,t28
6~u,t305~u,camk6left!2,camk6right!3,vert!16,color~red).CaMK(cam,t286~u,t305~u,camk6left!
3,camk6right!4,vert!17,color~red).CaMK(cam,t286~u,t305~u,camk6left!4,camk6right!5,vert!18,
color~red).CaMK(cam,t286~u,t305~u,camk6left!5,camk6right!6,vert!19,color~red).CaMK(cam,
t286~u,t305~u,camk6left!6,camk6right!7,vert!20,color~red).CaMK(cam,t286~u,t305~u,camk6le
ft!7,camk6right!1,vert!21,color~red).CaMK(cam,t286~u,t305~u,camk6left!8,camk6right!9,vert!
15,color~red).CaMK(cam,t286~u,t305~u,camk6left!9,camk6right!10,vert!16,color~red).CaMK(
cam,t286~u,t305~u,camk6left!10,camk6right!11,vert!17,color~red).CaMK(cam,t286~u,t305~u,c
amk6left!11,camk6right!12,vert!18,color~red).CaMK(cam,t286~u,t305~u,camk6left!12,camk6ri
ght!13,vert!19,color~red).CaMK(cam,t286~u,t305~u,camk6left!13,camk6right!14,vert!20,color
~red).CaMK(cam,t286~u,t305~u,camk6left!14,camk6right!8,vert!21,color~red)
CaMK14_in_red
    CaMK(cam,t286~u,t305~u,camk6left!1,camk6right!2,vert!15,color~green).CaMK(cam,t
286~u,t305~u,camk6left!2,camk6right!3,vert!16,color~green).CaMK(cam,t286~u,t305~u,camk6
left!3,camk6right!4,vert!17,color~green).CaMK(cam,t286~u,t305~u,camk6left!4,camk6right!5,v
ert!18,color~green).CaMK(cam,t286~u,t305~u,camk6left!5,camk6right!6,vert!19,color~green).
CaMK(cam,t286~u,t305~u,camk6left!6,camk6right!7,vert!20,color~green).CaMK(cam,t286~u,t
305~u,camk6left!7,camk6right!1,vert!21,color~green).CaMK(cam,t286~u,t305~u,camk6left!8,c
amk6right!9,vert!15,color~green).CaMK(cam,t286~u,t305~u,camk6left!9,camk6right!10,vert!16
,color~green).CaMK(cam,t286~u,t305~u,camk6left!10,camk6right!11,vert!17,color~green).Ca
MK(cam,t286~u,t305~u,camk6left!11,camk6right!12,vert!18,color~green).CaMK(cam,t286~u,t
305~u,camk6left!12,camk6right!13,vert!19,color~green).CaMK(cam,t286~u,t305~u,camk6left!1
```

The first and second species are the calcium and CaM species which do not have any connections or states at the beginning of the simulations. However, CaMKII subunits form

dodecamer through multiple connections. In the beginning, all CaMKII subunits are in the unphosphorylated state and CaM-free. The ring structure is formed using binding between individual subunits. The numbers after "!" means the tag of the bond. Using these tags, the interactions among subunits are defined. For instance, the connection "1" defines the connection between the "camk6left" of the first subunit on the top ring, with "camk6right" of the sixth subunit on the top ring. Using the same methodology, a ring is created. Similarly, the connections between the top and bottom subunits are also constructed. For instance, connection "13" is the vertical binding between the first subunit on the top and bottom rings. Finally, the red and green tags of the CaMKII subunits are also defined in this state.

B.4 OBSERVABLES

The next block is the definition of the observables block. The observables are defined as the counts of the given molecules or species. An example observable block is given in the following:

```
begin observables
        Molecules Duu CaMK(cam,t286~u,t305~u)
        Molecules Cu CaMK(cam!+,t286~u,t305~u)
        Molecules CaMK_tot CaMK()
        Species colocal CaMK(color~red).CaMK(color~green)
end observables
```

The syntax in the observable block includes three levels. First, the type of observable needs to be defined. "Molecules" argument is used to count individual molecule types whereas, "Species" argument is used to count species that has a specific pattern. The first observable in the block given above is the count of the CaMKII subunits in the CaM unbound and double unphosphorylated state (D_{uu}). The second state is the CaM bound and the double unphosphorylated state. In the observables block, it is not required to add any additional context that is not related

to the observable. For example, in the first two observable definitions, the state "color" or intermolecular binding among CaMKII subunits are not specified. It is also possible to count all molecule types, regardless of the binding or phosphorylation state. In the third observable, the count of all CaMKII subunits is calculated. Finally, the "Species" argument is used to find species with at least one subunit where the color is in state "red", and another subunit where the color is in "green" state. This value is used to calculate colocalization.

B.5 FUNCTIONS

The fifth block in BNGL is the definition of the functions. The functions block is used to calculate observable dependent parameters. An example function definition in BNGL model is given in the following:

```
begin functions
        P_rate() = kcat * pp1a / (Km + Cp + Dpu + Dpp + Dpp)
        Phospho() = (Cp + Dpu + Dpp) / CaMK_tot
end functions
```

The first reaction definition in the block is the phosphorylation rate constant. It follows the Michaelis-Menten kinetics. The "kcat" and "Km" are defined in the parameter block. Other values "pp1a" is the count of the phosphatase molecules, and "Cp","Dpu", and "Dpp" are the different states of the CaMKII subunits. The double occurrence of "Dpp" in the formula is because the phosphorylation rate constant is inversely proportional to a total number of phosphorylation sites instead of phosphorylated molecules. In the second function, the ratio of the phosphorylated CaMKII subunits is determined.

B.6 REACTION RULES

The sixth and arguably the most critical block of a BNGL model is the reaction rules block. Rules are local definitions of reactions. A couple of example rule definitions are given in the following:

```
begin reaction rules
# CaM binding to unphosphorylated CaMKII
R5 : CaMK(cam,t286~u,t305~u,camk6left!+,camk6right!+) + CaM(camk) <->
CaMK(cam!5,t286~u,t305~u,camk6left!+,camk6right!+).CaM(camk!5) kon_u,koff_u
# T286 phosphorylation of Cu by Cp
R13 :
CaMK(cam!5,t286~u,t305~u,camk6left!1).CaM(camk!5).CaMK(cam!4,t286~p,t305~u,camk6right!1).CaM
(camk!4) -> \
CaMK(cam!5,t286~p,t305~u,camk6left!1).CaM(camk!5).CaMK(cam!4,t286~p,t305~u,camk6right!1).CaM
(camk!4) r2
R92 : CaMK(t286~p) -> CaMK(t286~u) P_rate()
end reaction rules
```

The rule syntax has four parts. The first part is the definition of the reactants. Instead of defining complete reactant, the only required part for the reaction context needs to be defined. For example, CAM can only bind to CaMKII if the "cam" binding site is not occupied. Also, the binding rates of CaMKII are different depending on the phosphorylation state at "t286" and "t305". Therefore, it is required to describe the context of the reaction in the reactants. The second part of the reaction rule is the directionality part of the reactions. Since CaM binding/unbinding is an equilibrium reaction, "<->" needs to be used. The third part is the definition of the product part. The species of multiple molecules are created with "." notation. Basically, a species can be constructed by concatenating a lot of molecules with a "." sign between them. The "+" sign after "!" means that the site needs to be occupied regardless of the molecule. More specifically, the addition of binding partner requirement at "camk6left" and "camk6right" binding sites avoid CaM binding to vertical dimers resulted from subunit exchange mechanism. The second rule is more complicated because it is the definition of a state change of a molecule based on the structure of

the molecule. The first CaMKII subunit has a bound CaM, and both phosphorylation sites are in the unphosphorylated state. The neighboring CaMKII subunit also has a CaM, and "t286" site is phosphorylated. Therefore, the second subunit can phosphorylate the "t286" site of the first subunit with the rate of "r2". The rule-based modeling enables us to define this type of complex reactions with a single rule without even defining whole species. In the last rule, the dephosphorylation rate of the CaMKII is used as a function that is defined in the "functions" block. The dephosphorylation events are completely independent of context and can happen if a "t286" is in a phosphorylated state.

B.7 MODEL EXECUTION

The final block of the model is the part that the actions on the model are defined.

```
begin actions
simulate({method=>"nf",t_end=>6,n_steps=>600,print_functions=>1,gml=>5000000})
end actions
```

All the actions that are applied to the model with specifications are defined in the "actions" block. In conventional rule-based model simulations, first a network is generated or loaded from a file, and secondly, a simulate method is used to generate trajectories. However, since NFsim is used in this model, it is possible to use a "simulate" command directly. The command "simulate", has many arguments, but in the given example the arguments are the following: (i) "method" defines the simulation method that is used for generating trajectories. In this case, the selection is defined as "nf" and NFsim simulation engine is called. (ii) "t_end" defines the end of the simulation. In this case, the system is simulated for 6 seconds. (iii) "n_steps" defines the number of times the observables and functions are dumped into a trajectory file. By specifying it as 600, simulation

engine output observables every 0.01 seconds. (iv) “print_functions” is a flag that is used to choose function outputs at each time point. (v) “gml” is the global molecule limit which used to specify the maximum number of molecules in the simulation. To have models with many molecules, that value needs to be set to a large value. The complete model of activation-triggered subunit exchange is provided in the following repository: https://github.com/cihankayacihan/camkii_bng.git

BIBLIOGRAPHY

Amara, S. G., & Sonders, M. S. (1998). *Neurotransmitter transporters as molecular targets for addictive drugs*. Paper presented at the Drug Alcohol Depend

Drug and alcohol dependence. http://www.ncbi.nlm.nih.gov/pubmed/9716932

Bai, J., Blot, K., Tzavara, E., Nosten-Bertrand, M., Giros, B., & Otani, S. (2014). Inhibition of dopamine transporter activity impairs synaptic depression in rat prefrontal cortex through over-stimulation of D1 receptors. *Cereb Cortex, 24*(4), 945-955. doi:10.1093/cercor/bhs376

Ballnus, B., Schaper, S., Theis, F. J., & Hasenauer, J. (2018). Bayesian parameter estimation for biochemical reaction networks using region-based adaptive parallel tempering. *Bioinformatics, 34*(13), i494-i501. doi:10.1093/bioinformatics/bty229

Bannon, M. J., Michaud, R. L., & Roth, R. H. (1981). Mesocortical dopamine neurons. Lack of autoreceptors modulating dopamine synthesis. *Mol Pharmacol, 19*(2), 270-275.

Bartol, T. M., Bromer, C., Kinney, J., Chirillo, M. A., Bourne, J. N., Harris, K. M., & Sejnowski, T. J. (2015). Nanoconnectomic upper bound on the variability of synaptic plasticity. *eLife, 4*, e10778. doi:10.7554/eLife.10778

Bartol, T. M., Keller, D. X., Kinney, J. P., Bajaj, C. L., Harris, K. M., Sejnowski, T. J., & Kennedy, M. B. (2015). Computational reconstitution of spine calcium transients from individual proteins. *Front Synaptic Neurosci, 7*, 17. doi:10.3389/fnsyn.2015.00017

Beckstead, M. J., Ford, C. P., Phillips, P. E., & Williams, J. T. (2007). Presynaptic regulation of dendrodendritic dopamine transmission. *Eur J Neurosci, 26*(6), 1479-1488. doi:10.1111/j.1460-9568.2007.05775.x

Bennett, M. K., Erondu, N. E., & Kennedy, M. B. (1983). Purification and characterization of a calmodulin-dependent protein kinase that is highly concentrated in brain. *J Biol Chem, 258*(20), 12735-12744.

Beuming, T., Kniazeff, J., Bergmann, M. L., Shi, L., Gracia, L., Raniszewska, K., . . . Gether, U. (2008). The binding sites for cocaine and dopamine in the dopamine transporter overlap. *Nat. Neurosci, 11*(7), 780-789.

Bhattacharyya, M., Stratton, M. M., Going, C. C., McSpadden, E. D., Huang, Y., Susa, A. C., . . . Kuriyan, J. (2016). Molecular mechanism of activation-triggered subunit exchange in Ca(2+)/calmodulin-dependent protein kinase II. *eLife, 5*. doi:10.7554/eLife.13405

Blinov, M. L., Faeder, J. R., Goldstein, B., & Hlavacek, W. S. (2004). BioNetGen: software for rule-based modeling of signal transduction based on the interactions of molecular domains. *Bioinformatics, 20*(17), 3289-3291. doi:10.1093/bioinformatics/bth378

Block, E. R., Nuttle, J., Balcita-Pedicino, J. J., Caltagarone, J., Watkins, S. C., Sesack, S. R., & Sorkin, A. (2015). Brain Region-Specific Trafficking of the Dopamine Transporter. *J Neurosci, 35*(37), 12845-12858. doi:10.1523/JNEUROSCI.1391-15.2015

Bradshaw, J. M., Kubota, Y., Meyer, T., & Schulman, H. (2003). An ultrasensitive Ca2+/calmodulin-dependent protein kinase II-protein phosphatase 1 switch facilitates specificity in postsynaptic calcium signaling. *Proc Natl Acad Sci U S A, 100*(18), 10512-10517. doi:10.1073/pnas.1932759100

Cadet, J. L., Jayanthi, S., McCoy, M. T., Beauvais, G., & Cai, N. S. (2010). Dopamine D1 receptors, regulation of gene expression in the brain, and neurodegeneration. *CNS Neurol Disord Drug Targets, 9*(5), 526-538.

Caltagarone, J., Ma, S., & Sorkin, A. (2015). Dopamine transporter is enriched in filopodia and induces filopodia formation. *Mol Cell Neurosci, 68*, 120-130. doi:10.1016/j.mcn.2015.04.005

Canavier, C. C., & Landry, R. S. (2006). An increase in AMPA and a decrease in SK conductance increase burst firing by different mechanisms in a model of a dopamine neuron in vivo. *J Neurophysiol, 96*(5), 2549-2563. doi:10.1152/jn.00704.2006

Casado, V., Ferrada, C., Bonaventura, J., Gracia, E., Mallol, J., Canela, E. I., . . . Franco, R. (2009). Useful pharmacological parameters for G-protein-coupled receptor homodimers obtained from competition experiments. Agonist-antagonist binding modulation. *Biochem Pharmacol, 78*(12), 1456-1463. doi:10.1016/j.bcp.2009.07.012

Chao, L. H., Pellicena, P., Deindl, S., Barclay, L. A., Schulman, H., & Kuriyan, J. (2010). Intersubunit capture of regulatory segments is a component of cooperative CaMKII activation. *Nat Struct Mol Biol, 17*(3), 264-272. doi:10.1038/nsmb.1751

Cheng, M. H., & Bahar, I. (2015). Molecular mechanism of dopamine transport by human dopamine transporter. *Structure, 23*(11), 2171-2181.

Cheng, M. H., Block, E., Hu, F., Cobanoglu, M. C., Sorkin, A., & Bahar, I. (2015). Insights into the modulation of dopamine transporter function by amphetamine, orphenadrine and cocaine binding. *Front. Neurol, 6*, 134. doi:10.3389/fneur.2015.00134

Cheng, M. H., Garcia-Olivares, J., Wasserman, S., DiPietro, J., & Bahar, I. (2017). Allosteric Modulation of Human Dopamine Transporter Activity under Conditions Promoting its Dimerization. *J. Biol. Chem, 292*, 12471-12482.

Cheng, M. H., Kaya, C., & Bahar, I. (2018). Quantitative Assessment of the Energetics of Dopamine Translocation by Human Dopamine Transporter. *J Phys Chem B, 122*(21), 5336-5346. doi:10.1021/acs.jpcb.7b10340

Cheng, M. H., Torres-Salazar, D., Gonzalez-Suarez, A. D., Amara, S. G., & Bahar, I. (2017). Substrate transport and anion permeation proceed through distinct pathways in glutamate transporters. *eLife, 6*, e25850.

Chiba, H., Schneider, N. S., Matsuoka, S., & Noma, A. (2008). A simulation study on the activation of cardiac CaMKII delta-isoform and its regulation by phosphatases. *Biophys J, 95*(5), 2139-2149. doi:10.1529/biophysj.107.118505

Chipot, C., & Hénin, J. (2005). Exploring the free-energy landscape of a short peptide using an average force. *J. Chem. Phys, 123*, 244906.

Churchland, P. S., & Sejnowski, T. J. (2016). *The computational brain*: MIT press.

Colbran, R. J. (1993). Inactivation of Ca2+/calmodulin-dependent protein kinase II by basal autophosphorylation. *J Biol Chem, 268*(10), 7163-7170.

Coleman, J. A., Green, E. M., & Gouaux, E. (2016). X-ray structures and mechanism of the human serotonin transporter. *Nature, 532*(7599), 334-339. doi:10.1038/nature17629

Cosgrove, K. P. (2010). Imaging receptor changes in human drug abusers. *Curr Top Behav Neurosci, 3*, 199-217. doi:10.1007/7854_2009_24

Council, N. R. (1993). In D. R. Gerstein & L. W. Green (Eds.), *Preventing Drug Abuse: What do we know?* Washington (DC): National Academic Press.

Cragg, S. J., Nicholson, C., Kume-Kick, J., Tao, L., & Rice, M. E. (2001). Dopamine-mediated volume transmission in midbrain is regulated by distinct extracellular geometry and uptake. *J Neurophysiol, 85*(4), 1761-1771. doi:10.1152/jn.2001.85.4.1761

Cragg, S. J., & Rice, M. E. (2004). DAncing past the DAT at a DA synapse. *Trends Neurosci, 27*(5), 270-277. doi:10.1016/j.tins.2004.03.011

Czech, J., Dittrich, M., & Stiles, J. R. (2009). Rapid creation, Monte Carlo simulation, and visualization of realistic 3D cell models. *Methods Mol Biol, 500*, 237-287. doi:10.1007/978-1-59745-525-1_9

Dagher, A., & Robbins, T. W. (2009). Personality, addiction, dopamine: insights from Parkinson's disease. *Neuron, 61*(4), 502-510. doi:10.1016/j.neuron.2009.01.031

Danbolt, N. C. (2001). Glutamate uptake. *Prog Neurobiol, 65*(1), 1-105.

Dar, D. E., Metzger, T. G., Vandenbergh, D. J., & Uhl, G. R. (2006). Dopamine uptake and cocaine binding mechanisms: The involvement of charged amino acids from the transmembrane domains of the human dopamine transporter. *Eur. J. Pharm, 538*(1), 43-47.

De Koninck, P., & Schulman, H. (1998). Sensitivity of CaM kinase II to the frequency of Ca2+ oscillations. *Science, 279*(5348), 227-230.

Di Chiara, G., & Imperato, A. (1988). Drugs abused by humans preferentially increase synaptic dopamine concentrations in the mesolimbic system of freely moving rats. *Proc Natl Acad Sci U S A, 85*(14), 5274-5278.

Dittrich, M., Pattillo, J. M., King, J. D., Cho, S., Stiles, J. R., & Meriney, S. D. (2013). An excess-calcium-binding-site model predicts neurotransmitter release at the neuromuscular junction. *Biophys J, 104*(12), 2751-2763. doi:10.1016/j.bpj.2013.05.023

Doucet, G., Descarries, L., & Garcia, S. (1986). Quantification of the dopamine innervation in adult rat neostriatum. *Neuroscience, 19*(2), 427-445.

Dreyer, J. K., Herrik, K. F., Berg, R. W., & Hounsgaard, J. D. (2010). Influence of phasic and tonic dopamine release on receptor activation. *J Neurosci, 30*(42), 14273-14283. doi:10.1523/JNEUROSCI.1894-10.2010

Dreyer, J. K., & Hounsgaard, J. (2013). Mathematical model of dopamine autoreceptors and uptake inhibitors and their influence on tonic and phasic dopamine signaling. *J Neurophysiol, 109*(1), 171-182. doi:10.1152/jn.00502.2012

Durrant, J. D., de Oliveira, C. A., & McCammon, J. A. (2011). POVME: an algorithm for measuring binding-pocket volumes. *J Mol Graph Model, 29*(5), 773-776. doi:10.1016/j.jmgm.2010.10.007

Elgersma, Y., Fedorov, N. B., Ikonen, S., Choi, E. S., Elgersma, M., Carvalho, O. M., . . . Silva, A. J. (2002). Inhibitory autophosphorylation of CaMKII controls PSD association, plasticity, and learning. *Neuron, 36*(3), 493-505.

Erondu, N. E., & Kennedy, M. B. (1985). Regional distribution of type II Ca2+/calmodulin-dependent protein kinase in rat brain. *J Neurosci, 5*(12), 3270-3277.

Faeder, J. R. (2011). Toward a comprehensive language for biological systems. *BMC Biol, 9*, 68. doi:10.1186/1741-7007-9-68

Faeder, J. R., Blinov, M. L., & Hlavacek, W. S. (2009). Rule-based modeling of biochemical systems with BioNetGen. *Methods Mol Biol, 500*, 113-167. doi:10.1007/978-1-59745-525-1_5

Feifel, D., Shilling, P. D., Kuczenski, R., & Segal, D. S. (2003). Altered extracellular dopamine concentration in the brains of cholecystokinin-A receptor deficient rats. *Neurosci Lett, 348*(3), 147-150.

Ferris, M. J., Calipari, E. S., Mateo, Y., Melchior, J. R., Roberts, D. C., & Jones, S. R. (2012). Cocaine self-administration produces pharmacodynamic tolerance: differential effects on the potency of dopamine transporter blockers, releasers, and methylphenidate. *Neuropsychopharmacology, 37*(7), 1708-1716. doi:10.1038/npp.2012.17

Ford, C. P. (2014). The role of D2-autoreceptors in regulating dopamine neuron activity and transmission. *Neuroscience, 282*, 13-22. doi:10.1016/j.neuroscience.2014.01.025

Franken, I. H., Stam, C. J., Hendriks, V. M., & van den Brink, W. (2003). Neurophysiological evidence for abnormal cognitive processing of drug cues in heroin dependence. *Psychopharmacology (Berl), 170*(2), 205-212. doi:10.1007/s00213-003-1542-7

Franks, K. M., & Sejnowski, T. J. (2002). Complexity of calcium signaling in synaptic spines. *Bioessays, 24*(12), 1130-1144. doi:10.1002/bies.10193

Freyberg, Z., Sonders, M. S., Aguilar, J. I., Hiranita, T., Karam, C. S., Flores, J., . . . Javitch, J. A. (2016). Mechanisms of amphetamine action illuminated through optical monitoring of dopamine synaptic vesicles in Drosophila brain. *Nat Commun, 7*, 10652. doi:10.1038/ncomms10652

Garris, P. A., Ciolkowski, E. L., Pastore, P., & Wightman, R. M. (1994). Efflux of dopamine from the synaptic cleft in the nucleus accumbens of the rat brain. *J Neurosci, 14*(10), 6084-6093.

Gether, U., Andersen, P. H., Larsson, O. M., & Schousboe, A. (2006). Neurotransmitter transporters: molecular function of important drug targets. *Trends Pharmacol Sci, 27*(7), 375-383. doi:10.1016/j.tips.2006.05.003

Goto, Y., Otani, S., & Grace, A. A. (2007). The Yin and Yang of dopamine release: a new perspective. *Neuropharmacology, 53*(5), 583-587. doi:10.1016/j.neuropharm.2007.07.007

Gubernator, N. G., Zhang, H., Staal, R. G., Mosharov, E. V., Pereira, D. B., Yue, M., . . . Sames, D. (2009). Fluorescent false neurotransmitters visualize dopamine release from individual presynaptic terminals. *Science, 324*(5933), 1441-1444. doi:10.1126/science.1172278

Gur, M., Cheng, M. H., Zomot, E., & Bahar, I. (2017). Effect of Dimerization on the Dynamics of Neurotransmitter:Sodium Symporters. *J Phys Chem B, 121*(15), 3657-3666. doi:10.1021/acs.jpcb.6b09876

Hamelberg, D., de Oliveira, C. A., & McCammon, J. A. (2007). *Sampling of slow diffusive conformational transitions with accelerated molecular dynamics*. Paper presented at the J. Chem Phys

The Journal of chemical physics. http://www.ncbi.nlm.nih.gov/pubmed/17949218

Hanson, P. I., Meyer, T., Stryer, L., & Schulman, H. (1994). Dual role of calmodulin in autophosphorylation of multifunctional CaM kinase may underlie decoding of calcium signals. *Neuron, 12*(5), 943-956.

Herculano-Houzel, S. (2009). The human brain in numbers: a linearly scaled-up primate brain. *Front Hum Neurosci, 3*, 31. doi:10.3389/neuro.09.031.2009

Hines, M. L., & Carnevale, N. T. (1997). The NEURON simulation environment. *Neural Comput, 9*(6), 1179-1209.

Hines, M. L., Morse, T., Migliore, M., Carnevale, N. T., & Shepherd, G. M. (2004). ModelDB: A Database to Support Computational Neuroscience. *J Comput Neurosci, 17*(1), 7-11. doi:10.1023/B:JCNS.0000023869.22017.2e

Hlavacek, W. S., Faeder, J. R., Blinov, M. L., Perelson, A. S., & Goldstein, B. (2003). The complexity of complexes in signal transduction. *Biotechnol Bioeng, 84*(7), 783-794. doi:10.1002/bit.10842

Hoang, Q. Q. (2014). Pathway for Parkinson disease. *Proc Natl Acad Sci U S A, 111*(7), 2402-2403. doi:10.1073/pnas.1324284111

Hoffman, A. F., Lupica, C. R., & Gerhardt, G. A. (1998). Dopamine transporter activity in the substantia nigra and striatum assessed by high-speed chronoamperometric recordings in brain slices. *J Pharmacol Exp Ther, 287*(2), 487-496.

Huang, X., & Zhan, C. G. (2007). How dopamine transporter interacts with dopamine: insights from molecular modeling and simulation. *Biophys. J, 93*(10), 3627-3639.

ImageJ. (04/25/2016). TrakEM2 tutorials - ImageJ.

Jones, S. R., Gainetdinov, R. R., Wightman, R. M., & Caron, M. G. (1998). Mechanisms of amphetamine action revealed in mice lacking the dopamine transporter. *J Neurosci, 18*(6), 1979-1986.

Jones, S. R., Garris, P. A., & Wightman, R. M. (1995). Different effects of cocaine and nomifensine on dopamine uptake in the caudate-putamen and nucleus accumbens. *J Pharmacol Exp Ther, 274*(1), 396-403.

Jorstad, A., Nigro, B., Cali, C., Wawrzyniak, M., Fua, P., & Knott, G. (2015). NeuroMorph: a toolset for the morphometric analysis and visualization of 3D models derived from electron microscopy image stacks. *Neuroinformatics, 13*(1), 83-92. doi:10.1007/s12021-014-9242-5

Jufer, R. A., Wstadik, A., Walsh, S. L., Levine, B. S., & Cone, E. J. (2000). Elimination of cocaine and metabolites in plasma, saliva, and urine following repeated oral administration to human volunteers. *J Anal Toxicol, 24*(7), 467-477.

Kahlig, K. M., Binda, F., Khoshbouei, H., Blakely, R. D., McMahon, D. G., Javitch, J. A., & Galli, A. (2005). Amphetamine induces dopamine efflux through a dopamine transporter channel. *Proc. Natl. Acad. Sci. USA, 102*(9), 3495-3500.

Kahlig, K. M., & Galli, A. (2003). Regulation of dopamine transporter function and plasma membrane expression by dopamine, amphetamine, and cocaine. *Eur J Pharmacol, 479*(1-3), 153-158.

Kamali-Zare, P., & Nicholson, C. (2013). Brain extracellular space: geometry, matrix and physiological importance. *Basic Clin Neurosci, 4*(4), 282-286.

Keeler, J. F., Pretsell, D. O., & Robbins, T. W. (2014). Functional implications of dopamine D1 vs. D2 receptors: A 'prepare and select' model of the striatal direct vs. indirect pathways. *Neuroscience, 282*, 156-175. doi:10.1016/j.neuroscience.2014.07.021

Kennedy, M. B. (2013). Synaptic Signaling in Learning and Memory. *Cold Spring Harb Perspect Biol, 8*(2), a016824. doi:10.1101/cshperspect.a016824

Kerr, R. A., Bartol, T. M., Kaminsky, B., Dittrich, M., Chang, J. C., Baden, S. B., . . . Stiles, J. R. (2008). Fast Monte Carlo Simulation Methods for Biological Reaction-Diffusion Systems in Solution and on Surfaces. *SIAM J Sci Comput, 30*(6), 3126. doi:10.1137/070692017

Khelashvili, G., Stanley, N., Sahai, M. A., Medina, J., LeVine, M. V., Shi, L., . . . Weinstein, H. (2015). Spontaneous inward opening of the dopamine transporter is triggered by PIP_2-regulated dynamics of the N-terminus. *ACS Chem. Neurosci, 6*(11), 1825-1837.

Kinney, J. (2009). *Investigation of neurotransmitter diffusion in three-dimensional reconstructions of hippocampal neuropil.* (Ph. D.), University of California, San Diego, La Jolla, California.

Kinney, J. P., Spacek, J., Bartol, T. M., Bajaj, C. L., Harris, K. M., & Sejnowski, T. J. (2013). Extracellular sheets and tunnels modulate glutamate diffusion in hippocampal neuropil. *J Comp Neurol, 521*(2), 448-464. doi:10.1002/cne.23181

Kolb, S. J., Hudmon, A., Ginsberg, T. R., & Waxham, M. N. (1998). Identification of domains essential for the assembly of calcium/calmodulin-dependent protein kinase II holoenzymes. *J Biol Chem, 273*(47), 31555-31564.

Kozel, N. J., & Adams, E. H. (1986). Epidemiology of drug abuse: an overview. *Science, 234*(4779), 970-974.

Li, Y., Mayer, F. P., Hasenhuetl, P. S., Burtscher, V., Schicker, K., Sitte, H. H., . . . Sandtner, W. (2017). Occupancy of the zinc-binding site by transition metals decreases the substrate affinity of the human dopamine transporter by an allosteric mechanism. *J Biol Chem, 292*(17), 7161. doi:10.1074/jbc.A116.760140

Lisman, J. (1994). The CaM kinase II hypothesis for the storage of synaptic memory. *Trends Neurosci, 17*(10), 406-412.

Lisman, J., Yasuda, R., & Raghavachari, S. (2012). Mechanisms of CaMKII action in long-term potentiation. *Nat Rev Neurosci, 13*(3), 169-182. doi:10.1038/nrn3192

Liu, B., & Faeder, J. R. (2016). *Parameter estimation of rule-based models using statistical model checking.* Paper presented at the Bioinformatics and Biomedicine (BIBM), 2016 IEEE International Conference on.

Lodish, H., Berk, A., Zipursky, S. L., Matsudaira, P., Baltimore, D., & Darnell, J. (2000). *Neurotrasmitters, synapses and impulse transmission*.

Lotharius, J., & Brundin, P. (2002). Pathogenesis of Parkinson's disease: dopamine, vesicles and alpha-synuclein. *Nat Rev Neurosci, 3*(12), 932-942. doi:10.1038/nrn983

Lovinger, D. M. (2010). Neurotransmitter roles in synaptic modulation, plasticity and learning in the dorsal striatum. *Neuropharmacology, 58*(7), 951-961. doi:10.1016/j.neuropharm.2010.01.008

Ma, S., Cheng, M. H., Guthrie, D. A., Newman, A. H., Bahar, I., & Sorkin, A. (2017). Targeting of dopamine transporter to filopodia requires an outward-facing conformation of the transporter. *Sci Rep, 7*(1), 5399. doi:10.1038/s41598-017-05637-x

Mayer, M. L., Westbrook, G. L., & Guthrie, P. B. (1984). Voltage-dependent block by Mg2+ of NMDA responses in spinal cord neurones. *Nature, 309*(5965), 261-263.

McLellan, A. T., Lewis, D. C., O'Brien, C. P., & Kleber, H. D. (2000). Drug dependence, a chronic medical illness: implications for treatment, insurance, and outcomes evaluation. *JAMA, 284*(13), 1689-1695.

Meyer, T., Hanson, P. I., Stryer, L., & Schulman, H. (1992). Calmodulin trapping by calcium-calmodulin-dependent protein kinase. *Science, 256*(5060), 1199-1202.

Miao, Y., Nichols, S. E., Gasper, P. M., Metzger, V. T., & McCammon, J. A. (2013). *Activation and dynamic network of the M2 muscarinic receptor*. Paper presented at the Proc. Natl. Acad. Sci. U. S. A

Proceedings of the National Academy of Sciences of the United States of America. http://www.ncbi.nlm.nih.gov/pubmed/23781107

Michalski, P. J. (2013). The delicate bistability of CaMKII. *Biophys J, 105*(3), 794-806. doi:10.1016/j.bpj.2013.06.038

Michalski, P. J., & Loew, L. M. (2012). CaMKII activation and dynamics are independent of the holoenzyme structure: an infinite subunit holoenzyme approximation. *Phys Biol, 9*(3), 036010. doi:10.1088/1478-3975/9/3/036010

Miller, S. G., & Kennedy, M. B. (1986). Regulation of brain type II Ca2+/calmodulin-dependent protein kinase by autophosphorylation: a Ca2+-triggered molecular switch. *Cell, 44*(6), 861-870.

Miller, S. G., Patton, B. L., & Kennedy, M. B. (1988). Sequences of autophosphorylation sites in neuronal type II CaM kinase that control Ca2(+)-independent activity. *Neuron, 1*(7), 593-604.

Money, K. M., & Stanwood, G. D. (2013). Developmental origins of brain disorders: roles for dopamine. *Front Cell Neurosci, 7*, 260. doi:10.3389/fncel.2013.00260

Monine, M. I., Posner, R. G., Savage, P. B., Faeder, J. R., & Hlavacek, W. S. (2010). Modeling multivalent ligand-receptor interactions with steric constraints on configurations of cell-surface receptor aggregates. *Biophys J, 98*(1), 48-56. doi:10.1016/j.bpj.2009.09.043

Mortensen, O. V., & Amara, S. G. (2003). Dynamic regulation of the dopamine transporter. *Eur J Pharmacol, 479*(1-3), 159-170.

Mukherji, S., & Soderling, T. R. (1994). Regulation of Ca2+/calmodulin-dependent protein kinase II by inter- and intrasubunit-catalyzed autophosphorylations. *J Biol Chem, 269*(19), 13744-13747.

Nadkarni, S., Bartol, T. M., Sejnowski, T. J., & Levine, H. (2010). Modelling vesicular release at hippocampal synapses. *PLoS Comput Biol, 6*(11), e1000983. doi:10.1371/journal.pcbi.1000983

Nelson, A. M., Larson, G. A., & Zahniser, N. R. (2009). Low or high cocaine responding rats differ in striatal extracellular dopamine levels and dopamine transporter number. *J Pharmacol Exp Ther, 331*(3), 985-997. doi:10.1124/jpet.109.159897

Nirenberg, M. J., Vaughan, R. A., Uhl, G. R., Kuhar, M. J., & Pickel, V. M. (1996). The dopamine transporter is localized to dendritic and axonal plasma membranes of nigrostriatal dopaminergic neurons. *J Neurosci, 16*(2), 436-447.

Nolte, J. (2002). The human brain: an introduction to its functional anatomy.

Nowak, L., Bregestovski, P., Ascher, P., Herbet, A., & Prochiantz, A. (1984). Magnesium gates glutamate-activated channels in mouse central neurones. *Nature, 307*(5950), 462-465.

Nutt, D. J., Lingford-Hughes, A., Erritzoe, D., & Stokes, P. R. (2015). The dopamine theory of addiction: 40 years of highs and lows. *Nat Rev Neurosci, 16*(5), 305-312. doi:10.1038/nrn3939

Opazo, P., Labrecque, S., Tigaret, C. M., Frouin, A., Wiseman, P. W., De Koninck, P., & Choquet, D. (2010). CaMKII triggers the diffusional trapping of surface AMPARs through phosphorylation of stargazin. *Neuron, 67*(2), 239-252. doi:10.1016/j.neuron.2010.06.007

Palaniappan, S. K., Gyori, B. M., Liu, B., Hsu, D., & Thiagarajan, P. (2013). *Statistical model checking based calibration and analysis of bio-pathway models.* Paper presented at the International Conference on Computational Methods in Systems Biology.

Patton, B. L., Miller, S. G., & Kennedy, M. B. (1990). Activation of type II calcium/calmodulin-dependent protein kinase by Ca2+/calmodulin is inhibited by autophosphorylation of threonine within the calmodulin-binding domain. *J Biol Chem, 265*(19), 11204-11212.

Penmatsa, A., Wang, K. H., & Gouaux, E. (2013). *X-ray structure of dopamine transporter elucidates antidepressant mechanism*. Paper presented at the Nature. http://www.ncbi.nlm.nih.gov/pubmed/24037379

Penmatsa, A., Wang, K. H., & Gouaux, E. (2015). X-ray structures of Drosophila dopamine transporter in complex with nisoxetine and reboxetine. *Nat Struct Mol Biol, 22*(6), 506-508. doi:10.1038/nsmb.3029

Pohorille, A., Jarzynski, C., & Chipot, C. (2010). Good practices in free-energy calculations. *J Phys Chem B, 114*(32), 10235-10253. doi:10.1021/jp102971x

Pothos, E. N., Davila, V., & Sulzer, D. (1998). Presynaptic recording of quanta from midbrain dopamine neurons and modulation of the quantal size. *J Neurosci, 18*(11), 4106-4118.

Povlock, S. L., & Schenk, J. O. (1997). A multisubstrate kinetic mechanism of dopamine transport in the nucleus accumbens and its inhibition by cocaine. *J Neurochem, 69*(3), 1093-1105.

Prasad, B. M., & Amara, S. G. (2001). The dopamine transporter in mesencephalic cultures is refractory to physiological changes in membrane voltage. *J. Neurosci, 21*(19), 7561-7567.

Rao, A., Richards, T. L., Simmons, D., Zahniser, N. R., & Sorkin, A. (2012). Epitope-tagged dopamine transporter knock-in mice reveal rapid endocytic trafficking and filopodia targeting of the transporter in dopaminergic axons. *FASEB J, 26*(5), 1921-1933. doi:10.1096/fj.11-196113

Rao, A., Sorkin, A., & Zahniser, N. R. (2013). Mice expressing markedly reduced striatal dopamine transporters exhibit increased locomotor activity, dopamine uptake turnover rate, and cocaine responsiveness. *Synapse, 67*(10), 668-677. doi:10.1002/syn.21671

Razavi, A. M., Khelashvili, G., & Weinstein, H. (2017). A Markov state-based quantitative kinetic model of sodium release from the dopamine transporter. *Sci. Rep, 7*, 40076. doi:Article

Reith, M. E., Berfield, J. L., Wang, L. C., Ferrer, J. V., & Javitch, J. A. (2001). The uptake inhibitors cocaine and benztropine differentially alter the conformation of the human dopamine transporter. *J Biol Chem, 276*(31), 29012-29018. doi:10.1074/jbc.M011785200

Rellos, P., Pike, A. C., Niesen, F. H., Salah, E., Lee, W. H., von Delft, F., & Knapp, S. (2010). Structure of the CaMKIIdelta/calmodulin complex reveals the molecular mechanism of CaMKII kinase activation. *PLoS Biol, 8*(7), e1000426. doi:10.1371/journal.pbio.1000426

Rice, M. E., & Cragg, S. J. (2008). Dopamine spillover after quantal release: rethinking dopamine transmission in the nigrostriatal pathway. *Brain Res Rev, 58*(2), 303-313. doi:10.1016/j.brainresrev.2008.02.004

Rice, M. E., Patel, J. C., & Cragg, S. J. (2011). Dopamine release in the basal ganglia. *Neuroscience, 198*, 112-137. doi:10.1016/j.neuroscience.2011.08.066

Rich, R. C., & Schulman, H. (1998). Substrate-directed function of calmodulin in autophosphorylation of Ca2+/calmodulin-dependent protein kinase II. *J Biol Chem, 273*(43), 28424-28429.

Richardson, B. D., Saha, K., Krout, D., Cabrera, E., Felts, B., Henry, L. K., . . . Khoshbouei, H. (2016). Membrane potential shapes regulation of dopamine transporter trafficking at the plasma membrane. *Nat Commun, 7*, 10423. doi:10.1038/ncomms10423

Roeper, J. (2013). Dissecting the diversity of midbrain dopamine neurons. *Trends Neurosci, 36*(6), 336-342. doi:10.1016/j.tins.2013.03.003

Rooney, K. E., & Wallace, L. J. (2015). Computational modeling of extracellular dopamine kinetics suggests low probability of neurotransmitter release. *Synapse, 69*(11), 515-525. doi:10.1002/syn.21845

Rosenberg, O. S., Deindl, S., Comolli, L. R., Hoelz, A., Downing, K. H., Nairn, A. C., & Kuriyan, J. (2006). Oligomerization states of the association domain and the holoenyzme of Ca2+/CaM kinase II. *FEBS J, 273*(4), 682-694. doi:10.1111/j.1742-4658.2005.05088.x

Rosenberg, O. S., Deindl, S., Sung, R. J., Nairn, A. C., & Kuriyan, J. (2005). Structure of the autoinhibited kinase domain of CaMKII and SAXS analysis of the holoenzyme. *Cell, 123*(5), 849-860. doi:10.1016/j.cell.2005.10.029

Rothstein, J. D., Martin, L., Levey, A. I., Dykes-Hoberg, M., Jin, L., Wu, D., . . . Kuncl, R. W. (1994). Localization of neuronal and glial glutamate transporters. *Neuron, 13*(3), 713-725.

Saunders, C., Ferrer, J. V., Shi, L., Chen, J., Merrill, G., Lamb, M. E., . . . Galli, A. (2000). Amphetamine-induced loss of human dopamine transporter activity: an internalization-dependent and cocaine-sensitive mechanism. *Proc Natl Acad Sci U S A, 97*(12), 6850-6855. doi:10.1073/pnas.110035297

Seal, R. P., & Amara, S. G. (1999). Excitatory amino acid transporters: a family in flux. *Annu Rev Pharmacol Toxicol, 39*, 431-456. doi:10.1146/annurev.pharmtox.39.1.431

Sedaghat, K., Nantel, M. F., Ginsberg, S., Lalonde, V., & Tiberi, M. (2006). Molecular characterization of dopamine D2 receptor isoforms tagged with green fluorescent protein. *Mol Biotechnol, 34*(1), 1-14. doi:10.1385/MB:34:1:1

Shepherd, G. M. (2003). *The synaptic organization of the brain*: Oxford University Press.

Shields, S. M., Ingebritsen, T. S., & Kelly, P. T. (1985). Identification of protein phosphatase 1 in synaptic junctions: dephosphorylation of endogenous calmodulin-dependent kinase II and synapse-enriched phosphoproteins. *J Neurosci, 5*(12), 3414-3422.

Sik, A., Hajos, N., Gulacsi, A., Mody, I., & Freund, T. F. (1998). The absence of a major Ca2+ signaling pathway in GABAergic neurons of the hippocampus. *Proc Natl Acad Sci U S A, 95*(6), 3245-3250.

Smrcka, A. V. (2008). G protein betagamma subunits: central mediators of G protein-coupled receptor signaling. *Cell Mol Life Sci, 65*(14), 2191-2214. doi:10.1007/s00018-008-8006-5

Sneddon, M. W., Faeder, J. R., & Emonet, T. (2011). Efficient modeling, simulation and coarse-graining of biological complexity with NFsim. *Nat Methods, 8*(2), 177-183. doi:10.1038/nmeth.1546

Sorkina, T., Richards, T. L., Rao, A., Zahniser, N. R., & Sorkin, A. (2009). Negative regulation of dopamine transporter endocytosis by membrane-proximal N-terminal residues. *J Neurosci, 29*(5), 1361-1374. doi:10.1523/JNEUROSCI.3250-08.2009

Stiles, J. R., Van Helden, D., Bartol, T. M., Jr., Salpeter, E. E., & Salpeter, M. M. (1996). Miniature endplate current rise times less than 100 microseconds from improved dual recordings can be modeled with passive acetylcholine diffusion from a synaptic vesicle. *Proc Natl Acad Sci U S A, 93*(12), 5747-5752.

Stockner, T., Montgomery, T. R., Kudlacek, O., Weissensteiner, R., Ecker, G. F., Freissmuth, M., & Sitte, H. H. (2013). *Mutational analysis of the high-affinity zinc binding site validates a refined human dopamine transporter homology model*. Paper presented at the PLoS Comput. Biol

PLoS Comp Biol. http://www.ncbi.nlm.nih.gov/pubmed/23436987

Stratton, M., Lee, I. H., Bhattacharyya, M., Christensen, S. M., Chao, L. H., Schulman, H., . . . Kuriyan, J. (2014). Activation-triggered subunit exchange between CaMKII holoenzymes facilitates the spread of kinase activity. *eLife, 3*, e01610. doi:10.7554/eLife.01610

Sulzer, D., Cragg, S. J., & Rice, M. E. (2016). Striatal dopamine neurotransmission: regulation of release and uptake. *Basal Ganglia, 6*(3), 123-148. doi:10.1016/j.baga.2016.02.001

Sykova, E., & Nicholson, C. (2008). Diffusion in brain extracellular space. *Physiol Rev, 88*(4), 1277-1340. doi:10.1152/physrev.00027.2007

Taylor, I. M., Ilitchev, A. I., & Michael, A. C. (2013). Restricted diffusion of dopamine in the rat dorsal striatum. *ACS Chem Neurosci, 4*(5), 870-878. doi:10.1021/cn400078n

Thomas, B. R., Chylek, L. A., Colvin, J., Sirimulla, S., Clayton, A. H., Hlavacek, W. S., & Posner, R. G. (2016). BioNetFit: a fitting tool compatible with BioNetGen, NFsim and distributed computing environments. *Bioinformatics, 32*(5), 798-800. doi:10.1093/bioinformatics/btv655

Torres, G. E., Gainetdinov, R. R., & Caron, M. G. (2003). Plasma membrane monoamine transporters: structure, regulation and function. *Nat Rev Neurosci, 4*(1), 13-25. doi:10.1038/nrn1008

Tsai, H. C., Zhang, F., Adamantidis, A., Stuber, G. D., Bonci, A., de Lecea, L., & Deisseroth, K. (2009). Phasic firing in dopaminergic neurons is sufficient for behavioral conditioning. *Science, 324*(5930), 1080-1084. doi:10.1126/science.1168878

Tucker, K. R., Block, E. R., & Levitan, E. S. (2015). Action potentials and amphetamine release antipsychotic drug from dopamine neuron synaptic VMAT vesicles. *Proc Natl Acad Sci U S A, 112*(32), E4485-4494. doi:10.1073/pnas.1503766112

Turetken, E., Benmansour, F., Andres, B., Glowacki, P., Pfister, H., & Fua, P. (2016). Reconstructing Curvilinear Networks Using Path Classifiers and Integer Programming. *IEEE Trans Pattern Anal Mach Intell, 38*(12), 2515-2530. doi:10.1109/TPAMI.2016.2519025

van Soest, A. J., & Casius, L. J. (2003). The merits of a parallel genetic algorithm in solving hard optimization problems. *J Biomech Eng, 125*(1), 141-146.

Vaughan, R. A., & Foster, J. D. (2013). *Mechanisms of dopamine transporter regulation in normal and disease states*. Paper presented at the Trends. Pharmacol. Sci

Trends in pharmacological sciences. http://www.ncbi.nlm.nih.gov/pubmed/23968642

Venton, B. J., Michael, D. J., & Wightman, R. M. (2003). Correlation of local changes in extracellular oxygen and pH that accompany dopaminergic terminal activity in the rat caudate-putamen. *J Neurochem, 84*(2), 373-381.

Viggiano, D., Vallone, D., & Sadile, A. (2004). Dysfunctions in dopamine systems and ADHD: evidence from animals and modeling. *Neural Plast, 11*(1-2), 97-114. doi:10.1155/NP.2004.97

Vivo, M., Lin, H., & Strange, P. G. (2006). Investigation of cooperativity in the binding of ligands to the D(2) dopamine receptor. *Mol Pharmacol, 69*(1), 226-235. doi:10.1124/mol.105.012443

Volz, T. J., Hanson, G. R., & Fleckenstein, A. E. (2007). The role of the plasmalemmal dopamine and vesicular monoamine transporters in methamphetamine-induced dopaminergic deficits. *J Neurochem, 101*(4), 883-888. doi:10.1111/j.1471-4159.2006.04419.x

Wadiche, J. I., Arriza, J. L., Amara, S. G., & Kavanaugh, M. P. (1995). Kinetics of a human glutamate transporter. *Neuron, 14*(5), 1019-1027.

Wang, K. H., Penmatsa, A., & Gouaux, E. (2015). Neurotransmitter and psychostimulant recognition by the dopamine transporter. *Nature, 521*(7552), 322-327. doi:Article

Wheeler, D. S., Underhill, S. M., Stolz, D. B., Murdoch, G. H., Thiels, E., Romero, G., & Amara, S. G. (2015). Amphetamine activates Rho GTPase signaling to mediate dopamine transporter internalization and acute behavioral effects of amphetamine. *Proc Natl Acad Sci U S A, 112*(51), E7138-7147. doi:10.1073/pnas.1511670112

Wise, R. A., & Rompre, P. P. (1989). Brain dopamine and reward. *Annu Rev Psychol, 40*, 191-225. doi:10.1146/annurev.ps.40.020189.001203

Wu, S., Bellve, K. D., Fogarty, K. E., & Melikian, H. E. (2015). Ack1 is a dopamine transporter endocytic brake that rescues a trafficking-dysregulated ADHD coding variant. *Proc Natl Acad Sci U S A, 112*(50), 15480-15485. doi:10.1073/pnas.1512957112

Xia, Z., & Storm, D. R. (2005). The role of calmodulin as a signal integrator for synaptic plasticity. *Nat Rev Neurosci, 6*(4), 267-276. doi:10.1038/nrn1647

Zhu, J., & Reith, M. E. (2008). Role of the dopamine transporter in the action of psychostimulants, nicotine, and other drugs of abuse. *CNS Neurol Disord Drug Targets, 7*(5), 393-409.